Dynamic monitoring of water status of plants in the fields under environmental stress : Design of a portable NMR and applied to sorghum

Sidi-Boulenouar Rahima

THÈSE POUR OBTENIR LE GRADE DE DOCTEUR DE L'UNIVERSITE DE MONTPELLIER

En Physique

École doctorale : Information, Structures, Systèmes

Unité de recherche UMR 5221

Suivi dynamique aux champs du statut hydrique des plantes sous contrainte environnementale: Conception d'une RMN transportable et application au sorgho

Présentée par SIDI-BOULENOUAR Rahima

Le 11/10/2018

Sous la direction de Christophe Coillot CNRS, L2C et Jean-Luc Verdeil AGAP, CIRAD

Devant le jury composé de

Bertin Nadia, DR, INRA Avignon - PSH	Présidente
Ginefri Jean Christophe, MC, Univ. Paris Sud - IR4M	Rapporteur
Herbette Stephane, MC, Univ. Clermont Auvergne INRA Clermont, PIAF-SUREAU	Rapporteur
Goze-Bac Christophe, DR, Univ. Montpellier CNRS - L2C	Examinateur
Musse Maja, CR, IRSTEA Rennes - OPAALE	Examinatrice
Granier Christine, DR, INRA Montpellier - LEPSE	Examinatrice
Coillot Christophe, IR, Univ. Montpellier CNRS- L2C	Directeur de thèse
Verdeil Jean Luc, DR, CIRAD Montpellier - PHIV	Co-Directeur de thèse
Asfour Aktham, MC, Univ. Grenoble Alpes - G2Elab	Invité
van As Henk, PR, Univ. Wageningen - Laboratory of Biophysics & Research	Invité

UNIVERSITÉ DE MONTPELLIER

Suivi dynamique aux champs du statut hydrique des plantes sous contrainte environnementale: Conception d'une RMN transportable et application au sorgho

SIDI-BOULENOUAR Rahima

March 12, 2019

Contents

Remerciements

Le présent travail rapporté dans ce manuscrit est le fruit d'une collaboration entre deux domaines : la physique et l'agronomie. Ces travaux de thèse ont été menés entre deux sites : l'équipe BioNanoNMRI du laboratoire Charles Coulomb (L2C), unité du CNRS et de l'université de Montpellier et l' équipe PHIV au sein du CIRAD. Une thèse est un aboutissement de travail qui ne peut être achevé sans un entourage précieux que je tiens à remercier ici.

Tout d'abord, je remercie chaleureusement mes directeurs de thèse Christophe Coillot et Jean Luc Verdeil. Ils ont su m'apporter un soutien constant, une disponibilité, un optimisme, une confiance et des conseils avisés au cours de ces trois années de thèse. Au delà de vos compétences dans vos domaines respectifs, vos qualités humaines ont beaucoup contribuer à ma prise de conscience verte et responsable et puis à une passion envers le monde de la plante. J'ai énormément appris à vos cotés, je vous en remercie.

J'adresse aussi mes remerciements à Eric Nativel, co directeur de cette thèse et porteur du projet au LabEx NUMEV, qui a toujours répondu présent pour faire progresser cette thèse.

Je souhaite remercier Jean Christophe Ginefri et Stephane Herbette d'avoir accepté de rapporter cette thèse. Je tiens à remercier Nadia Bertin d'avoir accepter d'être présidente du jury. Je remercie également l'ensemble des membres de jury : Christine Granier, Maya Musse, Christophe Goze-Bac, Aktham Asfour et Henk van As. La version finale de ce manuscrit a bénéficié de leur relecture très attentive et de leurs remarques précieuses et pertinentes.

Je remercie tout particulièrement Christophe Goze-Bac pour sa bonne humeur quotidienne, sa disponibilité, sa rigueur, sa capacité d'analyse des problèmes et ses très nombreuses connaissances scientifiques qui m'ont permis de progresser et de m'épanouir tant sur le plan professionnel que personnel. Tu m'as montré que le monde de la recherche pouvait être un univers passionnant. Cette thèse et moi te devons beaucoup et oui grâce à toi "y'a un avant et un après RSB".

Je tiens à remercier mes khouyas Maïda Cardoso et Guillaume Saint Martin, votre soutien quotidien indéfectible et votre enthousiasme contagieux m'ont permis de ne jamais dévier de mes objectifs malgré quelques obstacles. La khouya, depuis mon arrivée en France, tu as

toujours était là pour moi même si quand tu viens en moto, des fois, tu me dis que je ne suis pas ta préférée (impolitesse majeure) et Maïda, tu sais que t'es "le coeur" de cette team, une coéquipière de choc et une amie formidable sur laquelle je peux toujours compter. "Je vous souhaite de tout mon coeur tout le bonheur du monde et un bon boulon".

Je remercie toute l'équipe BioNanoNMRI pour la bonne ambiance de travail et les nombreux bons moments passés ensemble et je pense à : Eric Alibert et ses précieux conseils, la très gentille Pauline De Pellegars, la plus anglophone de l'équipe Amandine Laboulais, ma mamoun canard Corinne Lautier qui a toujours veiller sur sa petite, Sébastien Rousset qui m'a fait découvrir les fromages de France et qui s'est souvent arraché les cheveux pour essayer de me comprendre, la très rigolotte Jeanne Simon avec qui j'aime bien passé du temps, Thanks ma Marioné Tardieu et enfin les plus sages de l'équipe Dominique Petit et Michel Zanca qui ont toujours répondu présents pour des échanges scientifiques.

Je tiens également à remercier le CIRAD pour l'accueil et les conditions de travail privilégiées qui m'ont été offertes, et je pense tout particulièrement à : Frédérique Gatineau, Christelle Batiste, Sandrine Roques et Denis Fabre.

Je remercie tout les ingénieurs, assistants ingénieurs, techniciens et mécaniciens du L2C que j'ai côtoyé : Raymand Aznar, Dominique Caron, Alain Charbit, Jérome Barbat, Alban Bertrand et Pascal Gamet.

Je remercie l'ensemble des stagiaires avec qui j'ai eu la chance de travailler : Olivier Yzebe, Ariston Do Reis, Pan Liu, Julie Plateau, Tirot Louis, Pauline Deltour et Alexie Techer.

Je remercie aussi mes "Girls" Chahrazed et Latifa qui m'ont permis d'oublier momentanément le travail dans des soirées, repas, sorties.....Vous avez su me soutenir, me supporter, m'encourager pendant toute la durée de ma thèse et plus particulièrement durant les derniers mois de rédaction qui n'ont pas toujours été faciles.

Mes remerciements vont à ma famille, je remercie mon frère et mes soeurs, Anouar, Amina et Marwa, ma nièce Racha ainsi que mes parents, pour leur soutien au cours de ces trois années et sans lesquels je n'en serais pas là aujourd'hui.

Enfin, ces remerciements ne peuvent s'achever, sans une pensée pour mon cher père, à qui j'aurais tant aimé faire lire cette thèse. Ses encouragements depuis toute petite pour que je m'en sorte et que je m'épanouisse en tant que femme indépendante sont les piliers fondateurs de ce que je suis et de ce que je fais. Merci papa, ce travail t'es dédié.

List of Publications

Patent

Eric Nativel, Pauline de Pellegars, **Rahima Sidi-Boulenouar**, Michel Zanca, Christophe Goze-Bac, Eric Alibert and Christophe Coillot, Bobines homogènes en champ magnétique pour la RMN et l'IRM, under progress, SATT, (2018).

Papers

(1) **Rahima Sidi-Boulenouar**, Ariston Reis, Eric Nativel, Simon Buy, Pauline de Pellegars, Pan Liu, Michel Zanca, Christophe Goze-Bac, Jérôme Barbat, Eric Alibert, Jean-Luc Verdeil, Frédéric Gatineau, Nadia Bertin, Atma Anand and Christophe Coillot, Homogenous static magnetic field coils dedicated to portable Nuclear Magnetic Resonance for agronomic studies, JSSS journal, 7, 227-234, https://doi.org/10.5194/jsss-7-227-2018, (2018).

(2) Simon Le Floch, Simon Buy, Ning Tang, **Rahima Sidi-Boulenouar**, Michel Zanca, Patrick Canadas, Eric Nativel, Maïda Cardoso, Eric Alibert, Guillaume Dupont, Dominique Ambard, Jean-Luc Verdeil, Christophe Maurel, Nadia Bertin, Christophe Goze-Bac and Christophe Coillot, Flip-Flop method : a new T1-weigthed flow-MRI for plants studies, PLOS one, 3 (3), DOI: 10.1371/journal.pone.0194845, https://prodinra.inra.fr/record/427381, (2018).

(3) Christophe Coillot, **Rahima Sidi-Boulenouar**, Eric Nativel, Michel Zanca, Eric Alibert, Maïda Cardoso, Guillaume Saintmartin, Harun Noristani, Nicolas Lonjon, Marine Lecorre, Florence Perrin, and Christophe Goze-Bac, Signal modeling of an MRI ribbon solenoid coil dedicated to spinal cord injury investigations, 5, 137-145, https://doi.org/10.5194/jsss-5-137-2016 JSSS journal, (2016).

(4) Lamiaa M.A. Ali, Emna Mathlouthi, Marilyn Kajdan, Morgane Daurat, Jérôme Long, **Rahima Sidi-Boulenouar**, Maïda Cardoso, Christophe Goze-Bac, Nourredine Amdouni, Yannick Guar, Joulia Larionova and Magali Gary-Bobo, Multifunctional manganese-doped Prussian blue nanoparticles for two-photon Photothermal Therapy and Magnetic Resonance Imaging, Photodiagnosis and Photodynamic Therapy, 22:65-69,
DOI: 10.1016/j.pdpdt.2018.02.015, (2018).

(5) Harun N. Noristani, Hassan Boukhaddaoui, Guillaume Saint-Martin, Pauline Auzer, **Rahima Sidi-Boulenouar**, Nicolas Lonjon, Eric Alibert, Nicolas Tricaud, Christophe Goze-

Bac, Christophe Coillot and Florence E. Perrin, A Combination of Ex vivo Diffusion MRI and Multiphoton to Study Microglia/Monocytes Alterations after Spinal Cord Injury, Frontiers in Aging Neurosciences, 9: 230, DOI: 10.3389/fnagi.2017.00230, (2017).

National and International Conferences

(1) **Rahima Sidi-Boulenouar**, Maïda Cardoso, Christophe Coillot, Sébastien Rousset, Eric Nativel, Fréderic Gatineau, Jean-Luc Verdeil and Christophe Goze-Bac, Multi scale NMR investigations of two anatomically contrasted genotypes of sorghum under normal conditions and during water stress, oral presentation and issue paper, NMRFood, Rennes, (2018).

(2) **Rahima Sidi-Boulenouar**, Olivier Yzebe, Christophe Coillot, Eric Alibert, Eric Nativel, Rémi Jelinek, Fréderic Gatineau, Jean-Luc Verdeil, Gilles Vercambre, Nadia Bertin and Christophe Goze-Bac, Real-Time dynamical monitoring plants status in normal and stress conditions : from Low Fields NMR in laboratory to compact NMR *in planta*, oral presentation, Eurolax, Pologne, (2017).

(3) **Rahima Sidi-Boulenouar**, Olivier Yzebe, Eric Nativel, Christophe Coillot, Jean-Luc Verdeil, Fréderic Gatineau, Eric Alibert, Nadia Bertin and Christophe Goze-Bac, Dynamical monitoring of water status in plant : from low field NMR in laboratory to compact NMR *in planta*, oral presentation, Djeddah (Arabie Saoudite), Workshop CNRS-KACST, (2016).

(4) **Rahima Sidi-Boulenouar**, Olivier Yzebe, Eric Nativel, Christophe Coillot, Jean-Luc Verdeil, Fréderic Gatineau, Eric Alibert, Nadia Bertin and Christophe Goze-Bac, Dynamical monitoring of water status in plant : from low field NMR in laboratory to compact NMR *in planta*, oral presentation, Riadh (Arabie Saoudite), Meeting KAUST, (2016).

(5) **Rahima Sidi-Boulenouar**, Olivier Yzebe, Christophe Coillot, Eric Alibert, Eric Nativel, Rémi Jelinek, Fréderic Gatineau, Jean-Luc Verdeil, Gilles Vercambre, Nadia Bertin and Christophe Goze-Bac, Real-Time dynamical monitoring plants status in normal and stress conditions : from Low Fields NMR in laboratory to compact NMR *in planta*, poster, Barcelona, ESMRMB, (2017).

(6) **Rahima Sidi-Boulenouar**, Olivier Yzebe, Christophe Coillot, Eric Alibert, Eric Nativel, Rémi Jelinek, Fréderic Gatineau, Jean-Luc Verdeil, Gilles Vercambre, Nadia Bertin and Christophe Goze-Bac, Real-Time dynamical monitoring plants status in normal and stress conditions : from Low Fields NMR in laboratory to compact NMR *in planta*, poster, IDB 2017 BioTechnologie, Hammamet (Tunisie), (2017).

(7) **Rahima Sidi-Boulenouar**, Olivier Yzebe, Eric Nativel, Christophe Coillot, Jean-Luc Verdeil, Fréderic Gatineau, Eric Alibert, Nadia Bertin and Christophe Goze-Bac, Dynamical monitoring of water status in plant : low field NMR investigations, poster, GERM, Lisbonne,

(2016).

(8) **Rahima Sidi-Boulenouar**, Olivier Yzebe, Eric Nativel, Christophe Coillot, Jean-Luc Verdeil, Fréderic Gatineau, Eric Alibert, Nadia Bertin and Christophe Goze-Bac, Dynamical monitoring of water status in plant : Magnetic sensors for low field NMR investigation, poster, Relaxome, Paris, (2016).

(9) **Rahima Sidi-Boulenouar**, Olivier Yzebe, Eric Nativel, Christophe Coillot, Jean-Luc Verdeil, Fréderic Gatineau, Eric Alibert, Nadia Bertin and Christophe Goze-Bac, Dynamical monitoring of water status in plant : Magnetic sensors for low field NMR investigation, poster, GDR ondes, Montpellier, (2016).

(10) **Rahima Sidi-Boulenouar**, Olivier Yzebe, Eric Nativel, Christophe Coillot, Jean-Luc Verdeil, Fréderic Gatineau, Eric Alibert, Nadia Bertin and Christophe Goze-Bac, Dynamical monitoring of water status in plant : from low field NMR in laboratory to compact NMR in planta, poster, Hortimodel INRA, Avignon, (2016).

List of Symbols & Abbreviations

- $\overrightarrow{A}$: Vector potential
- A_s : CO2 assimilation rate
- A_{fov} : Voxel surface
- A_p : RF pulse amplitude
- ATP : Adenosine Tri Phosphate (chemical energy)
- b : Gap between coils
- $\overrightarrow{B}_0$: Static magnetic field in Tesla
- $\overrightarrow{B}_1$: Dynamic magnetic field
- $\overrightarrow{B}_{rf}$: Radiofrequency magnetic field
- B_{SHS} : Total magnetic field
- δBw_{-3db} : Bandwidth at -3db :
- BFF : Biomass For the Future project
- C : Capacity in Farad
- C_t : Tuning capacity
- C_m : Matching capacity
- c : light velocity
- ci : Intercellular CO2 mole fraction
- C3 : mode of CO2 fixation by plant
- C4 : mode of CO2 fixation by plant
- CAM : Crassulacean Acid Metabolism (mode of CO2 fixation by plant)

- CO2 : Carbon Dioxide
- CPMG : Carr Purcell Meiboom Gill
- C6H12O6 : Glucose molecule
- D : Diameter
- DC : Direct Current mode
- D2O : Deuterium
- e : Induced voltage
- E : Leaf transpiration
- e_t : Thickness of material
- ETo : Evaporative demand
- EM : ElectroMagnetic
- f, f_0: frequency
- f_{min} : function of minimization
- Fasga : Staining
- FID : Free Induction Decay
- FOV : Field Of View
- FT : Fourier Transform
- FTSW : Fraction of Transpirable Soil Water
- g_s : stomatal conductance
- g_{max} : function of maximization
- G_n : intensity of gradient
- $GH2O$: Stomatal conductance
- h : Plank's constant
- h_s : Exchange coefficient
- H_c : Heigh of coil

- H2O : Water Molecule
- HSPs : High temperature shock proteins
- I : Current
- i : Nuclear spin
- IZ : Inner zone
- J : Current density
- k : Boltzmann constant
- k_c : Coil sensitivity coefficient
- L : Inductance
- LVDT : Linear Variable Differential Transformer
- $\overrightarrow{L}_s$: Kinetic Moment
- l_c : coil length
- l_w : Wire length
- L_B : Line broadening
- l_s : Left shift
- $\overrightarrow{M}$: Macroscopic magnetization
- $\overrightarrow{M}_0$: Macroscopic magnetization at Boltzmann equilibrium
- M_x, M_y : Transverse magnetization components
- M_z : Longitudinal magnetization component
- MEMS : Multi Echo Multi Slice
- MDS : Maximum Daily Trunk Shrinkage
- MNTDS : Minimum Daily Trunk Diameter
- MRI : Magnetic Resonance Imaging
- MXTDS : Maximum Daily Trunk Diameter
- M_{xy} : Transverse component of the magnetization

- n : direction of gradient
- N : number of coils
- N_S : number of slices
- N_{turns} : number of turns
- N_{points} : FID size
- N_α, N_β : Numbers of nuclei in the respective spin levels
- NADPH : Nicotinamide Adenine Dinucleotide Phosphate
- NMR : Nuclear Magnetic Resonance
- O2 : Oxygen
- OZ : Outer zone
- PEPc : Phosphoenolpyruvate carboxylase
- P : Pressure
- PAR : Luminosity
- P_n : Total power
- P_w : Pulse Width
- P_n^m : Legendre polynomials with positive integer order n and positive integer degree m
- PSD : Power Spectral Density
- Q_{Factor} : Quality factor
- R : Radius
- R_{cond} : Resistance of conduction
- R_{ac} : Resistance in AC mode
- R_{dc} : Resistance in DC mode
- R_s : Relaxation Matrix
- R_D : Recovery delay
- r_c : Radius of coil

- Res_1 : Resistance of coil
- RF : Radio Frequency
- RMN : Résonance Magnétique Nucléaire
- ROI : Region Of Interest
- Rx : Receiver
- s : Quantum number
- S : Section
- S_w : Spectral width
- S_{flip}, S_{flop} : Signal in slice
- SEMS : Spin Echo Multi Slice
- SHS : Space Harmonic Suppression
- SNR : Signal to Noise Ratio
- T : Temperature in Kelvin
- T_∞ : Room temperature
- T_s : Surface temperature
- T_z : Transmittance
- t_p : Pulse duration
- TEM : Transmission Electron Microscopy
- TE : Echo time
- THz : Terahertz
- TGR : Trunk Growth Rate
- T_R : Repetition time
- T_{hk} : Thickness of slice
- Tx : Transmitter
- T_1, T_2, T_2^* : relaxation times

- UV : Ultraviolet radiation
- V : Volume
- v : Velocity
- W_m : magnetic energy
- W_F, W_D, W_I : Weight
- WUE : Water Use Efficiency
- Z, Z_t, Z_m : Impedances
- α, β : Spin levels
- α_s, β_s : Optimization parameters α_{Ernst} : Ernst angle
- ΔE : Energy
- δe : Elementary induced voltage
- δm : Elementary magnetic field moment
- θ : Unknown angular positions
- γ : Gyromagnetic ratio
- ν_0 : Larmor frequency
- μ_0 : Vacuum magnetic permeability
- μ : Magnetic permeability
- ϵ_0 : vacuum permittivity
- τ : Time period
- ω_0 : Precession rate (Larmor precession)
- ω_{rf} : RF pulsation
- λ : Wave length
- λ_S : Thermal conductivity
- σ : Noise voltage
- φ : Phase

- φ_t : Density of the flux
- Φ_t : Flow through a surface
- ϕ : Total flux
- PHI_{rad} : Power radiated by a surface
- PHI_{conv} : Power emmited by a surface
- θ : Angle
- ρ : Resistivity
- $\overrightarrow{\Gamma}$: Couple of forces
- Ψ_{s} Osmotic potential
- Ψ_{p} Turgor pressure
- Ψ_{w} Water potential

List of Tables

List of Figures

Résumé

Aujourd'hui, comprendre comment les plantes réagissent au stress hydrique est essentiel pour relever le défi de développer de nouveaux cultivars et de nouvelles stratégies d'irrigation, compatibles avec le maintien de la productivité des cultures sous les effets néfastes du réchauffement climatique. Dans ce contexte, l'étude des relations eau/plante présente un intérêt majeur pour la modélisation des réponses des plantes et des organes aux contraintes biotiques et abiotiques. Paradoxalement, il existe très peu de méthodes directes et non invasives pour quantifier et mesurer la quantité et le débit d'eau dans les plantes.

Dans le cadre de cette thése, nous rapportons le développement d'une méthodologie innovante basée sur la relaxation par résonance magnétique nucléaire (RMN) à champ faible. Un dispositif RMN dédié à la caractérisation des plantes vivantes a été construit dans une chambre climatique qui permet un contrôle et une modification minutieuse des paramètres environnementaux pendant l'expérimentation sur des longues périodes au laboratoire. En parallèle, une imagerie RMN complémentaire à haut champ magnétique pour étudier, l'anatomie, la teneur en eau, le transport du phloéme et du xylème chez les plants de sorgho a été réalisé. La combinaison de ces approches nous permet de déterminer des biomarqueurs éco-physiologiques innovants et de concevoir de nouvelles expériences en laboratoire et même dans les champs.

Un résultat particulièrement intéressant concerne l'étude de la distribution spatiale de l'eau dans les tiges (nœuds et entrenœuds) à partir de la relaxométrie RMN à faible champ et des images IRM 3D à haute résolution. La modification des paramètres de relaxation RMN au cours du cycle diurne dynamique sera présentée dans des conditions normales et en situation de stress abiotique. Une application directe permet d'extraire des biomarqueurs écophysiologiques qui permettent d'explorer et de modéliser les flux d'eau en période de stress hydrique et d'analyser leur impact sur le développement du sorgho.

Notre but ultime est d'effectuer ces études RMN directement dans les champs. Ainsi, un dispositif RMN portable bas champ magnétique (8mT) conçu et développé pour cet objectif est présenté. Le développement et l'optimisation de l'homogénéité d'un aimant résistif et de sondes inductives Radio Fréquences (RF) ainsi que des séquences d'impulsions RMN, afin de respecter la polyvalence et les conditions thermiques pour maintenir la plante intacte sont

décrits en détail. Enfin nous présenterons les investigations menées avec ce dispositif en laboratoire, dans les serres et dans les champs de sorgho à Mauguio (près de Montpellier).

Abstract

Today, understanding how plants respond to water stress is essential to meet the challenge of developing new cultivars and new irrigation strategies, consistent with the maintenance of crop productivity with the evidence of global warming. In this context, the study of plant /water relations is of central interest for modeling plant and organ responses to biotic and abiotic constraints. Paradoxically, there are very few direct and non-invasive methods to quantify and measure the content and the flow of water in plants.

For this thesis, we report on the development of an innovative methodology based on low-field Nuclear Magnetic Resonance Relaxometry (NMR). A dedicated NMR device to perform NMR measurements on living plants has been built in a climatic chamber that allows a control and careful modification of environmental parameters during experimentation over reliable periods of time at the laboratory. In parallel, complementary NMR imaging at high magnetic field to study, the anatomy, water content, phloem and xylem transport in sorghum plants were performed. The combination of these approaches allows us to discuss and introduce an innovant eco-physiological biomarkers and to design new experiments in the laboratory and even in the fields.

One particular interesting result concerns the investigation of the spatial distribution of water stems (node and inter node) from low field NMR Relaxometry and 3D high resolution MRI images. The modification of the NMR relaxation parameters during dynamic diurnal cycle will be presented in normal and abiotic stress conditions. A direct application permits to extract eco-physiological biomarkers which allows to explore and model water fluxes during water stress and to analyze their impact on the development of sorghum plant.

Our ultimate goal is to perform these NMR studies directly in the fields. Thus, a low field portable NMR device ($8mT$) designed and developed for this project is presented. The development and optimization of the homogeneity of a resistive magnet, inductive Radio Frequency coils in order to respect the versatility and thermal conditions to maintain the plant intact are described in details. Finally we will present our investigations conducted with this device in the laboratory, in the greenhouses and in sorghum fields at Mauguio (close to Montpellier).

Description générale

Dans le contexte du changement climatique, les recherches sur le fonctionnement et la santé des plantes au sein de l'agrosystème deviennent primordiales pour relever des défis multiples : développer des stratégies de culture et d'irrigation pour satisfaire les besoins alimentaires des populations et préserver les ressources et les écosystèmes tout en limitant les émissions de gaz à effet de serre. Une clé de ces études est l'accès au "statut hydrique" et à la "dynamique des flux" de sèves brute et élaborée dans des plantes vivantes.

En effet, l'eau est le composant chimique le plus important dans les plantes. Un état adéquat de l'eau dans la plante exige un équilibre entre la quantité absorbé par les racines du sol et la demande atmosphérique (c.-à-d. les exigences de transpiration). Lorsque l'absorption d'eau est insuffisante, un déficit en eau appelé aussi "stress hydrique" peut se développer et causer un impact direct sur la croissance et le rendement. Cela peut également causer des dommages irréversibles et éventuellement entraîner la mort des plantes, Il est donc essentiel d'étudier le quantité, la mobilité et le statut en général de cet eau dans les plantes.

En présence de stress hydrique, la plante va réagir en régulant l'ouverture stomatique ce qui aura pour effet de réduire les flux xylémiens (lesquels transportent la sève brute des racines jusqu'aux feuilles grâce au mécanisme d' évapo-transpiration) mais aussi, grâce à des interactions cellulaires, réduire les flux phloémiens (lesquels transportent la sève élaborée : sucres carbonés issus de la photosynthèse des feuilles vers les organes puits et, en particulier, les fruits ou les graines). Ainsi, les modifications des flux de sève apparaissent aussi comme des manifestations physiologiques précoces de premier plan pour apprécier la santé de la plante et comprendre les stratégies mises en place en présence d'un stress hydrique.

L'étude du statut et le dynamisme de l'eau dans les plantes est devenue donc une priorité dans le domaine d'agronomie mais à ce jour les principales mesures utilisées découlent de méthodes destructives et difficilement exploitables en dehors des laboratoires de recherche.

Dans ce contexte, cette thèse vise le développement d'un outil original de diagnostic portable et non invasif basé sur le principe de la Résonance Magnétique Nucléaire (RMN) fonctionnant à très bas champ magnétique afin d'effectuer des mesures *in naturae*. En effet, ce type d'appareillage RMN offre plusieurs avantages expérimentaux en terme de contraste

par relaxation nucléaire entre différents tissues tout en restant simple et par conséquent à coût de fabrication avantageux par rapport aux équipements commerciaux actuels.

Cependant la technique de RMN à bas champ souffre d'une perte de sensibilité importante qui nous a conduit à étudier et proposer des possibilités d'amélioration innovantes de l'homogénéité de l'aimant qui produit le champ magnétique statique ainsi que la partie détection radio-fréquence (bobine et amplificateur à faible bruit) afin d'augmenter le rapport signal sur bruit des expériences.

L'originalité de nos travaux est également liée à la nature des plants étudiés. En effet, cette thèse vise à étudier le statut hydrique et la dynamique des flux dans le sorgho, une espèce candidate à fort potentiel économique en raison de son immense biodiversité, sa croissance rapide, sa grande quantité de biomasse générée, son incroyable panel génotypique et phénotypique. De plus, sa résistance à la sécheresse et aux températures élevées permet de s'adapter aux contraintes climatiques réelles. Notre objectif est de mettre au point une méthodologie pour révéler des "marqueurs écophysiologiques " de stress hydrique directement dans les serres et dans les champs.

Ainsi, nos expériences sont menées sur deux génotypes très contrastés le Biomasse 140 et SSM 1267.

Le présent manuscrit est organisé en 5 chapitres. D'abord, nous introduirons des notions de base sur l'organisme du sorgho à l'échelle tissulaire et cellulaire, les principales fonctions nécessaires à sa vie et à sa croissance et son comportement face aux contraintes environnementales.

Les mesures de certains paramètres physiologiques indiquant les variations de l'état de l'eau et sa dynamique sont délicates car ces paramètres sont très variables pendant le jour / la nuit et pendant le développement et la croissance de la plante. Autre facteur de complication, l'effet ou l'impact du stress qui peut en outre faire varier ces paramètres en fonction du stade de développement de la plante. Ainsi, le deuxième chapitre est une revue sur les techniques les plus fréquemment utilisées et leur contribution dans l'étude de l'état de l'eau et des flux dans les plantes.

Dans le troisième chapitre, nous présentons les concepts de base nécessaires pour appréhender les phénomènes physiques de la relaxométrie et de l'imagerie RMN. Ensuite, nous présentons l'ensemble des éléments qui composent un système RMN, les technologies utilisées pour chaque élément et leurs limites qui nous aideront à développer un appareil à bas champ.

Le quatrième chapitre est consacré à la description des développements instrumentaux qui ont permis de repousser les limites expérimentales en améliorant fortement le rapport signal sur bruit à bas champ d'abord tout en tenant compte de la contrainte de la miniaturisation

et de la polyvalence de la conception pour conserver la plante intacte.

Le dernier chapitre présente nos investigations multimodales incluant : histologie, relaxométrie bas champ en laboratoire et dans les serres ainsi que Imagerie RMN haute résolution à haut champ.

Enfin, une conclusion générale terminera ce manuscrit en exposant les perspectives envisagées et les améliorations qui peuvent être apportées.

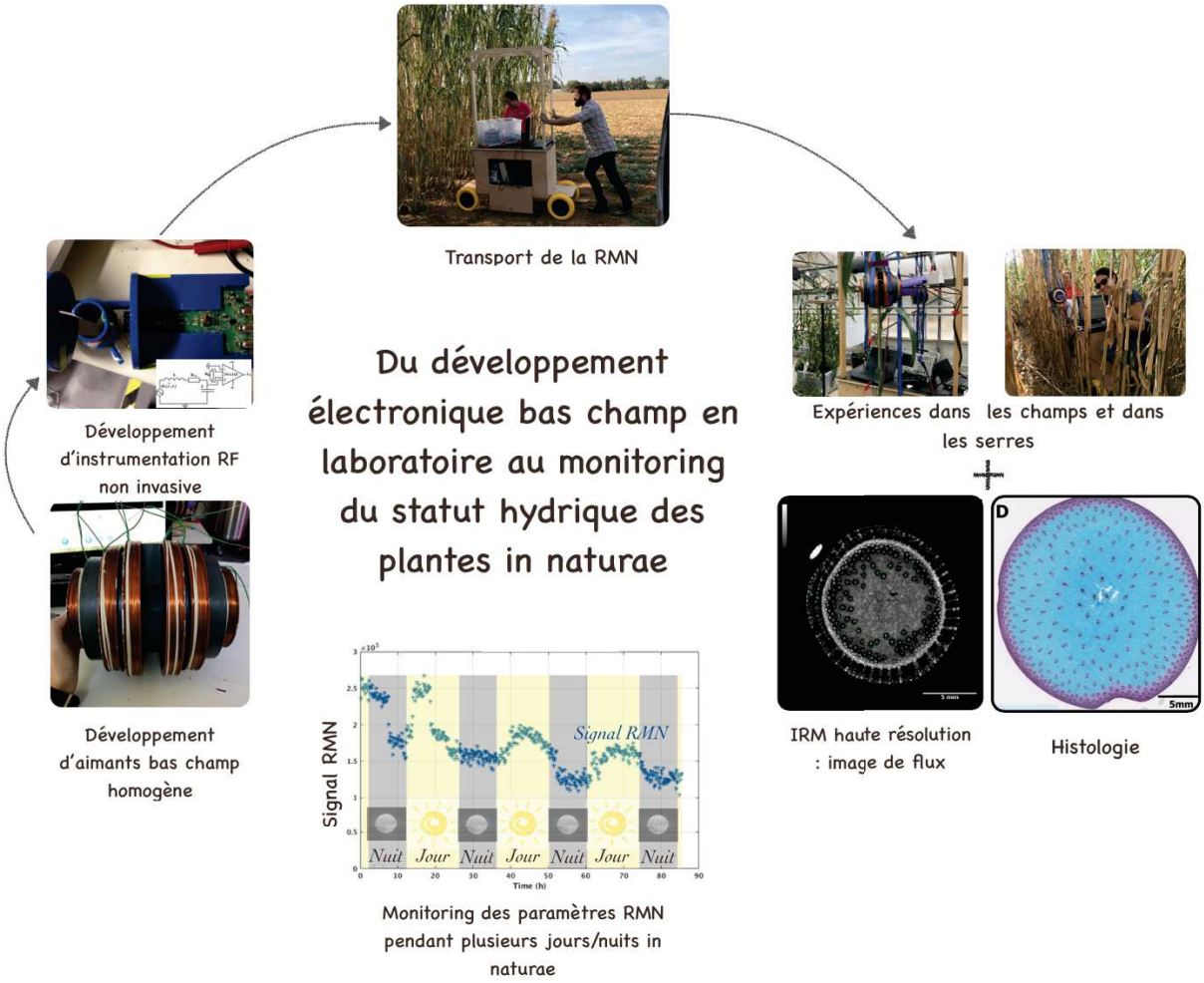

Chapter 1. Introduction to the sorghum plant

In this part, we will introduce basic notions about the organization of sorghum at tissular and cellular scale, the major functions needed for its life and growth and its behavior under environmental constraints. This step is necessary and fundamental in order to provide an interpretation of the results of NMR Relaxometry and imaging obtained in laboratory, greenhouse and fields. The documentation and illustrations for this introduction are based in part on the book "Le sorgho" by [Chantereau, 2013] and "Physiologie vegétale" by [Coupe, 2016].

1 Sorghum : plant of Biodiversity

Today, one of the main issues facing humanity is the fight against global warming. Studies have shown that it is related to the massive emissions of greenhouse gases into the atmosphere. These emissions are generated by the consumption of fossil fuels, such as oil or coal and by our economic models largely based on fossil energies. It is therefore urgent to accelerate the energy transition towards renewable energies and to develop a "green society" that respects the environment [GIEC, 2014].

Indeed, the current climate change and the degradation of the generated environments (natural and agricultural), make particularly acute the question of understanding plants and their behavior in an impacted environment (by drought, high temperature, salinity), this is one of CIRAD's research axes.

It is, in this context, the "Biomass for the future" project was born (2013-2019). This project brings together 22 public and private partners, including actors from the innovative sectors of bio-based materials. It aims to develop new varieties and growing systems of Miscanthus (for North of France) and Sorghum (for South of France), improved for the biomass (organic matter), with a low environmental impact and a composition adapted to industrial applications (biomaterials such a biocomposites) and energy production (bio-methanisation).

In this thesis, we are interested by sorghum plant, a candidate specie with high economic potential because of its immense biodiversity, its rapid growth, its large quantity of biomass generated, the incredible genotypic and phenotypic panel available to it. Moreover, its resis-

tance to drought and high temperature giving the possibility to adapt to the present climatic constraints. These climate changes induce stress at the plant level. Our goal is to discover markers to monitor these stress in the fields and develop an ideotypes adapted to the intended applications (ie methanisation, incorporation of fibers into bio-sourced resin...etc).

2 About sorghum plant

For centuries, sorghum played an important role in the nutrition of many people in Africa and Asia, but its use has extended and today this plant is involved in different fields such as industry food (flour, alcohols and sugar), animal feed, biofuels, cosmetics industry and also automotive industry.

The common sorghum (Sorghum bicolor), is a species of monocotyledonous plants of the family of Poaceae, originating from Africa [Chantereau, 2013]. With world production estimated in 2010 at 56 million tons, sorghum is the world's fifth cereal (just after the corn, the rice, the wheat, and the barley).

As with all species of the family Poaceae, sorghum consists of a root system and aerial organs whose architecture is formed by a stem with iterative structure composed by analogous units called phytomers, consisting of a node and internode, a particular leaf divided into two parts (the sheath and the blade) and an axillary bud. The stems end in an internode called peduncle, carrying a fruit bunch in the case of sorghum, is a panicle (see Fig. 1)[Chantereau, 2013].

To ensure its growth and development, the plant selects and extracts the elements it needs in the surrounding environment: carbon from carbon dioxide of atmospheric air, oxygen in the air and soil and finally water and the other nutrients took primarily from the soil. These processes are achieved by three fondamental physiological phenomena :

2.1 Photosynthesis

The photosynthesis (from Greek phos "light" and synthesis "combination") is the bioenergetic process that allows organisms called photoautotrophic (such as plants) to synthesize organic matter using CO2, water and light energy.

The general equation for photosynthesis is as follows :

6 CO2 + 6 H2O ——> C6H12O6 + 6 O2

Photosynthesis takes place in leaves whose anatomy is specialized in performing this function. The cells of the leaves contain many chloroplasts that contain a green pigment, the chlorophyll, capable of capturing this light energy. This energy is used to synthesize sugar molecules from water drawn from the soil and carbon dioxide from the atmosphere that enters

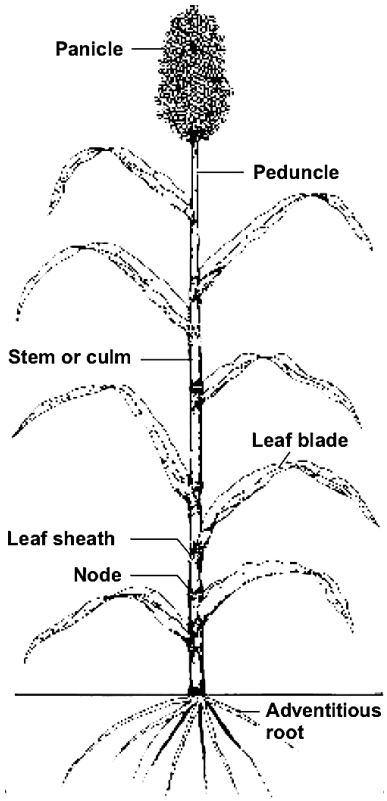

Figure 1 – Illustration of the morphology of sorghum plant [Chantereau, 2013]

the leaves through the stomata.

The first phase of photosynthesis, called clear phase is directly dependent on light. This photochemical phase corresponds to the capture of light energy by the photosynthesis pigments that absorb light and convert it into chemical energy in the form of ATP and reducing power in the form of NADPH (see Fig. 2).

During the second phase of photosynthesis (improperly called dark phase or Benson-Calvin Cycle), the CO2 of the atmosphere is fixed by a particular sugar (the ribulose diphosphate). This carboxylation is controlled by a key enzyme : the Rubisco (Ribulose 1,5 bisphosphate carboxylase / oxygenase). This enzyme is the key for the fixation of CO2 carbon dioxide in plant biomass by initiating the Calvin cycle. Rubisco is probably the most abundant protein on Earth where it accounts for about 50% of soluble proteins in plant leaves (see Fig. 2).

The Rubisco allows incorporation of carbon from atmospheric CO2 which has also an affinity for atmospheric oxygen O2. Under certain conditions such as at high temperature or low atmospheric CO2, the likelihood of fixation of the O2 by the Rubisco becomes more important. This phenomenon related to the oxygenase activity of Rubisco which consumes, in general, oxygen (O2) and which releases carbon dioxide (CO2) occurs in the light, in the chloroplasts instead of the photosynthesis that should normally take place.

In the case of photosynthesis, CO2 reacts with a 5-carbon molecule to form two 3-carbon molecules. These two molecules will be called later: 5C and 3C respectively. One molecule of CO2 plus one molecule with 5 carbons gives rise to a product with a total of 6 carbons: in the form of two molecules with 3 carbons (1 + 5 = 3 + 3). Part of the 3C molecules will be used for sugar synthesis (the glucose molecule), while the rest will be used to reform 5C molecules to restart the Calvin cycle.

However, in the case of photorespiration, the incorporated O2 (under control of the oxidase activity of the Rubisco) reacts with the 5C molecule to form the 3C molecule and a 2-carbon molecule. Most often, this latter can be partially recovered as a 3C molecule, with release of CO2. However, in some algae, the 2C molecule is lost. In this case, the photorespiration leads to the production of a 3C molecule, contrary to the photosynthesis that produces 2x3C.

Photorespiration is therefore an expensive and disadvantageous process. It leads to the reduction of photosynthesis efficiency in different ways:

- It occurs in the place of photosynthesis and leads to the incorporation of one less carbon molecule
- Unlike photosynthesis, it does not allow the recycling of the initial 5C molecule and therefore consumes carbon resources
- Moreover, photorespiration is a process that consumes more energy, compared to photosynthesis, and therefore leads to a waste of energy.

One of the reasons that would explain this phenomenon goes back to the origins of the activity of the Rubisco enzyme, dating from a geological period where the atmospheric oxygen concentration was negligible or non-existent. Some plants living in arid environments, however, have evolved to avoid this very expensive phenomenon and to improve CO2 fixation under water deficit and high temperatures.

There are 3 modes of CO2 fixation in plants during photosynthesis : C3, C4 and CAM (Crassulacean Acid Metabolism). Their mechanisms differ in the effectiveness of this carboxylation step [Yamori, 2014].

- **C3 Plants :** About 85% of the species on the planet belong to this family (rice, wheat, soybeans and all trees). Here, the fixation of CO2 is achieved during the day and the "Calvin cycle" is done at mesophyll cells, see Fig. 3. The C3 mechanism works well in cool environments and have no special features to combat photorespiration.
- **C4 Plants :** In this family, the light reactions and the "Calvin cycle" are physically separated, see Fig. 3. The fixation of CO2 during the day occur in the mesophyll cells

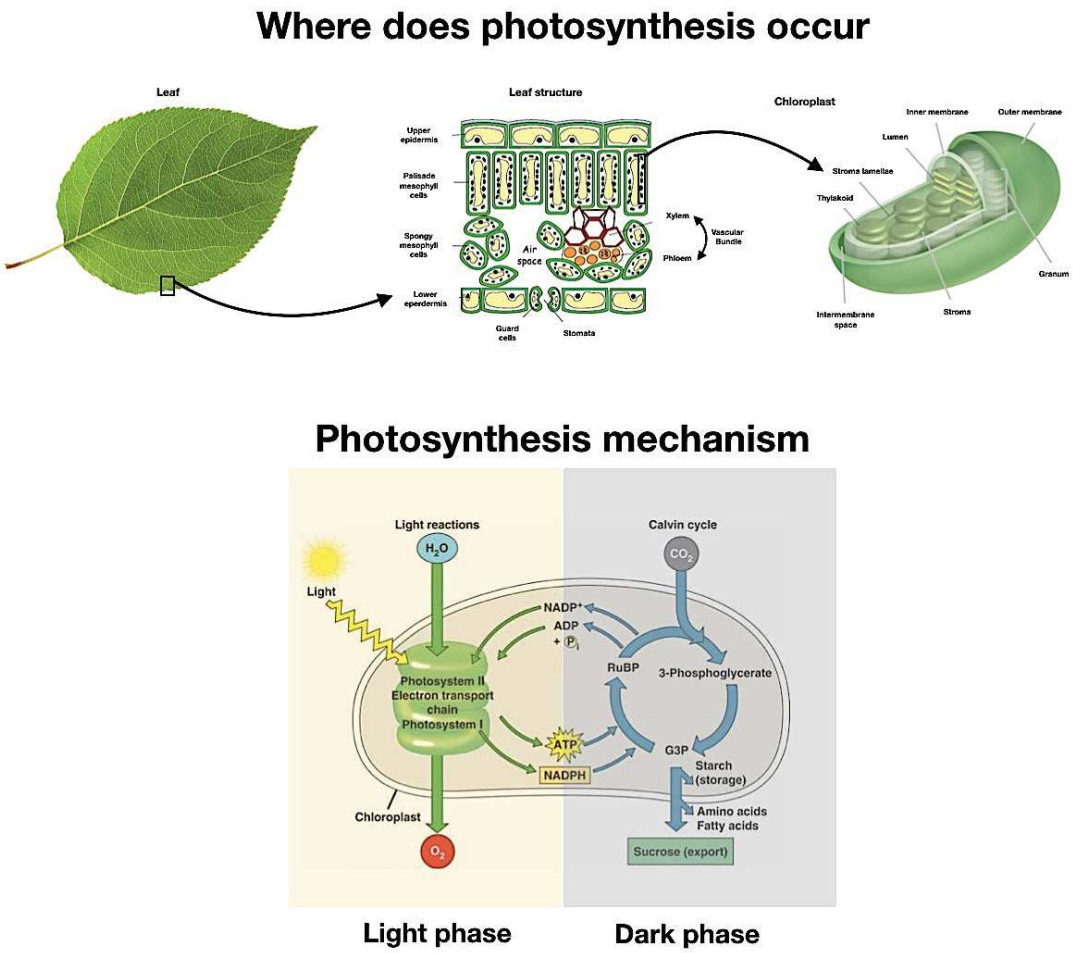

Figure 2 – Illustration of where the process of photosynthesis is localized at the level of the plant and the main mechanisms engendered during the day/night. Modified from : https://www.quora.com/How-can-the-reaction-equation-of-photosynthesis-be-described

to form a simple oxaloacetate (carbon organic acid), this step is carried out by a non-Rubisco enzyme, PEP carboxylase (PEPc). The "Calvin cycle" occur in others cells called "bundle sheath cells". During this cycle, the oxaloacetate is then converted into a similar molecule, malate, which will transport up to "bundle sheath cells" where it releases a CO2.

The enzyme PEPc that has no tendency to bind the O2, this feature allows it to reduce the photorespiration and adapt to the hot climatic. Thus, C4 plants particularly is located in tropical areas with high light environment like sorghum, maize... etc[Coupe, 2016].

- **CAM Plants :** Instead of separating the light reactions and the use of CO2 the "Calvin cycle" in space, CAM plants separate these processes in time, Fig. 3 . In fact,

the fixation of CO2 by the PEPc is done during the night. During this cycle the malate is converted to another organic acid and stored inside mesophyll cell. In the daylight, the CAM plants do not open their stomata, but they can transport and release a CO2 from organic acid. Theses features allows to not only avoid the photorespiration, but makes this category also very water-efficient. CAM plants are typically dominant in very hot and dry areas like cactus, pineapple...

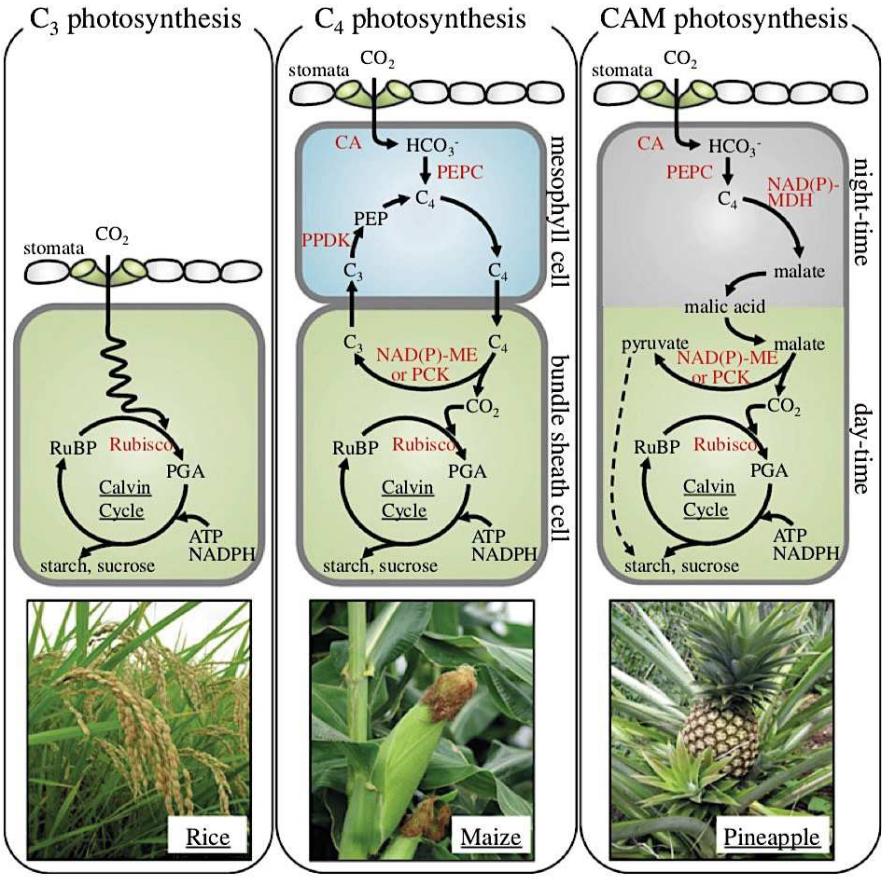

Figure 3 – Illustration of the photosynthetic types : C3, C4 and CAM [Yamori, 2014]

2.2 Water status

The water is absorbed first at the level of the absorbent root hairs. Subsequently, it must reach the conducting vessels that carry the water to the leaves in two different pathways. The apoplast pathway corresponds to the way using the cell wall. The symplast pathway corresponds to the way using plasmodium cells to switch from one cytoplasm to another, see Fig. 4.

Apoplasm refers to the extracellular continuum formed by pectocellulosic walls and empty spaces between plant cells. Water and solutes can navigate by non-selective passive diffusion.

Symplasm refers to the intracellular continuum formed by plant cells through plasmodesmata. The cytoplasm of cells thus connected then form a single compartment shared by all the cells. The size of plasmodesmes regulates the size of solutes that can actively navigate from one cell to another. The passage of the water from the apoplasm to the symplasm requires the transport of the water through the cytoplasmic membrane which borders the cells. Thus involves aquaporins which are membrane proteins that form "pores" permeable to water molecules in biological membranes.

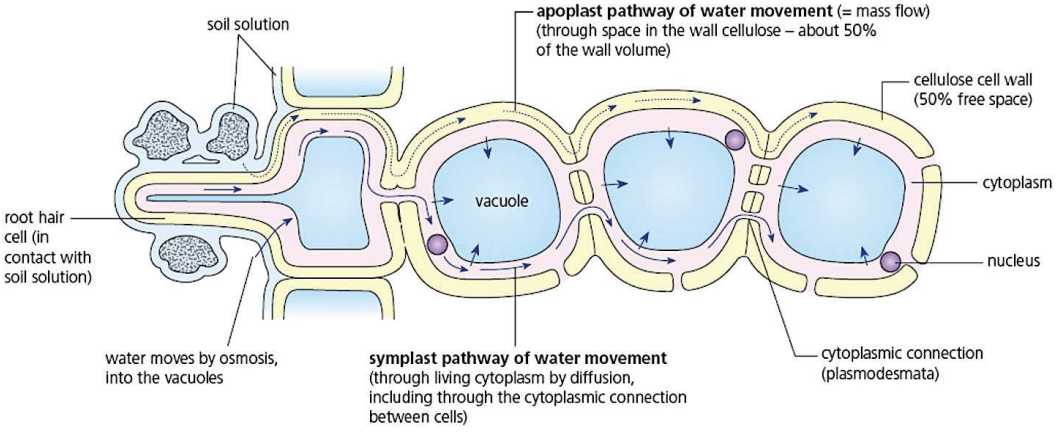

Figure 4 – Illustration of the principal pathways of water at cellular level - modified from http://alevelnotesastar.blogspot.com/2016/10/7-transport-in-plants.html

In the roots, the symplasm ensures the passage of water and solutes from the soil to the central cylinder where the sap-conducting bundles sit. The symplastic path is made obligatory by the presence of the Casparian band in the endoderm that obstruct the apoplastic pathway. This is due to the fact that endodermis cell walls contains suberin, a strong hydrophobic macromolecule.

Thus, in the roots, the symplastic path is made obligatory to allow the passage of water and solutes from the soil to the central cylinder where the sap-conducting bundles sit by the presence of Caspary frames in the endoderm that obstruct the apoplastic way.

Water enters the plant through root end by osmotic forces and matrix forces.

Osmotic forces is a process by which the molecules of solvent (water) move from a region of low concentration to a region of high concentration through pathways. Matrix forces include imbibition forces and capillary forces. The imbibition forces originate electrostatic attractions between the charges that constitute the soil. Capillary forces are related to surface tension phenomena.

The concept of water potential Ψ_w is commonly used to evaluate a plant's ability to take water from the soil and mobilize it to the leaves. For the plant, the hydric potential depends essentially on the balance of two opposing forces: the osmotic potential Ψ_s and the turgor

pressure Ψ_p exerted by the cell walls. The water flows will result from the balance between these osmotic and mechanical forces [Chantereau, 2013].

This water movement is governed principally by two hydric motors :

- **The transpiration :** is the emission of water in the vapor state generally by the leaf. In this case, the water is guided by a negative hydrostatic pressure = tension : water drawn towards the high by a voltage, generated by leaf transpiration.

  This phenomenon is the main driving force in sap circulation and occurs mainly in the stomata. The regulation of their opening and the environmental conditions influences the intensity of transpiration [Chantereau, 2013].

- **The root pressure :** in times of very low transpiration there is another type of force to ensure the rise of the water of the aerial parts : positive hydrostatic pressure force = root pressure. This is another phenomenon of pression that allows the absorption of water by the roots (xylem cells) due to the accumulation of local mineral ions (potassium, chlorine) that is transported with water.

  We observe the establishment of this type of force at the beginning and end of the day and in a non-transpiring period, for young plants, when the transpiration is very low.

Water is found in plants under two states:

- Free water: it can be in solution (in vacuoles or saps) and in the form of vapour (stomatal chamber).
- Confined water: it can be linked by the osmotic force and by the capillary force.

2.3 Mineral nutrition

In addition to water, the roots of plants draw from the soil minerals essential for their growth and development. The mineral elements obviously do not play the same role in vegetable nutrition. Some (oxygen, carbon, hydrogen, nitrogen, phosphorus, sulfur) are the basic constituents of plant tissues and are assembled during organic synthesis. Others, the cations (potassium, calcium, magnesium) are mainly used to maintain a balance with the anions in the internal environment. And finally, the oligo elements (iron, copper....) act as catalysts for metabolic reactions.

3 Transport system of the sap

The water and mineral salts that constitute the raw sap extracted from the soil by the roots as well as the elaborated sap made of water and the sugars synthesized in the leaf are transported

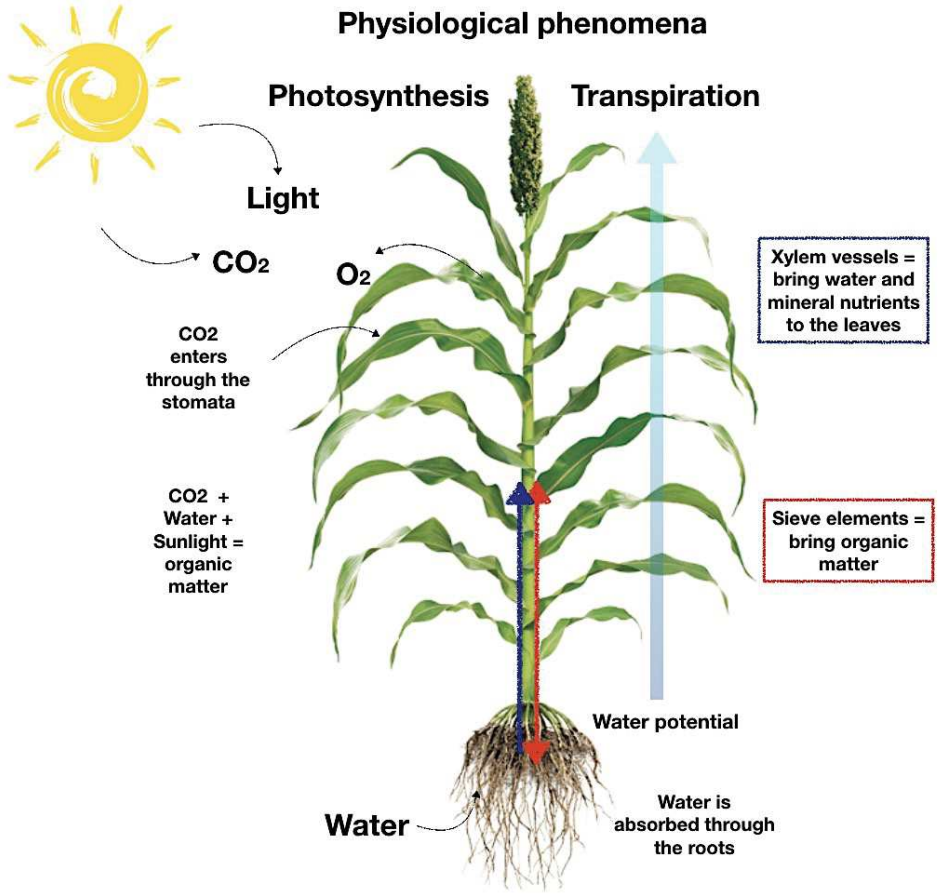

Figure 5 – Illustration of the principal interaction of plant with surrounding environment

by the vascular system of the plants. Plant vascular system contains two types of tissues : xylem and phloem (see Fig. 6).

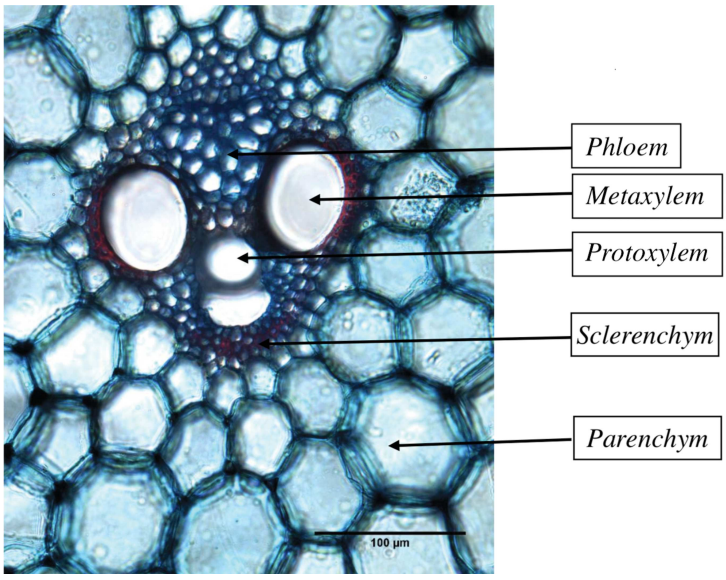

Figure 6 – Organization of a vascular tissue at stem level of sorghum plant - transversal slice - Fasga coloration- from BFF project

3.1 Xylem : structure and function

The xylem, vessels and tracheids of the roots, stems and leaves are interconnected to form a continuous system of water ducts reaching all parts of the plants (see Fig. 5). It transports water and soluble mineral nutrients from the roots throughout the plant. It is also used to replace water lost during transpiration, photosynthesis and growth. Xylem sap consists mainly of water and inorganic ions, although it can contain a number of organic chemicals as well. The transport is passive, not powered by energy spent by the xylem vessels or tracheary elements themselves, which are dead cells with lignified water-proof cell walls and no longer have living contents. Transporting sap upwards becomes more difficult as the height of a plant increases and upwards transport of water by xylem is considered to limit the maximum height of trees.

The most widely accepted theory for the transport of the raw sap through xylem vessels is the cohesion-tension theory [Dixon, 1894] (see Fig. 7). It is based on intermolecular attraction to explains the process of water flow upwards (against the force of gravity) through the xylem of plants. Indeed, water is a polar molecule and when two water molecules approach one another, the slightly negatively charged oxygen atom of one forms a hydrogen bond with a slightly positively charged hydrogen atom in the other. This attractive force, along with other intermolecular forces, is one of the principal factors responsible for the occurrence of surface tension in liquid water. It also allows plants to draw water from the root through the xylem to the leaf. Water is constantly lost through transpiration from the leaf. When one water molecule is lost another is pulled along by the processes of cohesion and tension. Transpiration pull, utilizing capillary action and the inherent surface tension of water, is the primary mechanism of water movement in plants [Vilagrosa, 2012], [Coupe, 2016]. However, it is not the only mechanism involved. Any use of water in leaves forces water to move into them. Transpiration in leaves creates tension (differential pressure) in the cell walls of mesophyll cells. Because of this tension, water is being pulled up from the roots into the leaves, helped by cohesion (the pull between individual water molecules, due to hydrogen bonds) and adhesion (the stickiness between water molecules and the hydrophilic cell walls of plants). This mechanism of water flow works because of water potential (water flows from high to low potential), and the rules of simple diffusion.

Root pressure is also playing a role in water transport by xylem vessels. If the water potential of the root cells is more negative than that of the soil, usually due to high concentrations of solute, water can move by osmosis into the root from the soil. This causes a positive pressure that forces sap up the xylem towards the leaves. Root pressure is highest in the morning before the stomata open and allow transpiration to begin.

There is a strong correlation between transpiration and conduction velocity of sap. The speed of the raw sap is temperature dependent and in a general way it depends on anything that influence the transpiration. The speed of the raw sap is variable: it increases until the middle of the day then decreases in the afternoon when the stomata close at the hottest hours of the day. This speed varies from $0.14 mms^{-1}$ in some pines to $12.8 mms^{-1}$ in some creepers. It varies from 16 to 45 m / h in trees such as ash or elm [Coupe, 2016].

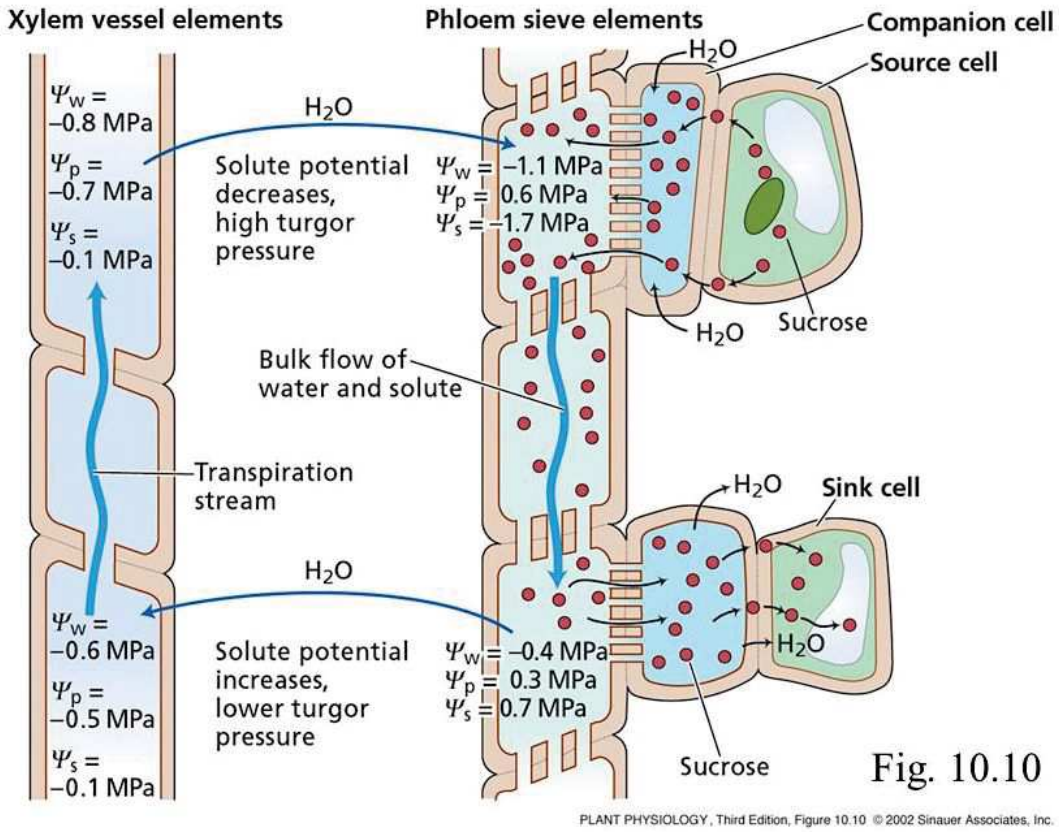

Figure 7 – Pressure flow hypothesis of Munch - Transport system of the sap [Dixon, 1894]

3.2 Phloem : structure and function

Phloem is the vascular tissue responsible for the transport of sugars from source tissues (photosynthetic leaf cells) to sink tissues (roots, developing flowers or fruits). Other molecules such as proteins are also transported throughout the plant via phloem [Nabors, 2008]. The phloem sap is a downward-flowing sap that supplies sugar to all sink organs of the plant (see Fig. 5).

The phloem is a complex structure comprising three main cell types, namely parenchymal cells, companion cells and sieve elements. The parenchymal cells can store sugars from photosynthesis as starch before transport, when the sieve elements are saturated. The companion cells have metabolic functions: such as protein synthesis, energy supply, and transfer of pho-

tosynthetic assimilates to the sieve elements. The sieve elements are rows of cells allowing the circulation of the sap containing the sugars synthetized in the leaves during photosynthesis through perforations of their transverse partitions. The Munch Pressure Flow Hypothesis, also known as the Mass Flow Hypothesis is the best-supported theory to explain the movement of sap through the phloem. Indeed, at the source end of the phloem (area where sugar is synthesized), sugars are moved into the phloem sieve elements. This increase in solute decreases the water potential of sieve elements and causes water to flow in from of xylem vessels (downward circulation) by osmosis (see Fig. 7).

The sugar loading of the phloem sieve elements decreases the water potential of the latter. In Xylem vessels (rising circulation) the sap is much less concentrated than in the phloem sieve elements (downward circulation). The water thus passes through osmosis from a xylem vessels to a phloem sieve element causing an increase in the hydrostatic pressure of the sieve elements. The hydrostatic pressure is constantly increasing, the sap developed is pushed to low pressure environments, causing the sap developed downward. On the way, the sucrose is regularly reabsorbed by the target organs bordering the vessels, decreasing the concentration of the sap. The water then goes back into the xylem vessels to resume the previous cycle.

The sap elements must remain at least partially alive and keep a functioning plasma membrane in order to help control the flow of sugars into and out of the sap element [Kehr, 2007]. Recent studies have demonstrated the relationship between structure and size of sieve element and its hydraulic resistance. In fact, the hydraulic resistance in the phloem is inversely proportional to the height of the tree because of a change in the structure of the sieve elements along the trees, so in trees, a new robust transport pathway model is suggested involving several trees [Savage, 2018].

4 Types of stress and their effects on the plant life

Stress is any external condition that affects the growth, development or productivity of a plant. It is known that there are two types of stress. The first is the biotic stresses (caused by other organisms) and the second is abiotic stresses (occurring whenever there is an excess or deficit in the physical or chemical environment of the plant). Stress is recognized by a plant when it is perceived at the cellular level and then transmitted to the whole plant. The resulting change alters growth and development, and influences the reproductive abilities of the plant [Ben Rejeb, 2014], [Suzuki, 2014].

4.1 Biotic stress

They are a lot and originate from viruses, phytophagous organisms and pathogens. In order to cope, the plant sets up a defense system that involves a chain of reactions. The defensive plant proteins produced act as a bulwark against harmful agents.

4.2 Abiotic stress

Plants depend simultaneously on their internal status and their environmental conditions that can cause abiotic stress include : floods, drought, excessive salinity of soils or water, the presence of an inadequate mineral in the soil, heavy metals, the excess of light that stimulates photo inhibition, the case of low illumination, UV radiation, phytotoxic compounds such as ozone which is a high oxidizing reactor, air pollution, oxidized products formed from pesticide reactions [Zhu, 2016], [Vesna, 2017], [Cramer, 2011].

Hydric and salinity are the most frequent and most studied stress. They can impose on plants metabolic, physiological and phenological changes.

4.3 Impact and response of plant after an abiotic stress

In this section, we will focus on the effects of abiotic stress only that can cause multiple responses at multiple levels of the plant :

- **Molecular level :** at this level there is an alteration of the expression of genes, case of oxidation damage of bio molecules or the case of the typical response at high temperatures which is manifested by a reduction in the synthesis of normal proteins accompanied by an acceleration of the transcription of new proteins called high temperature shock proteins (HSPs) [Kregel, 2002], [Cramer, 2011].

- **Cellular level :** at this level, stress can cause a change in the metabolism, a trouble on ion transport, an increase in membrane permeability and fall modification in membrane potential.

- **Whole plant level :** the stress response is manifested at the level of the whole plant by a decrease in the rate of photosynthesis, foliar damage, a reduction in growth and a decrease in productivity.

5 Study of hydric stress in sorghum plant

Several origins of hydric stress can be distinguished:

- Hydric stress caused by insufficiency of water at the root level or drought

- Hydric stress due to high water loss at the leaf level, caused by heat, wind or low relative humidity
- Hydric stress due to cold
- Hydric stress due to excess of water caused by strong rain (floods)

In water stress caused by drought, plants develop resistance mechanisms that can be grouped into two main categories according to [Chaves, 2003]:

- Avoidance is to maintain the water potential and to limit as much as possible the loss of water by transpiration. Some plants close very quickly their stomata, others limit the leaf mass, or increase the entrances of water with deeper roots like trees.

- Tolerance is to implement mechanisms to support the stress and maintain the physiological functions of growth and development by decreasing the water potential, maintain turgidity by adjusting the osmotic potential obtained by accumulation of mineral ions and organic compounds.

Global warming has induced changes in the life of the plant. The increase in temperature and drought are the two most striking effects of this change. Today it is essential to develop methods to respond to this problem to ensure the agricole productivity for the next generations. Despite the efforts put in place to prevent stress, nowadays, there is still a few techniques often invasive to measure stress in the plant. Thus, it is urgent to find a way to detect stress and act accordingly to reduce its impact on productivity and why not set up a smart irrigation strategy to save water use in the land especially for developing countries.

Chapter 2. Multi Scale Technologies used to monitor Water Status and Sap Flow in plants

Water is the most important chemical component of plants. An adequate state of the plant's water requires that soil root absorption requires atmospheric demand (ie, transpiration requirements). When water absorption is insufficient, a water deficit can develop and can directly impact the growth and the yield. This can cause also an irreversible damage and can eventually lead to death of the plants. It is therefore essential to find ways to investigate without invasivity the "water status".

In plant, the measurements of some physiological parameters that indicate the water status variations are delicate because these parameters are very variable during the day/night and during the development and growth. The xylem and phloem fluxes being very sensitive to any modification of the water potential or osmotic potential gradients, it makes their evaluation even more difficult [Tixier, 2013]. As another complicating factor, the effect or impact of stress may further change these parameters depending on the stage of development of the plant.

However, several measurement methods exist and can characterize the water status in plant or further the sap flow informations (velocity, volume flow). The purpose of this chapter is to review the most frequent techniques used for the study of the water status and fluxes of plants.

6 Review of the classical water status method

6.1 Pressure chamber

For more than a century, the pressure chamber was a reference in the measurement of water potential (Ψ_w) and pression volume at different levels of plants : leaves, stem and roots [Scholander, 1965]. The pressure chamber technique permits also to measure the hydraulic resistance of plant related to xylem sap and membrane damage [Boyer, 1967], [Oosterhuis, 1983] and [Turner, 1988].

Overview of techniques used to monitor the water status and Flow Sap				
Techniques	Investigated parameters	Output parameters	Scale	Refs
Pressure chamber	Pressure in MPa	Water potentiel, pression volume relation, hydraulic resistance and membrane damage	leaf, stem or root	[Boyer, 1967], [Oosterhuis, 1983], [Turner, 1988], [Taiz, 2014].
Dendometer	Variation of diameter in μm	Growth and Water state	stem, trunk or fruit	[Daudet, 2005], [Ortuno, 2010], [Van Der Maaten, 2016].
Fluorometer	Photosynthesis activity/Stomatal conductance g_s in $mmol.m^{-2}.s^{-1}$	Gaz diffusion and water content	Leaf	[Begue, 1992], [Fay, 1995], [Nagy, 1995], [Jones, 1998], [Bunce, 2001].
Isopiestic Psychometer	Pressure in MPa	Water potential	leaf, stem or trunk	[Barrs, 1965], [Oosterhuis, 1983], [Martinez, 2011], [Taiz, 2014].
Thermal Infrared Imaging	Indices related to the temperature	Water content	leaf	[Monteith and Szeicz, 1962], [Tanner, 1963], [Kotchi, 2004].
Terahertz	Transmitted and Reflected signal	Water content	leaf	[Hu, 1995], [Hadjiloucas, 1999], [Breitenstein, 2011], [Gente, 2016].
Dielectric sensors	Dielectric proprieties	Water content	leaf	[Emmerik, 2017].
Tomography ultra fast neutron	Neuton attenuation	Root uptake, Sap Flow, Embolism	root, stem	[Matsushima, 2009], [Moradi, 2011], [Zarebanadkouki, 2011], [Tötzke, 2013].
NMR/MRI	T_1, T_2 and flow	Water content and Sap Flow	stem, fruit	[Köckenberger, 1997], [Windt, 2006], [Musse, 2009a], [Musse, 2009b].

Table 1 – Techniques used and the main investigated parameters to monitor the water status and the flow sap in plant

There are different types of pressure chambers, some using a tank of high pressure gas, some using a hand-pump, but all work on the same basic principle. The Fig. 8 is an example of use of pressure chamber for water potential measurement at the stem level illustrated by [Taiz, 2014].

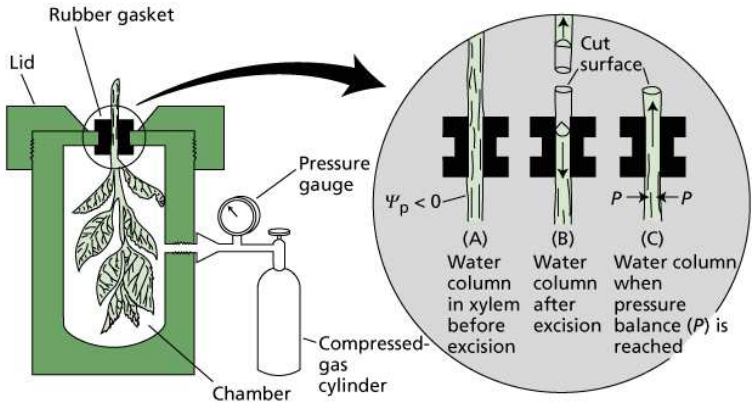

Figure 8 – The pressure chamber method for measuring plant water potential. The diagram at left shows a shoot sealed into a chamber, which may be pressurized with compressed gas. The diagrams at right show the state of the water columns within the xylem at three points in time: (A) The xylem is uncut and under a negative pressure, or tension. (B) The shoot is cut, causing the water to pull back into the tissue, away from the cut surface, in response to the tension in the xylem. (C) The chamber is pressurized, bringing the xylem sap back to the cut surface [Taiz, 2014]

The results shown in Fig. 9 is an example of a study that suggests that Ψ_w measurement at the stem level can be a useful indicator of vine plant water status and a practical technique for growers to manage breeding strategies irrigation [Cole, 2015].

However, the technique is destructive, time consuming and proved useful only when the majority of cells in a sample were damaged (lack of precision). Despite its invasiveness, the pressure chamber is still frequentty used particularly in fields studies (portability) thanks to its simplicity of use and the speed of measurement.

6.2 Dendometer

The dendometers allow to measure the micro-fluctuations of the diameter of the stem which can inform on the growth of the plant and its water state. It is known that, the variations in stem diameter reflect a combination of four phenomena: irreversible radial growth, reversible dehydration / rehydration of living cells, thermal expansion and contraction, and expansion of xylem tissues due to change of internal tensions and influenced by plant development [Daudet, 2005], [Van Der Maaten, 2016].

Generally, dendometer consists of a Linear Variable Differential Transformer (LVDT) linear displacement sensor and a metal support made of Invar (iron-nickel alloy with a very low

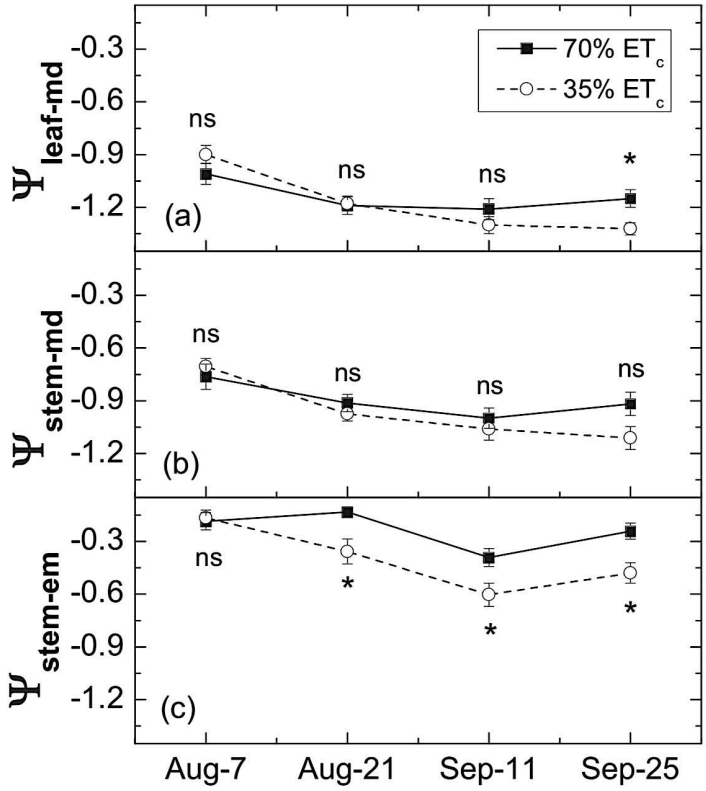

Figure 9 – Seasonal patterns of grapevine water potentials (Ψ_w) at two levels of sustained deficit irrigation, 70% of crop evapotranspiration (ETc) and 35% ETc. Leaf or stem Ψ_w was measured using a leaf pressure chamber at three different times of the day : (a) midday $\Psi_{leaf-md}$, (b) midday $\Psi_{stem-md}$ and (c) early morning $\Psi_{stem-em}$. ns and * indicate no significant difference and significant difference at $P < 0.05$, respectively. All Ψ_w values reported in units of MPa [Cole, 2015]

coefficient of expansion) allowing the sensor to be fixed to the element to be measured (stem, branch or fruit), see Fig. 10.

These studies highlights also the daily variations (Diurnal fluctuations) of stem diameter with a minimum diameter of the stem occurring just before the end of the light period after daily watering and a maximum at the end of the dark period when the optimal tissue water content was restored. These changes in stem diameter reflect a new water balance. This dynamic behavior suggests the involvement of two types of water sources : the first, in direct relation with the transpiration flow, the second, more slowly involved by higher resistances and physiological mechanisms. These variations are also sensitive to climatic fluctuations [Daudet, 2005].

Papers reporting data acquired by this method highlight the usefulness of LVDT for detecting moderate stress, but stress intensity can not be quantified. The LVDT requires maintenance when applied in the field, especially in case of rapid growth and needs protection against any potential physical contact (passage in the row, raindrops, birds insects) source of

Figure 10 – Photograph of LVDT sensor device for measuring diameter fluctuations in trunks of citrus tree [Ortuno, 2010]

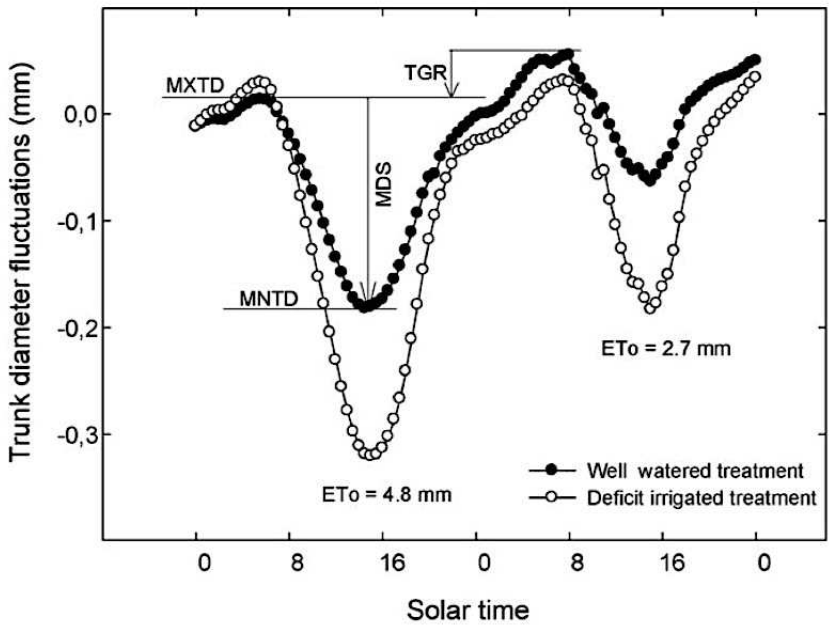

Figure 11 – Daily trunk diameter fluctuations indices during two days at different evaporative demand (ETo) in well watered and deficit irrigated plum trees : maximum (MXTD) and minimum (MNTD) daily trunk diameter, maximum daily trunk shrinkage (MDS) and trunk growth rate (TGR) [Daudet, 2005]

artefacts [Ortuno, 2010].

6.3 Fluorometer

Stomatal conductance is the dominant factor in the diffusion conductance of leaf surfaces, which controls both the water loss from plant leaves and the assimilation of CO2 for photosynthesis. Measurements of diffusion conductance are therefore important indicators of plant water status and provide a valuable insight into plant growth and plant adaptation to environmental variables (temperature, light ...).

Stomatal conductance, expressed in $mmol.m^{-2}.s^{-1}$, is the measurement of the flow of outgoing water vapor or incoming CO2 carbon dioxide from a leaf through its stomata. Stomatal size and its opening is the main determinant of gas diffusion conductance g_s at the leaf surface.

Different measurement systems exist but the most commonly used devices is gas-exchange fluorescence system (discovered since 1985 by Heinz Walz) that measures the rate of humidification inside a small chamber clipped onto a sheet.

Different study demonstrated the interaction of environmental factors on the net reduction in g_s as diurnal and seasonal variations, drought, water availability of the soil, the elevated carbon dioxide, salt stress, shade... Thus, g_s in the plant is very sensitive to the imbalance between climatic demand and water availability of the soil. It is therefore an indicator that reflects instantly, the severity of this umbalance [Bunce, 2001], [Fay, 1995]. Similarly, there have been differences in stomatal conductance between the C3 and C4 species [Begue, 1992].

However, sorghum is less susceptible to stress, compared to other plants such as maize and therefore has a real power of acclimation to it, which makes it difficult to detect it early with g_s measurement [Nagy, 1995].

Acquiring relevant information with stomatal conductance at the plot scale requires an intensive sampling that becomes a limiting factor when it comes to tracking a set of parcels [Jones, 1998].

6.4 Thermal measurement

Thermal detection is mainly used to study the hydrological relationships of plants and more particularly the stomatal conductance, since a major determinant of leaf temperature is the rate of evaporation or transpiration of the leaf. The cooling effect of transpiration arises because a large amount of energy (the latent heat of vaporization) is needed to convert the liquid water to water vapor, and this energy is then removed from the water. Leaf temperature is therefore a tool for stress detection as the leaves are strongly affected by transpiration, which is mainly regulated by stomatal conductance, with an increase in leaf temperature as the rate of transpiration decreases [Li, 2010].

6.4.1 Isopiestic Psychometer

There are several types of psychometers (nonquilibrium, dewpoint and isopiestic) and generally the principle of a psychrometers is based on the measurement of the temperature difference between the air temperature and the dew point inside a chamber containing the tissues whose water potential is to be measured, the Fig. 12 illustrates an exemple of Isopiestic psychrometry tool [Taiz, 2014], [Martinez, 2011].

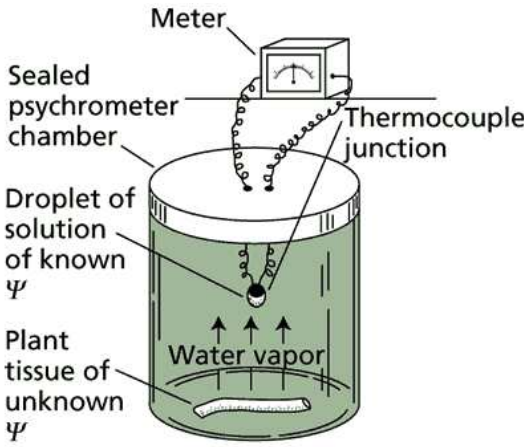

Figure 12 – Illustration of Isopiestic psychrometry technique. Investigators make a measurement by placing a piece of tissue sealed inside a small chamber that contains a temperature sensor (in this case, a thermocouple) in contact with a small droplet of a standard solution of known solute concentration [Taiz, 2014]

Recently, sensors to be installed on plants *in situ* are marketed by the company ICT International, its use is still not widespread. However, in order to successfully measure *in situ* particularly in the field, it is necessary to thermally insulate leaf psychrometers and be cautions in their use (installation, surrounding humidity, radiance...)[Oosterhuis, 1983], [Barrs, 1965] and [Martinez, 2011].

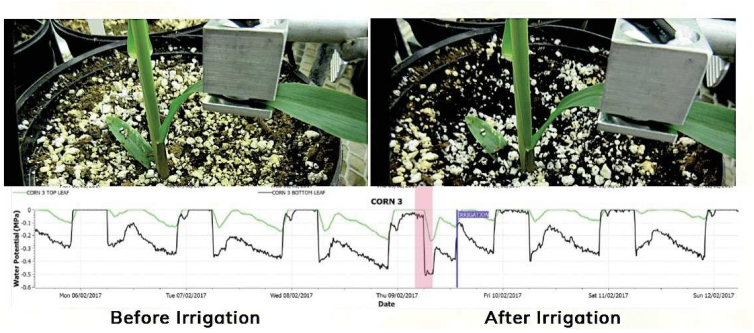

Figure 13 – Monitoring *in situ* of water status (water potential) of rice crops by ICT international http://www.ictinternational.com/casestudies/psy1-leaf-psychrometer/

6.4.2 Thermal Infrared Imaging

More than 40 years have passed since thermography was first applied for plant examination ([Monteith and Szeicz, 1962] and [Tanner, 1963]). However, the effective testing of this technologie was achieved with the recent development of field-portable thermal imaging systems opens up the opportunity to study the distributions of temperature over the area and, if necessary, to include only areas of interest. The Fig. 14 is an example of monitoring of water stress on the leaves of potato plant [Kotchi, 2004].

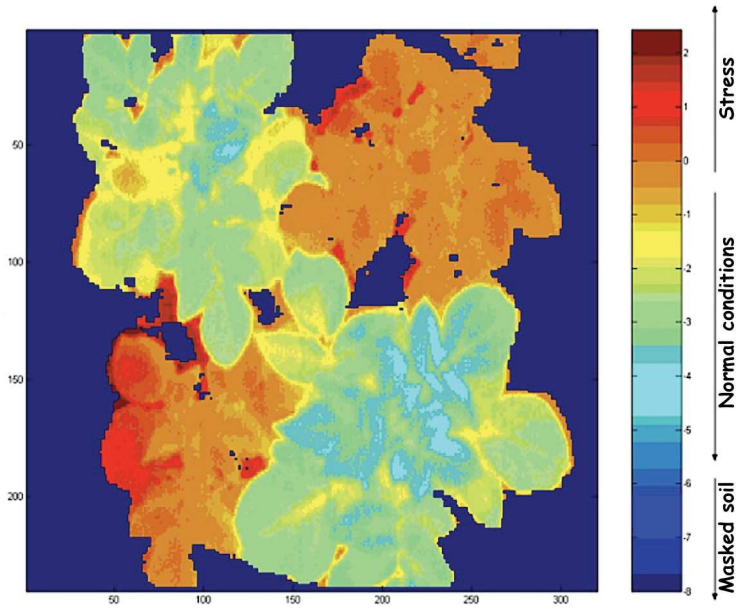

Figure 14 – Mapping by Thermal Infrared Imaging method of potato plants under normal conditions and under water constraints [Kotchi, 2004]

In practice, field application of this approach is likely to be limited (needs a processing) by both the assumption of random leaf orientations and the fact that any image is likely to include non transpiring tissues such as twigs and branches, as well as extraneous surfaces such as soil or even sky with their widely differing temperatures. Furthermore, the radiation, the air temperature, the humidity and the wind speed modify leaf temperature and may mask indications of water stress [Kotchi, 2004].

7 Emerging methods for the measurement of water status

7.1 Terahertz

Assessment of the behavior of plants to water stress using terahertz (THz) is a very recent method that has a proven track record of feasibility and is starting to become involved in the field of plants. This non-destructive method is used for determining changes in leaf moisture content thanks to terahertz waves that are strongly absorbed by water of plant [Hu, 1995], [Hadjiloucas, 1999] and [Breitenstein, 2011].

The reliability of this innovative method under different conditions was verified by monitoring changes in the leaf water content by the measure of transmitted or reflected THz signal. The Fig. 15 shows an exemple of the monitoring of water content in plant during several days by the measure of transmitted THz signal.

Several factors must be taken into account when using this method. Firstly, the detection of terahertz signals is difficult because of the SNR which depends on the studied system. Then,

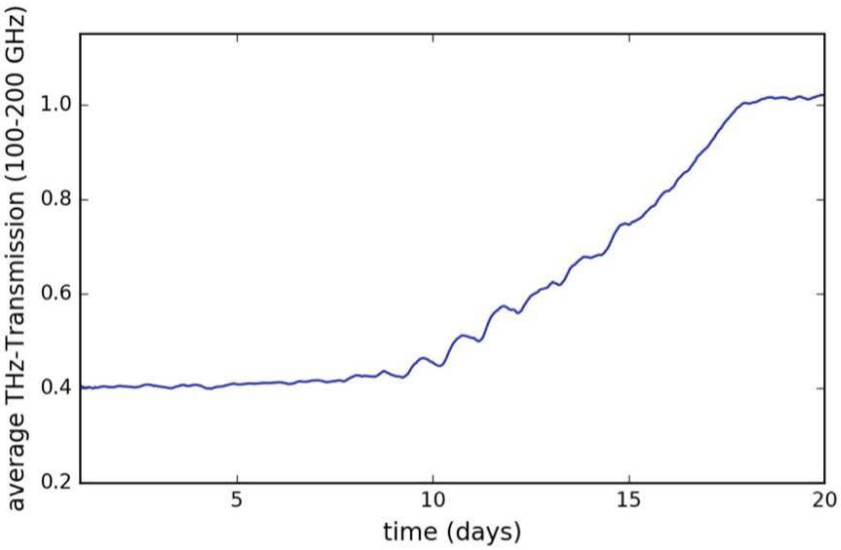

Figure 15 – Relative transmitted amplitude of the THz signal through the leaf of a rye plant under water stress during 20 days [Gente, 2016]

the vapor of the transpiration of the leaves can influence the spectral signature. Finally, the biggest challenge for this method is the atmospheric attenuation that can be severe.

7.2 Dielectric Sensor

Water content monitoring based on dielectric sensor is a new method in plant domain that allows measurements of leaf dielectric properties on living plants under field conditions [Emmerik, 2017]. By measuring the dielectric response of corn Leaves plants with and without water stress, it is demonstrated that there is a significant difference (in the magnitude and in the shift of dielectric responses) in the leaf dielectric properties of stressed and unstressed plants, see Fig. 16.

However, this method is used to study only the early water stress in leaves and the measure depends, in addition to the water content, on the salinity and the temperature of leaves.

8 Sap Flow measurement

8.1 Tomography ultra fast neutron

Neutron imaging is also a recent non-destructive technique in the field of the plant often used for studying the architecture of root systems and the distribution of water in the surrounding

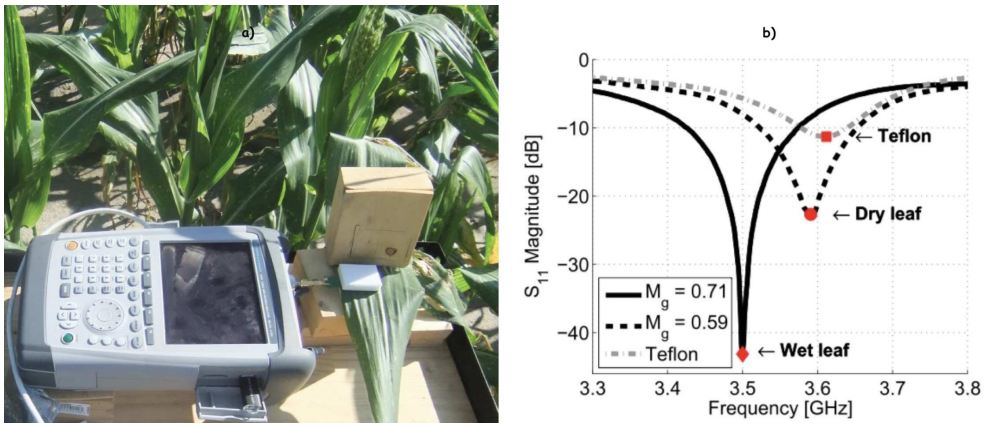

Figure 16 – a) Setup used to measure the dielectric proprieties of leaves b) Measurements of dielectric properties of a Teflon block, a wet leaf and dry leaf [Emmerik, 2017]

soil *in situ* [Moradi, 2011].

Due to its high temporal resolution (a few seconds) and the use of Deuterium D2O as a tracer, this method captures dynamic changes in the local distribution of water in the sample. This is how the application of this method made it possible to visualize the phenomena of water transport in plants, e.g. root uptake [Zarebanadkouki, 2011], axial transport in the xylem [Matsushima, 2009] and embolism [Tötzke, 2013].

A very recent post-harvest investigations of three types of roses, Akito, Milva and Red Giant, with this method yielded flow velocities of approximately $0.75, 1.33$ and $0.31 mm.s^{-1}$, respectively [Matsushima, 2009].

Unfortunately, despite these promising results, this method has not been really us ed because : the set up and D2O is expensive, the data processing is complex and the method is very invasive for the plant.

8.2 Nuclear Magnetic Resonance

The potential of the nuclear magnetic resonance (NMR) method (relaxometry and imaging) to finely investigate plant has recently been demonstrated in pioneering work by [Vans As, 1984 and 1985]. NMR techniques detect water in living tissue and measure its diffusion and mobility in a non-destructive way.

First, The NMR relaxometry investigations is a support for conducting qualitative studies. Thus, it has been possible to study the structural changes taking place within tissues during physiological processes. In tomato, a decrease in the T_1 and T_2 values of around 25% during the ripening of the fruit after harvest has been demonstrated in the placenta, columella and pericarp, and correlated with fruit weight loss [Musse, 2009a].

Then, NMR imaging (MRI) investigations is a support for conducting quantitative studies.

One of the advanced major of this method is the flow measurement using pulsed field gradients (PFG) method [Köckenberger, 1997], [Windt, 2006]. Thus, it has been demonstrated in castor bean seedlings that there are differences in conduction velocities between the xylem having an average flow rate of $0.47mm.s^{-1}$ and the phloem characterized by a velocity of flux of $0.58mm.s^{-1}$ [Köckenberger, 1997]. In the same way, the fluctuations in flow velocities during the daily variations, which can not be explained solely by the variation in the diameter of the conducting vessels, have been demonstrated in Tomato [Köckenberger, 1997]. Thus, it has been determined that the xylem flow can reach a maximum volume flow of $8.0 \pm 0.92mm^3.s^{-1}$ during the day and minimum at night with a volume flow of $2.26 \pm 0.52mm^3.s^{-1}$. On the other hand, according to this study, phloem flux rates do not vary significantly during the day-night cycle and their average volume flow is $0.40 \pm 0.04mm^3.s^{-1}$ [Windt, 2006].

8.3 Motivation to built a NMR device

NMR/MRI devices can provide non-invasive access to the structure and the functioning of plants, to determine quantitative data in real time in particular on the compartmentalization of water, its mobility and dynamics. There is a real interest for phenotyping plants to study their water efficiency. The development of new sensors for precision farming offers interesting prospects for developing strategies to optimize water use and its adjustment on demand. In the context of climate change, understanding the adaptive response of plants under water stress is essential in order to develop new varieties optimized in terms of efficiency of water use in a constrained environment. Portable NMR devices show a great potential for studying plants in their natural environment and their development is still at the beginning [Van As, 1994]. While some authors have occasionally reported the use of NMR for the measurement of water in plants in the fields, this technique is rarely used because of the complexity of its control by physiologists of the plant [Van As, 2007]. In this work, we propose to lift this lock by mobilizing the skills in physics, electronics and plant physiology to develop a new tool to monitor water in the plant based on NMR.

Performing NMR experiments in situ inside climatic chambers, greenhouses or in the fields, rather than transporting plants to the laboratory is a real challenge. There are several examples of NMR/MRI studies performed on plants in their natural environment. For the development of the outdoor NMR system, most of the works proposed the use of permanent magnets based on the U-shaped magnet or Halbach concept which can be manufactured with an homogeneous field and flexible design adapted to the study of living plants in a controlled environment to maintain their stability [Van As, 1994], [Blumich, 2011] & [Windt, 2011 & 2015]. Concerning MRI systems, few works recently have been reported in

greenhouses [Rokitta, 2000], [Okada, 2006], [Kimura, 2011] & [Jones, 2012] but these systems remain difficult to transport and require a considerable amount of electric power. Indeed, outdoor NMR/MRI devices have to deal with the effects of the environmental conditions and mainly the temperature which can act on the drift of the magnetic field. The essential element of the NMR system determining the reliability of the measurements, which is the magnet requires high temperature stability. The heating control of the samples is also critical for measurements of relaxation times as both signal amplitude and relaxation times depend on temperature [Musse, 2017]. Above these environmental constraints are added constraints related to the portability, the autonomy of the system, the respect of the plant geometry and physiology, the ability to make rapid measurements with a significant sensitivity even when the plant is under stress. Hence, the objectives of this work is to design and build a reliable and easy to transport NMR system and to investigate the water status of contrasted sorghum genotypes in a situation of water stress in the fields with the goal to evaluate (quantitatively and qualitatively) the produced biomass in each conditions. Some complementary ecophysiological study acquired in the framework of the BFF project will be confronted to the investigations with the constructed NMR mobile system, in order to validate the relevance of the NMR biomarkers.

Chapter 3. Introduction to the Nuclear Magnetic Resonance

In this chapter, we introduce the basic foundations and concepts necessary to apprehend the physical phenomena of NMR Relaxometry and Imaging studied in this thesis. Next, we present all the elements that compose an NMR system, the technologies used for each element and their limits, wich will help us to develop a low-field device. The documentation and illustrations for this introduction are based in part on the book "Magnetic Resonance Imaging" by [Robert, 2014].

9 NMR principles

9.1 NMR phenomenon

The phenomenon of Nuclear Magnetic Resonance (NMR) was first observed in condensed matter in 1946 by two groups of physicists, Professor Bloch's team at Stanford and that of Professor Purcell at Harvard, as they sought to highlight transitions between nuclear spin states. Today, the scope of this technique has expanded in many scientific fields as : biology [Lauterbur, 1973], health [Damadian, 1971], [Mansfield, 1977] and plant physiology relatively recently [Vans As, 1984 and 1985].

The NMR is based on the fact that nuclei of some atoms have magnetic properties that can be utilized to yield chemical and biological informations. Quantum mechanically subatomic particles (electrons, protons and neutrons) have spin I. In the case of atom nuclei, if the number of neutrons and the number of protons are both even (eg $^{12}C, ^{16}O, ^{32}S$) , the nucleus has no spin. If the number of neutrons plus the number of protons is odd, then the nucleus has a half-integer spin (i.e. $1/2, 3/2, 5/2...$). If the number of neutrons and the number of protons are both odd, then the nucleus has an integer spin (i.e. $1, 2, 3...$).

In quantum mechanical terms, the nuclear magnetic moment $\overrightarrow{M}$ of a nucleus has a random direction but it will be aligned when we apply an external static magnetic field of strength B_0, generated by a **magnet**, in only $2i + 1$ ways, aligned or opposite to the direction of applied field B_0, this phenomenon is called the polarization of nuclear spins. For a single nucleus like proton (^1H) with $i = 1/2$, only one transition is possible between the two energy levels (α

and β) for spins, it corresponds to the quantum number s : a fraction N_α having parallel orientation (s=+1/2), while another fraction N_β having an anti parallel orientation with the applied magnetic field B_0 (s=-1/2) , see Fig. 17 [Levitt, 2008].

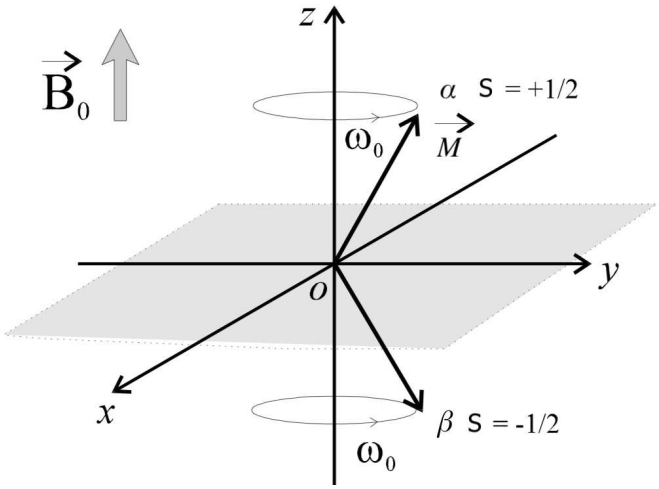

Figure 17 – Illustration of energy levels diagram of a nucleus with spin = 1/2 and the orientation of the magnetic moment when we applied an external static magnetic field B_0

At the thermal equilibrium and according to the Boltzmann equation, the ratio of the populations of spin in the two energy levels N_α and N_β is :

$$N_\alpha / N_\beta = e^{(-\Delta E/kT)} \tag{1}$$

Where k is the Boltzmann constant ($k = 1,38064852 \times 10^{-23} m^2 kgs^{-2} K^{-1}$) and T is the room temperature in Kelvin. ΔE represents the energy needed to make a transition between the two energy states α and β according to Bohr equation:

$$\Delta E = (h\gamma B_0)/2\pi = h\nu_0 \tag{2}$$

Where h is the Planck's constant ($h = 6.62607004 \times 10^{-34} m^2 kg/s$), ν_0 is the frequency, γ is the gyromagnetic ratio of the excited nucleus and B_0 (in Tesla) is the intensity of the magnetic field.

These spins will acquire a macroscopic nuclear magnetization oriented along the B_0 axis. The module of this magnetization is given by :

$$M = (N_\alpha - N_\beta)\gamma^2 h^2 \frac{B_0}{4kT} \tag{3}$$

9.2 Nuclear Magnetization

Every subatomic particle has an electric charge and a mass. It is also characterized by a kinetic moment $\overrightarrow{L}$ and a magnetic moment $\overrightarrow{M}$ which characterizes its intrinsic rotational motion ($\overrightarrow{M}$ is proportional to $\overrightarrow{L_s}$: $\overrightarrow{M} = \gamma\overrightarrow{L_s}$, where γ is the gyromagnetic ratio related to the magnetic moment and the spin number for a specific nucleus). The application of a static magnetic field $\overrightarrow{B_0}$ on a population of spins of magnetic moment $\overrightarrow{M}$ will generate a couple of forces $\overrightarrow{\Gamma}$ that will modify the kinetic moment according to the fundamental principle of dynamics [Callaghan, 1991].

$$\overrightarrow{\Gamma} = \frac{d\overrightarrow{L_s}}{dt} = \overrightarrow{M} \wedge \overrightarrow{B_0} \tag{4}$$

Thus, the movement of the magnetic moment can be written as :

$$\frac{d\overrightarrow{M}}{dt} = \gamma\overrightarrow{M} \wedge \overrightarrow{B_0} \tag{5}$$

The solution of this equation (Eq. (5)) highlights the movement of precession of $\overrightarrow{M}$ around the axis of $\overrightarrow{B_0}$ (defined in our coordinate system as about the z axis Fig. 17).

The rotational axis of the nuclei spin cannot be oriented exactly parallel (or anti-parallel) with the direction of the applied field B_0 but precess (motion similar to a gyroscope) around this magnetic field at a constant angle, with an angular velocity given by the expression (for further details see [Kennouche, 2014]) :

$$\frac{d\overrightarrow{M}}{dt} = \overrightarrow{\omega_0} \wedge \overrightarrow{B_0} \tag{6}$$

From the Eq. (5) and Eq. (6), we found :

$$\omega_0 = -\gamma B_0 \tag{7}$$

Where ω_0 (rad/s) is the precession rate which is also called the Larmor precession and $\gamma = 42.577 MHz/T$ for protons or hydrogen nucleus.

After the polarization of the spins by the magnetic field $\overrightarrow{B_0}$, and to switch from the equilibrium state to the excited state, it must be subjected to the action of an oscillating magnetic field called $\overrightarrow{B}_{rf}$. This radiofrequency (RF) field is, characterized by a pulsation ω_{rf} and a phase φ, produced by a **RF coil** which serves to collect the variations of the magnetization of the sample, but generally also to excite the sample when it is crossed by a sinusoidal alternating current. This excitation magnetic field can be decomposed into two

components: $\overrightarrow{B}^{+}_{rf}$ rotates in the same direction as $\overrightarrow{\omega_0}$ at a speed of ω^{+}_{rf} and $\overrightarrow{B}^{-}_{rf}$ in the opposite direction at a speed of ω^{-}_{rf} according to :

$$\overrightarrow{B}_{rf}(t) = \overrightarrow{B}^{+}_{rf}(t) + \overrightarrow{B}^{-}_{rf}(t) = B_1(e^{j(\omega_{rf}t+\varphi)} + e^{-j(\omega_{rf}t+\varphi)}) \tag{8}$$

Thus, the Eq.(5) can be expressed by

$$\frac{d\overrightarrow{M}}{dt} = \gamma\overrightarrow{M} \wedge (\overrightarrow{B_0} + \overrightarrow{B}_{rf}) \tag{9}$$

In practice, the NMR experiments are related to a population of spins, sample. In the presence of a magnetic field and at thermal equilibrium, the sum of these different spin populations (or magnetic moments) gives a macroscopic magnetization M_0, aligned with B_0. After the application of RF pulse with an amplitude A_p and during a finite time called t_p, the magnetization vector will be tilted by an angle ($\theta = \gamma B_1 t_p$): the spins will come out of their equilibrium state [Robert, 2014]. After stopping this pulse, the magnetization returns to its equilibrium position M_0, an electromagnetic (EM) field is associated to precession and the electric field associated to this EM field induces a signal in the **RF coil** [Bloch, 1946]. This evolution of the magnetization over time is called relaxation and it is characterized by two times constants : T_1 and T_2 relaxation times.

$$\frac{d\overrightarrow{M}(t)}{dt} = \gamma\overrightarrow{M}(t) \wedge (\overrightarrow{B_0} + \overrightarrow{B}_{rf}) - R(\overrightarrow{M}(t) - \overrightarrow{M}_0) \tag{10}$$

R_s is the relaxation matrix which is written :

$$R_s = \begin{pmatrix} \frac{1}{T_2} & 0 & 0 \\ 0 & \frac{1}{T_2} & 0 \\ 0 & 0 & \frac{1}{T_1} \end{pmatrix} \tag{11}$$

These observed NMR parameters result in the decomposition of the magnetization vector (thanks to solutions of Bloch equations, see Annex 1.) into two transverse components M_x and M_y and one longitudinal component M_z according to :

$$M_z(t) = M_0(1 - e^{(-t/T_1)}) \tag{12}$$

$$M_x(t) = M_0 cos(\omega_0 t)(1 - e^{(-t/T_2)}) \tag{13}$$

$$M_y(t) = M_0 sin(\omega_0 t)(1 - e^{(-t/T_2)}) \tag{14}$$

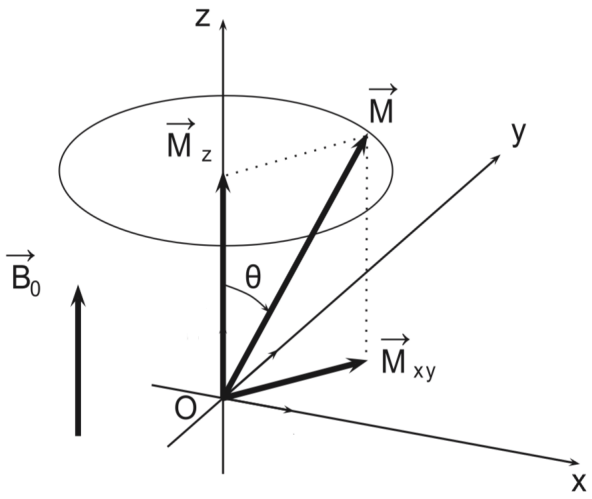

Figure 18 – Illustration of transverse and longitudinal components of macroscopic magnetization

9.3 Collecting the NMR signal

The RF coils allow to create the B_1 field and detect the NMR signal from the sample at Larmor frequency. It is known that, the efficiency of coil to detect the magnetization is proportional to its ability to create a B_1 field in the sample for a current I under the reciprocity theorem [Hoult, 1976], which implies that transmit and receive efficiency are related. Indeed, the return to the equilibrium of the magnetization is accompanied by the emission of an electromagnetic field (EM) whose electrical component will be detected by RF coil, thereby obtaining the NMR signal also called FID.

The elementary induced voltage ($\delta e(t)$) in a coil caused by an elementary magnetic field moment ($\delta m(t)$) can be expressed thanks to the vector potential formalism :

$$\overrightarrow{A}(\overrightarrow{r},t) = \frac{\mu_0}{4\pi}\frac{\delta\overrightarrow{m}(\overrightarrow{r},t)\times\overrightarrow{r}}{\overrightarrow{r}^3} \tag{15}$$

The magnetic field $\overrightarrow{B}_1$ can be related to the potential vector by :

$$\overrightarrow{B}_1(\overrightarrow{r},t) = \overrightarrow{Rot}\,\overrightarrow{A} \tag{16}$$

The total flux in a section S can be written as:

$$\phi = \oiint_S \overrightarrow{B}_1(r,t)d\overrightarrow{S} \tag{17}$$

Applying the Stock's theorem, we obtain:

$$\phi = \oint_{(L_s)} \overrightarrow{A}d\overrightarrow{L}_s \tag{18}$$

Using Eq. (15) and the product of the mixed vector, the expression of the flux becomes:

$$\phi = \frac{\mu_0}{4\pi} \oint_{(L_s)} \frac{d\overrightarrow{L}_s \times \overrightarrow{r}}{\overrightarrow{r}^3} \delta\overrightarrow{m} \tag{19}$$

Where μ_0 is the vacuum permeability.

Then, we identify in Eq. (19) the expression of the magnetic field according to the law of Biot & Savart :

$$\overrightarrow{B}_1(\overrightarrow{r}, t) = \frac{\mu_0 I}{4\pi} \oint_{(L_s)} \frac{d\overrightarrow{L}_s \times \overrightarrow{r}}{\overrightarrow{r}^3} \tag{20}$$

The expression of flux can be written :

$$\phi = -\frac{\overrightarrow{B}_1(\overrightarrow{r}, t)}{I} \delta\overrightarrow{m} \tag{21}$$

The voltage e due to the circulation of this current along the coil is then function of the variation of the flux of the magnetic field through a section of the coil according to the law of Lentz [Hoult, 1990] can be written :

$$\delta e = \frac{-d(\overrightarrow{B}_1 / I\delta\overrightarrow{m})}{dt} = \frac{-d\phi}{dt} \tag{22}$$

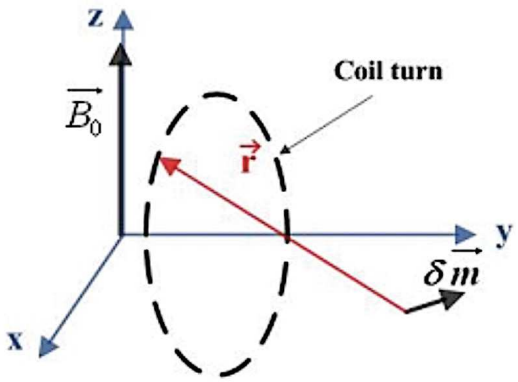

Figure 19 – Illustration of the origin of NMR signal : the return to equilibrium of magnetization induces a voltage e in the coil.

10 NMR Relaxation measurements

10.1 Measurement of spin lattice relaxation time T_1

10.1.1 Spin lattice relaxation time T_1 :

The T_1 relaxation time, also known as the spin-lattice relaxation time, quantifies the rate of transfer of energy from the nuclear spin system to the surroundings molecules (the lattice).

This is a relaxation in the z-direction and leads to an exponential recovery to Boltzmann equilibrium M_0 [Robert, 2014].

10.1.2 Methods to measure T_1

In conventional NMR, there are several techniques commonly used to measure T_1 :

- The first method for measuring T_1 is known as **Saturation-Recovery :**

  First, a "pulse saturating sequence" cancels the magnetization perpendicular to the z axis. Then, a delay τ , is allowed, during which spin-lattice relaxation occurs causing M_z to go from *zero* to its equilibrium value of M_0, the FID is recorded, see Fig. 20. The experiment is repeated with different delays τ, allowing determination of the T_1 value in s. T_1 is therefore defined as the time for which the longitudinal magnetization Mz returns to 63% of its final value.

  The equation governing this behavior as a function of the time t :

$$M_z(t) = M_0(1 - e^{-t/T_1}) \tag{23}$$

- The second method for measuring T_1 is known as **Inversion-Recovery :**

  First, a π pulse inverts the magnetization along the -z axis. A time period, τ, is allowed, during which spin-lattice relaxation occurs causing M_z to go from the value of $-M_0$ through zero to its equilibrium value of M_0. Then, a $\pi/2$ pulse is applied and the FID is recorded, see Fig. 20. The experiment is repeated with different τ delays, allowing determination of the T_1 value by fitting the curve.

  The equation governing this behavior as a function of the time t :

$$M_z(t) = M_0(1 - 2e^{-t/T_1}) \tag{24}$$

- The last one is the **Flip angle or Ernst angle :**

  This method is widely used in fast NMR imaging for determining T_1. Here, the magnetization is tilted with multiple angles at constant τ ($\tau << T_1$). The magnetization is maximized at the Ernst angle (α_{Ernst}) [Ernst, 1966].

  The equation governing this behavior as a function of the angle this time is :

$$\alpha_{Ernst} = arcos(e^{(-\tau/T_1)}) \tag{25}$$

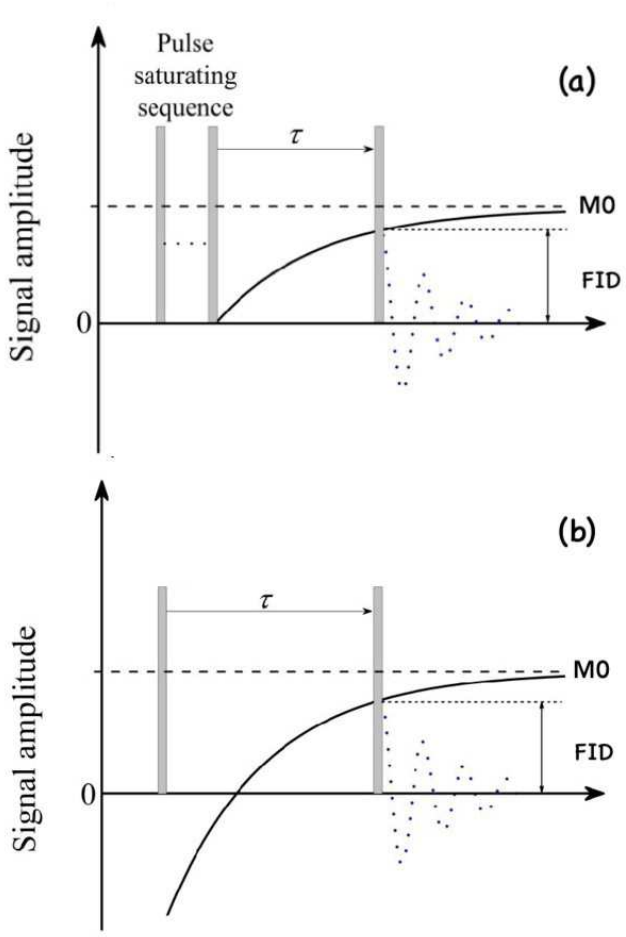

Figure 20 – Illustration of the saturation recovery (a) and inversion recovery (b) pulse sequences [Shakhovoy, 2015].

10.2 Measurement of spin spin time relaxation T_2

10.2.1 Spin-spin time relaxation T_2 :

The spin-spin (or transverse) relaxation time T_2 is used to reach a molecular interaction and dynamic informations, it corresponds to the rate of the decay of the magnetization within the XY plane. The T_2 decay of the signal also depends on the inhomogeneity of the magnetic field B_0. The observed signal therefore depends on the "real" T_2 of the observed tissue but it also contains the inhomogeneities of the field. This decay is called T_2^* and represents a combination of external field induced due to inhomogeneities (T_2') and the T_2 of the sample [Robert, 2014].

$$\frac{1}{T_2^*} = \frac{1}{T_2} + \frac{1}{T_2'} \tag{26}$$

10.2.2 Methods to measure T_2

- The **spin echo** method is based on the application of two pulses : a $\pi/2$ pulse followed by a π called "refocusing pulse". The NMR signal observed following an $\pi/2$ pulse decay according to T_2^* due to both spin relaxation and inhomogeneous effects which cause different precession rates. However, the application of π pulse removes these effects and allows to observe the decay of signal according to T_2, see Fig. 21, this is called the "spin echo".

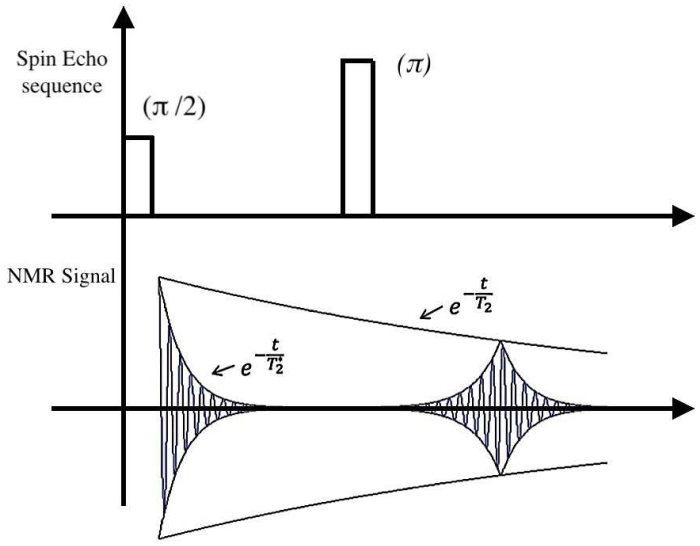

Figure 21 – Illustration of Spin Echo sequence :

- The **Carr-Purcell-Meiboom-Gill (CPMG)** is based on the application of a $\pi/2$ pulse following by a "train" of π pulses applied at intervals $\tau, 3\tau, 5\tau, 7\tau$, etc. Echoes are then observed every echo time TE because the dephasing resulting from molecular interactions the protons can no longer be completely refocused. The magnitude of the multiple echoes decreases successively as a consequence of T_2 dephasing, see Fig. 22 .

  The equation governing the behavior of T_2 decay as a function of the time t after its displacement is (see Annexe.1):

$$M_{xy}(t) = M_{xy0}e^{(-t/T_2)} \tag{27}$$

  Where M_{xy0} is the initial transverse magnetization. T_2 corresponds to the time in s taken by the transverse magnetization to decrease to 37% of its initial value.

The NMR parameters, spin-spin relaxation time (T_2) and spin-lattice relaxation (T_1), are known to be highly relevant to investigate both microscopic and macroscopic changes in

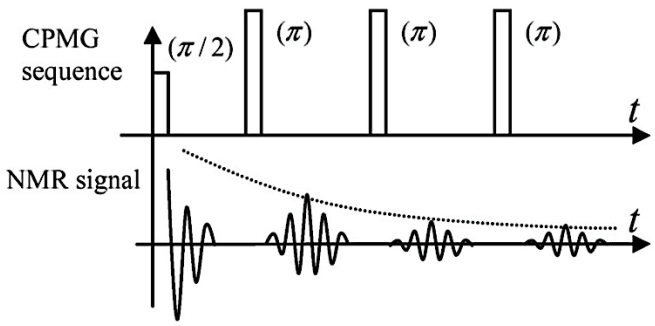

Figure 22 – Illustration of CPMG Sequence. The amplitude of the 'echo' signal decays according to T_2 relaxation time

structure of plant tissue as shown in the investigation of tomato during post-harvest maturation by MRI at $0.2T$ by [Musse, 2009a], [Duval, 2004]. The variations in T_2 were between 180 and $300ms$ while changes in T_1 were between 380 and $500ms$ for different types of tissues : vacuolar, cytoplasmic and parietal. The T_1 and T_2 depends on the intensity of the field B_0 in which the measurement is achieved [De Graaf, 2006],[Bottomley, 1984].

With the combination of the magnet and the coil, we can do relaxometry experiments (M_0, T_1, T_2) and this allows to have quantitative or qualitative informations about the studied sample.

11 Spatial localization of the NMR signal

During the first half of the 20th century, Felix Bloch and Edward Purcell described the phenomenon of NMR, but it was the next generation of scientists in the 1970s who discovered how to localize the NMR signal.

Paul Lauterbur published in 1973, his experimental device which implied for the first time, in addition to the magnet and the RF coil, another part called "gradients coils".

The so called "gradient-coil" produces a magnetic field applied in the same direction as the static field B_0 but with a magnitude that linearly depends on the position (mT/m). By applying this magnetic field gradients, it was possible to obtain the projections of the NMR signal and thus it was localized on a slice-by-slice basis.

The magnetic field of the gradient is much lower than B_0 and are active during NMR experiments for a few milliseconds [Lauterbur, 1973], [Bernstein, 2005].

The effective magnetic field after application of gradient can be expressed :

$$B = B_0 + nG_n \tag{28}$$

$$f = f_0 + \gamma n G_n \tag{29}$$

where n is the direction of gradient and G_n his intensity.

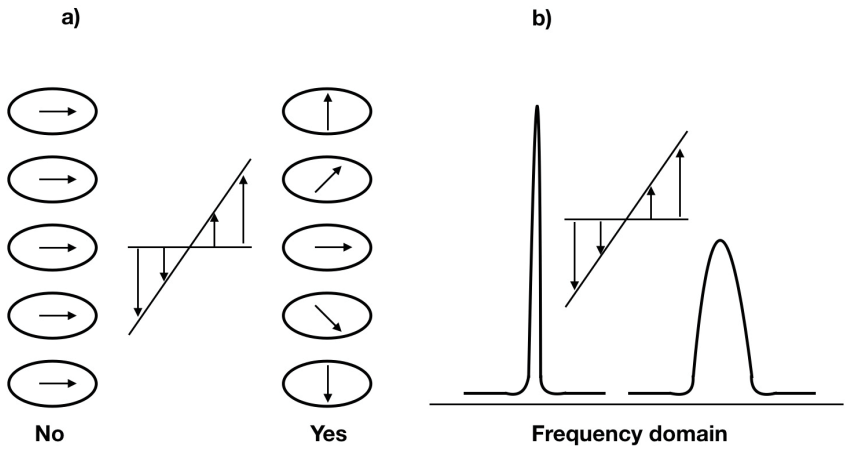

Figure 23 – Illustration of the effects of a gradient a) orientation of the magnetization of spins and b) the line width of a spectrum of the same sample

The Fig. 23 shows the effect of the gradient on spectrum width. Indeed, the gradient tends to explode the line width of a spectrum because the spins do not precess at the same frequency. This effect gives us a spatial signature about the localization of spins.

Thus, the localization of the nuclear magnetic resonance signal is obtained by the determination of the position by their resonance frequency according to Eq. (30). To obtain a linear variation of the frequency with the position, one gradient minimum is used.

The MR images are generated by means of the sequential application of three gradients to spatially encode the contributions of volume elements (voxels) from the selected region to the total signal in three directions : x, y and z, see Annex 3.

$$B(x, y, z) = B_0 + xG_x + yG_y + zG_z \tag{30}$$

12 NMR instrumentation : introduction to the magnets and RF coils

12.1 Magnets

Because of its preponderant role in the NMR experiment, the development of the magnet, which produces the B_0 magnetic field, has focused special attention. The choice of a technology and the structure of magnet depends on the application and the desired performances :

intensity, homogeneity, stability of the field, the cost and the complexity of realization. To address planta agronomic studies in *naturae*, in addition to these performances, the NMR instrument should be light in order to be easily moved.

It is known that, the ^1H NMR signal is roughly quadratically dependent on the **intensity** of the magnetic field B_0 and its **homogeneity** [Vo-Dinh, 2002]. This consideration has historically oriented to design higher magnetic fields, up to 31T [Yoshisa, 2011]. Nevertheless this magnetic field "race" has made the NMR magnet more and more sophisticated (cooling is mandatory, bulky and extremely heavy) and therefore not transportable.

In this part, we will see the types of magnets that will allow to create a magnetic field B_0.

12.1.1 Resistive Magnet :

The resistive magnets consist of coils providing homogeneous magnetic field at the center. Different type of coils are encountered, the most commonly encountered are : the solenoid and Helmholtz coil.

The other constraint for the NMR dedicated to agronomic studies is the "accessibility". Indeed, the configuration of Helmholtz coils (unlike the solenoid) allows us to consider experiments where the integrity of the plant is maintained.

The Helmholtz coils consist of two circular parallel coils of the same radius R placed at a distance equal to their radius. The magnetic field intensity produced at the center of a "N_{turn}" turns coil flown by an electrical current of magnitude I, is given by :

$$B_0 = \frac{4}{5}^{3/2} \frac{\mu_0 N_{turn} I}{R} \tag{31}$$

These magnets are widely used to produce low field otherwise the system overheats and requires cooling. Among the NMR work with a resistive magnet, we can cite the prototype at $4.5mT$ of Asfour group [Asfour, 2011]. The weak points of these magnets are the limitation of the intensity of the magnetic field B_0 produced which is proportional to its weight and its energy consumption.

12.1.2 Permanent Magnet :

A permanent magnet is a magnetic material which owns a magnetization (thanks to a dedicated manufacturing process under a strong magnetic field) and creates a magnetic field.

For a long time, the progress in the field of materials made it possible to hope the replacement of the superconducting magnets by the low cost permanent magnets.

Homogenous cylindrical permanent magnet based on Halbach work [Halbach, 1980] have inspired relatively recent NMR permanent magnets designs [Raich, 2004].

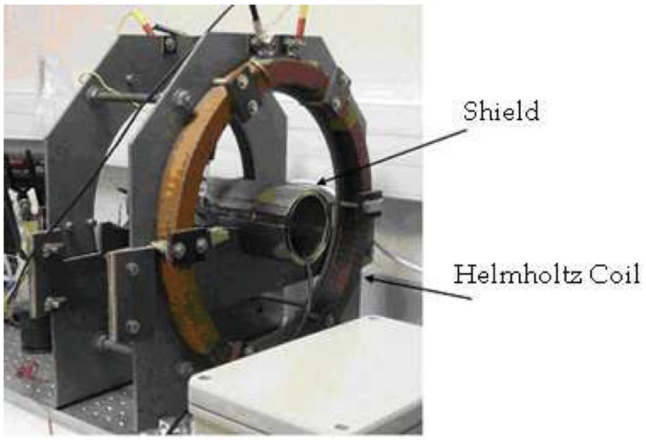

Figure 24 – Illustration of prototype of Helmholtz coil at $4.5mT$ [Asfour, 2011]

The Halbach structure consists of segments of permanent magnets joined together in an array to create the homogenous field in transverse plan as shown in Fig. 25. Its magnetic field amplitude and homogeneity can be controlled by using some analytical theory tool [Hugon, 2010].

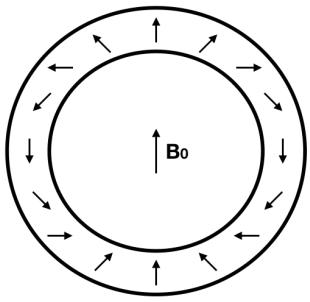

Figure 25 – Illustration of structure of Halbach, each segment represents a elementary permanent magnet

Among the many works carried out, we can mention the prototype developed by the Sakellariou group in 2010 [Sakellariou, 2014], which has an interesting particularity : the possibility of controlling the inclination of the magnetic field, see Fig. 26. In the NMR in solids and MRI in oriented tissue, this rotation at the called "Magic Angle" eliminated the effects of anisotropic interactions from the spectra, leads to high-resolution, high-sensitivity isotropic signatures of metabolites and increase the T_2 [Hugon, 2010], [Bydder, 2007].

Often, these permanent magnets require shimming system used to compensate the inhomogeneity caused by the material's imperfection, assembly inaccuracies and the tolerance of the manufacturing. In addition, the main weakness of this magnet is its field stability due to thermal drift which limits where the measurement is achieved. NMR measurements achieved

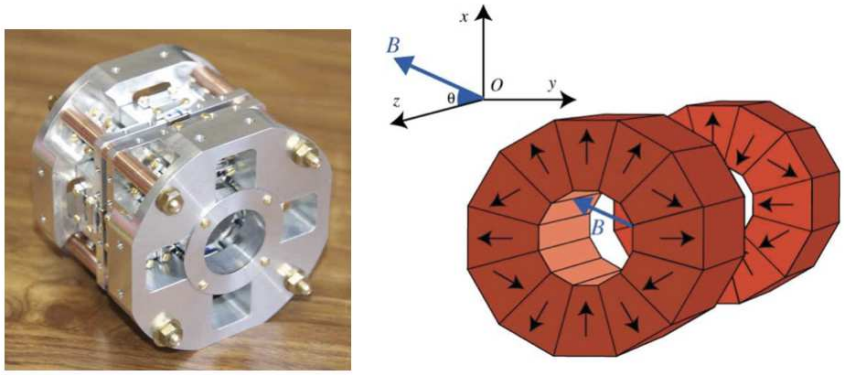

Figure 26 – Illustration of prototype with the inclinaison of the field B_0 can be controlled and photograph of its assembly at $0.22T$ [Sakellariou, 2014]

in a "Reasonable" environment where the daily variations of temperature is a few degrees seems very complicated, this limits the fields experiments [Hugon, 2010].

12.1.3 Electromagnet :

An electromagnet (invented in 1823 by William Sturgeon and improved by Joseph Henry) is a device consisting of a wrapping coil of wire around a soft iron core or other ferromagnetic material. In fact, the shape of the magnetic core material makes it possible to concentrate the effect of the magnetic field and reduce the losses, in particular that caused by the eddy currents. Thus, the strength of a magnetic field produced by an electromagnet depends on the number of turns of coil N_{turn} flown by a current of magnitude I, the shape of the core material and its ability to magnetize which depends on its type through its "magnetic permeability μ" [Nave, 2006].

However, and despite multiple studies in the design of electromagnet, there is a real fundamental problem in the optimization of the geometry : it is necessary to model its magnetic performances and its thermal performances. The electromagnets are often used to produce high field and thus require a cooling system, generally water, to dispose the overheating of the coil [Herlach, 2002], [Haignere, 1976] .

12.1.4 The superconducting Magnet :

A superconducting magnet is a multi turn coil made of superconducting wire with zero resistance when it is cooled below a critical temperature close to absolute zero ($0K$) by immersing it in liquid helium. The coil and liquid helium are kept in a large dewar. This dewar is typically surrounded by a liquid nitrogen ($77.4K$) dewar, which acts as a thermal buffer between the room temperature air ($293K$) and the liquid helium. Nevertheless, the complexity, the

weight and the cost of cooling limit its use to indoor experiments. With these systems the homogeneity is about few ppm [Braun, 1996].

Summary of magnets used in NMR				
Criteria/Magnets types	Res. magnets	Per. magnet	Electromagnet	Sup. magnet
Natural homogeneity	++	−	−	+
Intensity of B_0	− −	+	+	++
Overheating (K)	− −	++	−	Not App.
Stability in Temp.	++	− −	−	Not App.
Portability	+	++	++	Not App.
Accessibility	++	++	++	−
Manufacturing	++	+	−	− −
Cost	++	++	−	− −

Table 2 – Summary of the strengths and weaknesses of the different magnets used in NMR

We conclude from this part that the resistive magnet is a good candidate for our problematic (stability as a function of temperature, simple configuration, possibility of making it mobile...) if we can improve its homogeneity.

12.2 Inductive RF Coils

RF coils are key components in determining the efficiency of NMR. The RF coil can be used as Transmitter (Tx) to create B_1 field or Receiver (Rx) to detect NMR signal or in both modes. By using independent Transmitter and / or Receiver, the design of coil can be practical, which opens up great design flexibility to maximize NMR performance especially at low field.

12.2.1 Overview of RF coil configurations

It is known that, the RF coils can be classified into two categories : the volume RF coils [Coillot, 2016a] and the surface RF coils [Ginefri, 2001 and 2005]. The choice of RF coil type depends strongly on the application and also the intensity of magnetic field. The common configurations for volume coils include Solenoid coil, Birdcage Coil and Saddle Coil presented in Fig. 27. The choice between these volumic RF coils will result in a compromise between homogeneity, sensitivity and adequacy to the sample (shape and position of B_1 with respect

with B_0) [Mispelter, 2006].

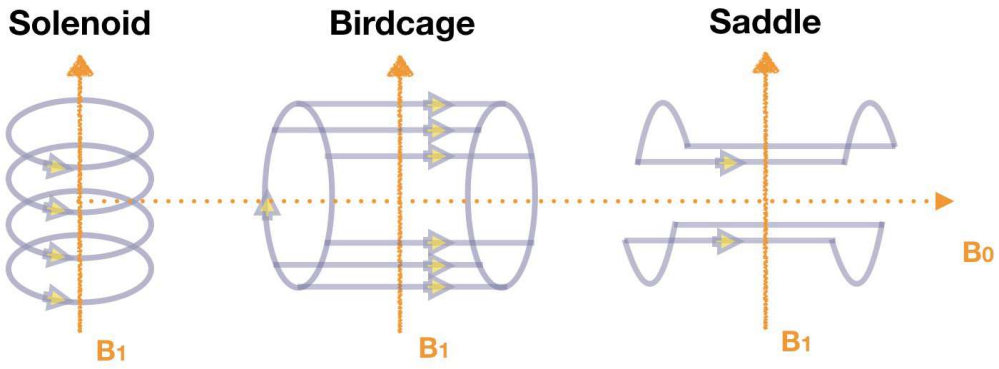

Figure 27 – Illustration of the common RF coil used in NMR : the magnetic field B_1 resultant is represented for each RF coils.

12.2.2 RLC model : Tank circuit

The NMR volumic coil is an electric dipole which can be modeled by :

- A induced voltage (e) which results from the variation of the magnetic field following the return to equilibrium of the spins according to Eq. (22)
- An inductance L (in H) which describes the storing of magnetic energy according to :

$$W_m = \iiint_V \frac{1}{2}\frac{B^2}{\mu_0} dV = \frac{1}{2} L I^2 \tag{32}$$

  Where V is the volume of the coil. In the case of solenoid coil, an estimation of the equivalent inductance value can be obtained by using Wheeler formulae [Wheeler, 1928] :

$$L = \frac{N_{turn}^2 \mu_0 D^2}{0.45D + l_c} \tag{33}$$

  Where D is the diameter of the Solenoid, l_c is the coil length and μ_0 is the vacuum magnetic permeability.

- The resonance occurs in the coil around $\lambda/2 = l_w$ accounts for the propagative electromagnetic wave phenomenon and light velocity and its reflection. It can be represented by a capacitor (C) in parallel with the inductance whose value is such as:

$$C = \epsilon_0 \mu_0 \frac{l_w}{\pi L^2} \tag{34}$$

Where ϵ_0 is the vacuum permittivity and l_w is the length of wire.

And $\omega_0 = 2\pi c/\lambda$

- A resistance R_{ac} which gives account for the losses in the coil (by Joule's effect) and the sample (magnetic et dielectric losses). At low frequency and/or for small sample the dominant losses mechanisms will be the resistive losses by Joule's effect [Mispelter, 2006]. This phenomenon is governed by three major effects : the skin effect (at a high frequency, the current tends to flow only on the surface of the conductors), the lateral skin effect (the current density will tend to flow at the the extremities of the coil [Belevitch, 1971]) and the the proximity skin effect (the current density between neighbor conductors will be strengthened especially at the extremities of the coil). The resistive losses in a coil being described in an elegant form in the PhD thesis work of Erna hamburger [Hamburger, 1937].

  We will consider a simplified modeling by taking into account the skin effect in round wire. Thus, in AC mode and for cylindrical conductors, with a wire radius of r_c, a section S, a resistivity ρ and a frequency f, this resistance can be expressed :

$$R_{ac} = \frac{R_{dc} r_c}{2\delta} \tag{35}$$

  Where

$$\delta = \sqrt{\frac{\rho}{\pi \mu f}} \tag{36}$$

  The R_{dc} is the resistance in DC mode, this term can be calculated :

$$R_{dc} = \rho \frac{l_w}{S} \tag{37}$$

  The Eq. (35) and Eq. (36) show that, at high frequency we must consider the skin effect.

Then, a RF coil can be represented by the RLC model also called Tank circuit showed in Fig. 28. The impedance of this model can be expressed :

$$Z(j\omega) = \frac{R_{ac} + jL\omega}{1 - LC\omega^2 + jR_{ac}C\omega} \tag{38}$$

The transmittance of the coil can be expressed:

$$T_z(j\omega) = \frac{V_{out}}{e} = \frac{1}{1 - LC\omega^2 + jR_{ac}C\omega} \tag{39}$$

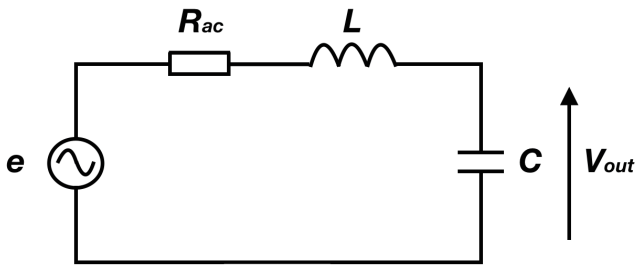

Figure 28 – RLC representation of coil

The study of the behavior of transmittance of coil as function of its electrical resonance ω shows a strong amplification at Larmor frequency : $\omega = \omega_0$ [Coillot, 2018].

When we want to connect our coil to the NMR system, we must take into account two rules:

- The first is the resonance frequency : the electrical resonance frequency of coil that should be **tuned** to the gyromagnetic frequency according to Eq. (7). The coil resonance should coincidate with the Larmor frequency. In this aim, the coil is usually tuned using an adjustable capacitor C_t in parallel with the coil.

  From the calculation of the impedance equivalent (with $Z_t = 1/jC_t\omega$) according to the RLC model presented in Fig. 29, we can deduce:

$$C_t = \frac{1}{\omega}\frac{(R_{ac}C\omega^2) + (1 - LC\omega^2)^2}{L\omega(1 - LC\omega^2) + R_{ac}^2C\omega} \tag{40}$$

- The second point is to **match** the coil so that its impedance is compatible with the rest of the NMR system (50Ω). This rule of electronics is justified by the need to maximize the transmitted power and limit the reflected power that could damage the input stage of the RF amplifiers.

  From the calculation of the impedance equivalent (with $Z_t = 1/jC_t\omega$ and $Z_m = 1/jC_m\omega$) according to the RLC model presented in Fig. 29, we can deduce:

$$C_m = \frac{2Z_0L\omega^2 - \sqrt{b}}{2Z_0(L^2 + R_{ac}^2\omega^2)} \tag{41}$$

$$with\ Real(Z) = Z_0\ and\ Img(Z) = 0 \tag{42}$$

$$b = 4(Z_0 L\omega^2)^2 - 4(Z_0 - R_{ac})Z_0(L^2\omega^4 + R_{ac}^2\omega^2) \tag{43}$$

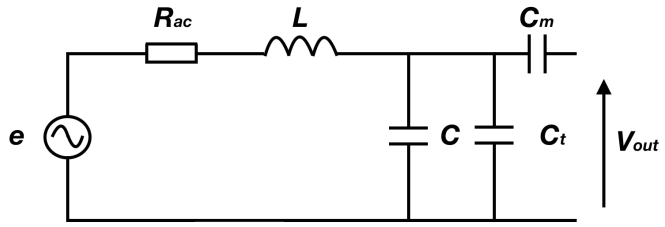

Figure 29 – RLC representation of coil with its Tuning Matching circuit [Coillot, 2016a]

We conclude that the resonant frequency of the coil depends first of all on its dimensions, but also on elements added to it and the volume of the coil must be adapted to the sample to reduce the losses: it is the filling factor.

12.3 Sensitivity and Signal to Noise Ratio

In addition to the signal, It is necessary to consider the contribution of noise voltage which comes principally from the thermal agitation of charge carriers (electrons, ions) in the conductive material constituting the coil. The charges of a conducting medium (electrons or ions), even if the latter is not crossed by a current, are not perfectly immobile. The random movement of these charges is of Brownian type. More precisely the fluctuation-dissipation theorem states that the efficient value of the noise voltage (σ) in a conductor are related to its resistance (R) and its temperature (T) according to :

$$\sigma = \sqrt{4kTR_{ac}\Delta f} \tag{44}$$

Where Δf is the bandwidth of the detection system.

Thus, considering an input source of noise and according to the RLC model represented in Fig. 28, we deduce the spectral power density (PSD) voltage [Coillot, 2016a] :

$$PSD_{vout} = \frac{4kTR_{ac}}{1 - LC\omega^2 + jR_{ac}C\omega} \tag{45}$$

Finally, the SNR is simply the ratio between the output signal V_{out} which can be deduced from Eq. (39) and the PSD of the input noise :

$$SNR = \frac{V_{out}}{PSD_{V_{out}}} = \frac{e}{\sqrt{4kTR_{ac}\Delta f}} \tag{46}$$

The evaluation of the SNR performance on the NMR coil is usually performed through the Q factor evaluation.

The Q_{Factor} value of the RLC coil can written as :

$$Q_{Factor} = \frac{\omega L}{R_{ac}} \tag{47}$$

In practice, the quality factor is defined as the ratio of the center frequency to the bandwidth at $-3db$:

$$Q_{Factor} = \frac{f}{\delta Bw_{-3db}} \tag{48}$$

the Eq. (48) shows that the bandwidth value is related to the coil efficiency.

In this chapter, we will remember that the NMR signal is proportional to the intensity of field and to the efficiency and the homogeneity of RF coil. Adding a gradients to the system permits to localize these spins and determines more informations about the molecular dynamics or produces MRI images. We have also summarized through the literature the technologies of the magnets, RF coils and gradients and evoke their strong points and their weaknesses to guide us in our choice to develop our portable NMR device without compromising our future experiments.

Chapter 4. NMR instrumentation : Development of a portable NMR system at low field

Low field NMR is a non invasive technology that concerns NMR measurements in mT range and aims to offer advantages like cost and no need for a special maintenance. Besides these desirable features, the low field NMR will suffer from a significant loss of sensitivity which has led us to investigate the different possibilities of enhancement : homogeneity of the magnet and SNR of the RF detection part (coil and low noise amplifier).

This chapter details some ways to push the boundaries of the SNR at low field while considering the constraint of miniaturization and versatility of the design to keep the plant intact. The goal is to transport NMR ^1H in the fields to access to a large palette of agronomics plants of interest : sorghum, tomato, vineyards.

13 Design of RF coil for Low Field : Homemade innovative active Tuning-Matching circuit

The RF coils used in NMR experiments are designed to generate a transverse homogeneous magnetic field inside the region of interest (ROI) with the minimum power consumption or, according to the reciprocity principle, with the maximum signal to noise ratio. It is known that this device can be modeled by a conventional tank circuit where the inductive coil is represented by a RLC circuit and to this are added elements for Tuning to the Larmor frequency and Matching the impedance to the 50Ω Fig. 29.

A challenge of low field NMR is to find the best compromise between the lowest possible magnetic field (which will reduce the power consumed, in the case of a resistive coil to reduce the mass of the magnet (whatever the technology) and to reach a sufficiently high SNR enough to perform a measurement that can be used on a plant in a "reasonable" time in order to be able to monitor the water statut *in natura*.

To determine this compromise, we investigated the SNR at different B_0 by designing an optimized coil for each frequencies that coincide with the gyromagnetic resonance of the

considered B_0.

For this, several RF coils optimized for different proton resonance frequencies ($1, 2, 5$ and $10MHz$), have been designed according to Tank model (Eq. (33) to Eq. (41)) and 3D printed for the mechanical support part. These coils are decoupled, the transmitting and receiving parts being not provided by the same electric circuit, and connected to a Tuning Matching circuit as described previously, see Fig. 29. The Transmitter generating the B_1 magnetic field, is provided by a solenoid coil of diameter $12mm$, and the Receiver part by a Saddle coil with a diameter of $16mm$. An electromagnet (Drusch $gap = 36mm, 860kg, 6mT - 2T$) allows the generation of the magnetic field B_0.

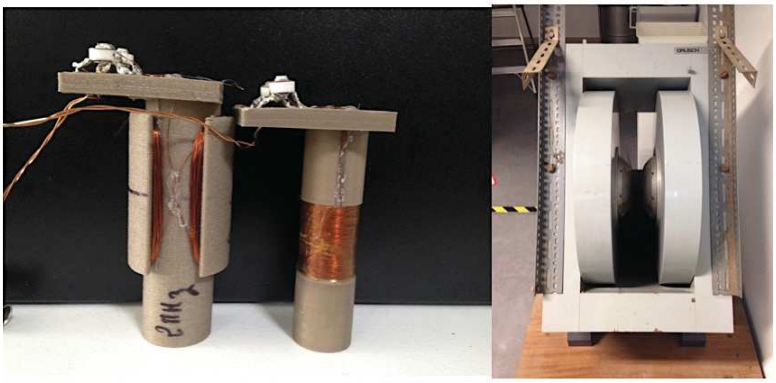

Figure 30 – NMR system used for the SNR study. On the left : an exemple of Transmitter coil (solenoid coil, $N_{turns} = 48$, which will be connected with a AMT RF amplifier) and Receiver coil (Saddle coil $N_{turns} = 30$ for each frequency) at $2MHz$ and on the right : an electromagnet.

The Fig. 31 shows the dependence of the SNR as a function of the frequency (Tuning-Matching curve) and as expected the SNR falls at $1MHz$ and a reasonable NMR experiments becomes too long with a conventional Transmitter/Receiver circuit (TxRx).

While at frequency above few MHz, it is convenient to use Tx power amplifier and Rx low noise Amplifier designed for input impedance of $50Ohm$, at lower frequency the design of the coil associated to the Tx and Rx amplifier should be reconsidered with the goal to optimize SNR.

Thus, the Rx amplifier designs conducted in the low field NMR investigations [Asfour, 2011] report the use of high impedance low noise amplifiers that would be better suited to the nature of the impedance on reception while the Tx amplifier can be oriented towards a very low impedance output to effectively excite the spins.

This configuration at low frequencies allowed us to gain a non-negligible factor in SNR

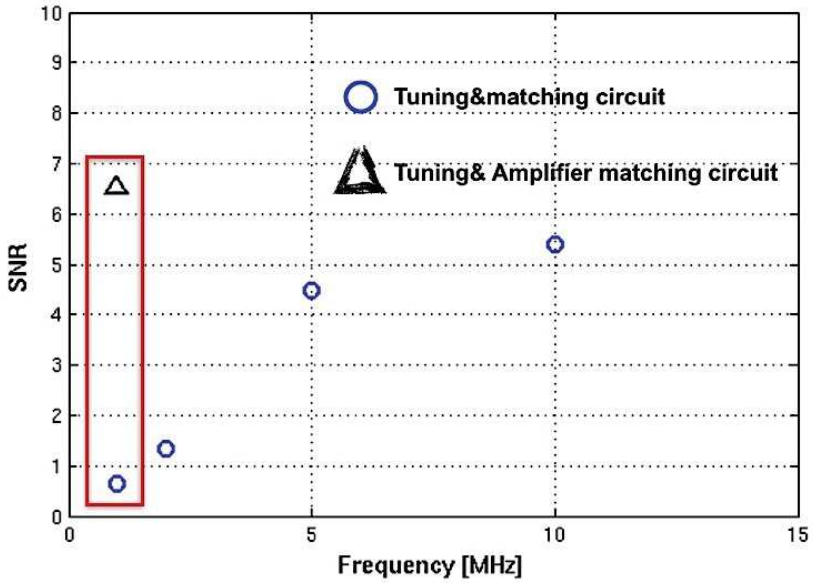

Figure 31 – SNR study as a function of Larmor Frequency. NMR signal obtained with water reference. NMR signal measured with CPMG sequence under NTNMR pulse sequencer with the same parameters (acquisition time about 30mn for each frequency).

showed in the Fig. 32. This gain in SNR by optimizing the detection chain opens a new way to work at low magnetic field.

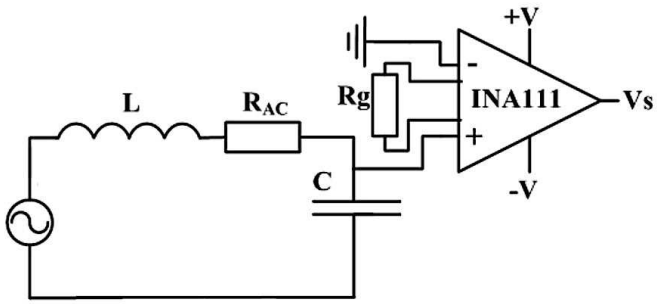

Figure 32 – Illustration of the RLC coil with Tuning and Matching amplifier circuit which matches the natural high impedance of the coil at low frequency.

Concerning TxRx coil configuration best suited for our agronomic studies, it is required, in addition to the usual qualities expected from a NMR coil probe (optimized filling factor, homogenous RF field) a convenient configuration of coils for keeping intact the plants. Obviously, the configuration of a Solenoid as Transmitter and a Saddle as Receiver used in the SNR study is not suitable for agronomic studies.

To keep the plant intact we have designed an original configuration of TxRx that consists

of clipping coils. This feature is essential in order to allow a TxRx placement while keeping the plant intact. Our prototype of clipping coil consists of two identical Saddles with a same geometrical parameters.

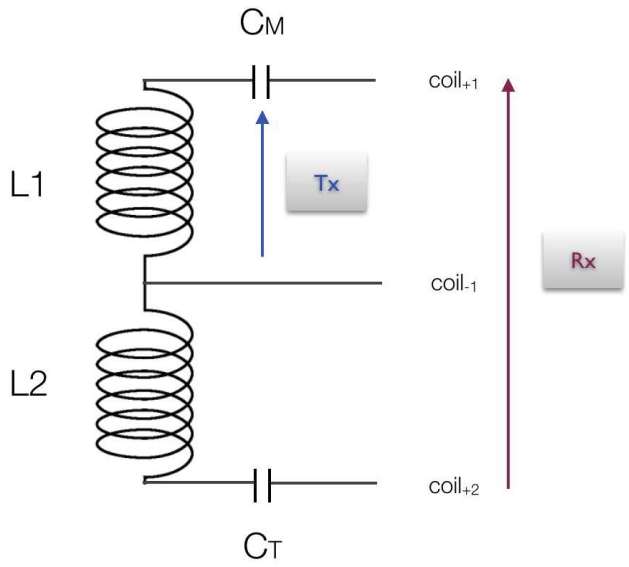

Figure 33 – Sketch of the TxRx clipping coil configuration

In our TxRx coils prototype presented in Fig. 33 : one Saddle is used as Transmitter (with an inductance L_1) which must be able to generate an efficiently field. Thus, we use a coil Tx far from its resonance and which approximates by $R_{ac}+jL\omega$, it is associated with a matching capacity element (C_M) that will compensate the imaginary part, the equivalent impedance then becomes : $Z = R_{ac}$. Since the impedance is weak, we will more easily generate current in the coil and thus the field B_1.

Then, the coil Rx (with an inductance L_1+L_2) must have its "natural " resonance closest to the gyromagnetic resonance (in practice , it would be justified by the study of the quality factor according to the capacity C_T in parallel).

Finally, the coupling caused by a superposition of coils is problematic, to remedy this, an active decoupling solution is assured by a switch in both modes Tx and Rx. By using switches, it must be ensured that there is no effect that degrades the SNR excitation. To do this, we found that when it was inserted between the tuning capacity and the coil, its contribution to the noise becomes considerable (because its resistance in the conducting state was added to that of the coil). Whereas when it was placed after the tuning capacity its contribution to the noise becomes reduced (in the passing state, the resistance of the switch used is of $20Ohm$, its contribution to thermal noise will therefore be neglected in noise modeling).

For our mobile NMR we took part to work at $336KHz(8mT)$. Thus, the first TxRx

clipping coil actively decoupled was developed (number of turns for each Saddle $N_{turns} = 30$, a inductances $L_1 = L_2 = 130uH$, a heigh of coils $H_c = 50mm$ and the inside diameter of the coil D=$20mm$) and exhibits a satisfactory performances ($Q_{factor} = 40$) because we have reached the ultimate goal which is non invasiveness. The complete schematic of Tx and Rx amplifiers developed with electrical components references is presented in Annex 3.

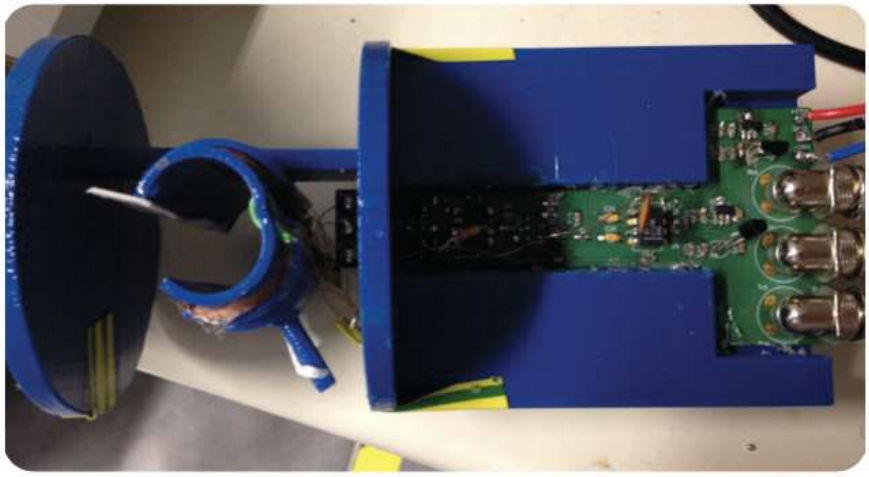

Figure 34 – Design and 3D printing of clipping antenna based on Saddle configuration at $336kHz$ to keep the integrity of plant. Transmitter coil is a Saddle : $N_{turns} = 30, L_1 = 130uH$, Receiver coil is a Saddle : $N_{turns} = 60, L_2 = 475uH$ and $D = 20mm$.

14 Design of portable and homogeneous resistive magnet

In this part we will describe the steps to develop a resistive magnet with the following constraints : a magnetic field of 8mT with a homogeneity of 1% in the area of interest, accessible with a minimum gap of 20mm and with overheating tolerance of about 6K to keep the plant intact.

14.1 Magnet based on Helmholtz coils

For our first low field NMR investigations, we will use a pair of commercially available Helmholtz coils (reference: $Teltron261 - 018$ with gap about $50mm$, $N_{turns} = 320$ and $D = 138mm$), see Fig. 36. This magnet is able to generate a maximum uniform magnetic field of $10mT$. Indeed, the study of the magnetic field profile revealed to us that the inhomogeneity of this prototype is estimated to be more than 2 %.

From a practical point of view, it is imperative to improve the homogeneity of the magnetic field. It is therefore necessary to act on the homogeneity of the magnet by "shimming" with additional coils. In fact, magnetic field inhomogeneities can be reduced using shimming

coils, that make the magnetic field uniform in the measurement area. These coils minimize the magnetic field inhomogeneities by superimposing a magnetic field with the same spatial distribution and magnitude but with opposite sign to inhomogeneities.

14.1.1 Design of shimming coils

The design of the shimming coils is very delicate. Moreover, about this [Romeo and Hoult, 1984] said: " there is no substitute for the experience in the design of coils and shim" systems. Nevertheless these pioneers have proposed a mathematical approach that allows modeling the contribution of free sources of current density, J, in region of space to create a magnetic field B governed by the Maxwell equations.

Thus and with considering only the z component, we can describe the magnetic field vector by spherical harmonic functions in spherical coordinates (r, θ, ϕ) as [Hudson, 2011] :

$$B_z(r) = \Sigma_{n=0}^{\infty} \Sigma_{m=-n}^{n} C_n^m r^n P_n^m(cos\theta) e^{(im\phi)} \tag{49}$$

where P_n^m are Legendre polynomials with positive integer order n and positive integer degree m. C_n^m is the amount of the n^{th} order, m^{th} degree spherical harmonic present in $Bz(r)$.

So, the shimming of the magnet involves the introduction of coils that can be positioned in such a way to compensate for unwanted terms in the spherical harmonic basis. The next Fig. 35 shows, in a Cartesian and spherical reference frame, the basis functions that are commonly encountered in NMR [Hudson, 2011].

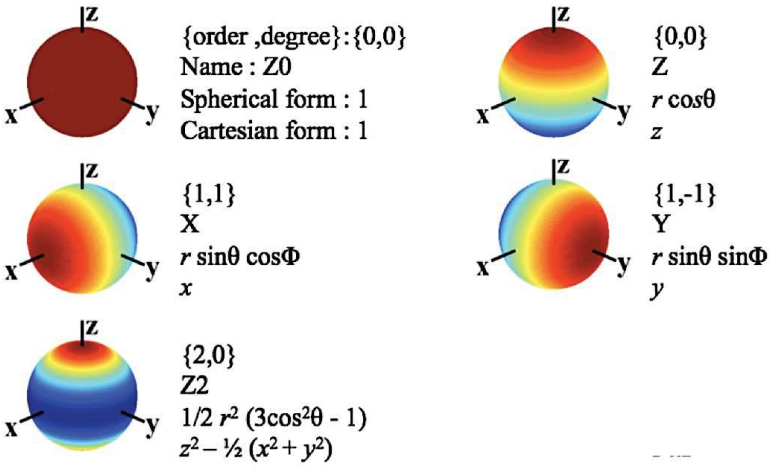

Figure 35 – Plots of the most spherical harmonics on the surface of a sphere. The equations for the spherical harmonics are given in spherical (r, θ, ϕ) and Cartesian (x, y, z) coordinates extracted from [Hudson, 2011].

In our case, shimming coils are resistive coils of wire carrying currents controlled by the

user to minimize the field inhomogeneities. Four sets of gradient coils were manufactured for our NMR device : the x, y, z and z^2 gradients (which their compensation are respectively represented by the spheres $x\{1,1\}, y\{1,-1\}$, $z\{0,0\}$ and $z^2\{2,0\}$ in the Fig. 35). Each coil set (of radius R) is driven by an independent power amplifier and creates a gradient magnetic field whose z component varies linearly along the x, y, z and z^2directions, respectively .

According to [Romeo and Hoult, 1984], our design of the z gradients is based on circular planar Maxwell coils, the transverse (x and y) gradients typically on a planar Golay coil, while the z^2 gradient is based on a planar anti maxwell configuration. The size of the gradient coils and the intensity of the magnetic field gradient they are able to produce in order to compensate the inhomogeneities have been determined thanks to a numerical finite element software tool (see Fig. 36) and are given in Table. 3.

Coils types	According gradient	N_{turns}	R	Field compensation
Maxwell	G_z	30	$40mm$	$67\mu T(1\%)$
Golay	G_x, G_y	28	$50mm$	$67\mu T(1\%)$
Anti Maxwell	G_z^2	30	$40mm$	$67\mu T(1\%)$

Table 3 – Summary of the geometric informations and the field produced by the gradients which makes it possible to compensate 1% of inhomogeneities associated to the Helmholtz coil according to the simulations achieved by a numerical finite element software.

Thus, we have developed and manufactured these gradients. The prototype shown in Fig. 36 represents the Helmholtz coils with their shimming coils. The homogeneity of the prototype is improved and estimated now to be less than 1% which is in good agreement with the simulation at $8mT$.

Despite the efforts , the homogeneity remains also a critical point in this prototype for NMR studies. The other disadvantage is that the shimming coils require a power supply which will complicate the transport to the fields. Finally, the overheating of the magnets was very unfavorable (about 30K). All these reasons pushed us to find another approach to build a magnet with respect to our constraints. The SHS method, described in [Coillot, 2016b], initially intended for the design of the RF coil, seems a good track that will be investigated in the next part to develop the magnet.

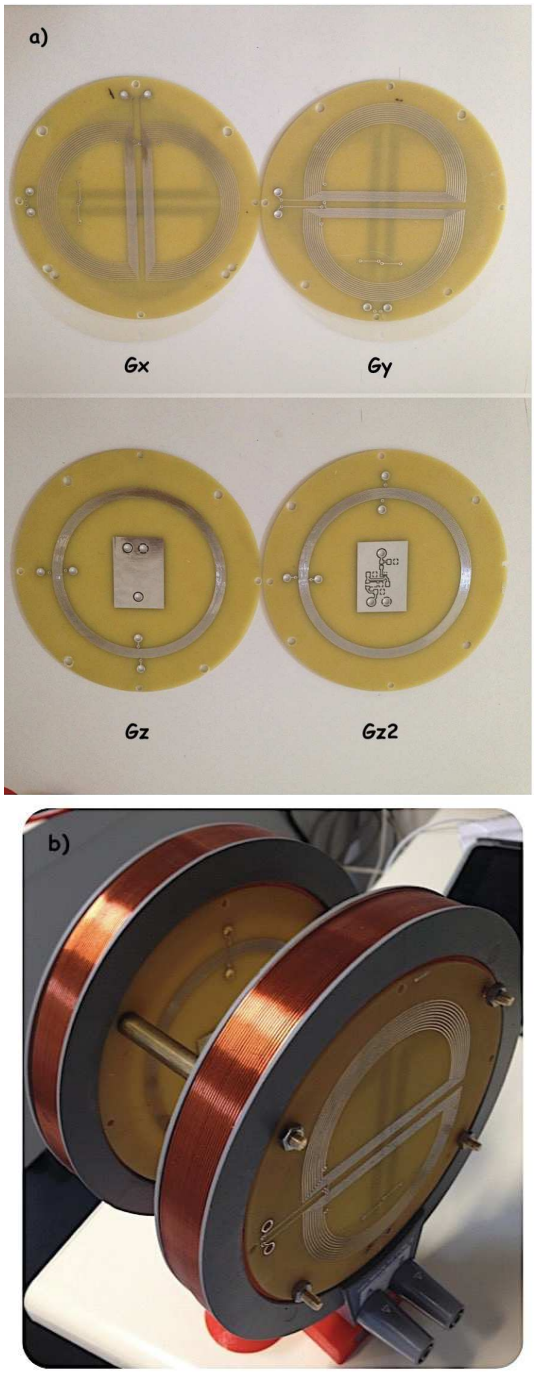

Figure 36 – a) Photography of the x, y, z and z^2 gradients dedicated to Helmholtz coil prototype and b) Portable Magnet prototype based on the Helmholtz model at $336kHz$ ($I = 2A$, $R = 69mm$, $N_{turns} = 320$, window of wire winding : $18mm \times 15layers$, $r_c = 0.4mm$, and the prototype total weight about $3Kg$)

14.2 Magnet based on Space Harmonic Suppression method

14.2.1 Space Harmonic Suppression method

It is a well known fact that a cosine current repartition in infinite cylindrical or spherical shells allows to approach perfect magnetic field homogeneity [Clarck, 1938], [Hayes, 1985] and [Bolinger, 1988]. For coils of revolution with axisymmetric geometry, the homogeneous

condition is reached when the magnitude of the current density J_{e_ϕ}, oriented in e_ϕ direction (Fig. 37.a), is cosinusoidal (along the virtual circle represented with the dashed line). This configuration of the spherical coil was first (to our best knowledge) proposed to improve the homogeneity of the Helmholtz coil for nuclear research [Clarck, 1938].

$$J_{e_\phi}(\theta) = J_0 cos(\theta) e_\phi \tag{50}$$

Similarly, in the case of an infinite extruded plane geometry the homogeneous condition is reached when the magnitude of the current density distribution J_z, oriented in z direction (Fig. 37.b), is cosinusoidal along the circumference of the virtual circle represented with dashed line.

$$J_z(\theta) = J_0 cos(\theta) z \tag{51}$$

Where, in both cases, J_0 is the current density magnitude and θ is the angular position over a circle of radius R.

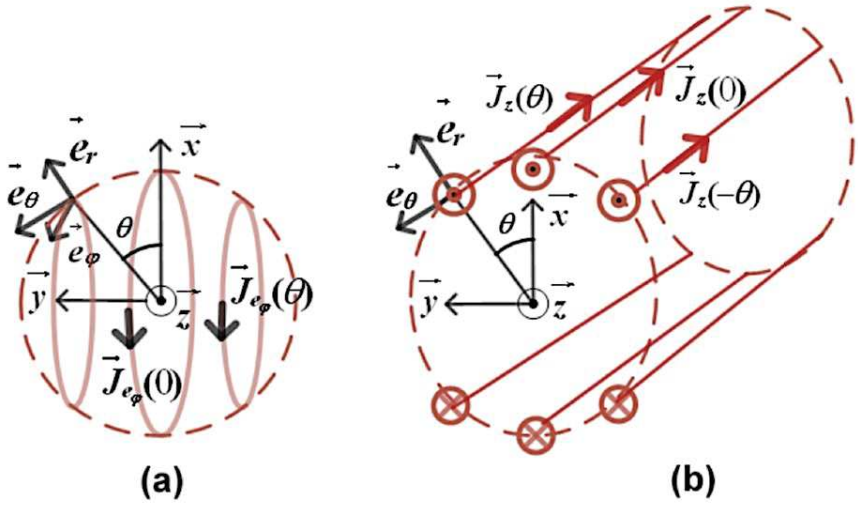

Figure 37 – Illustration of current density distribution for two configurations : (a) axisymmetric geometry in spherical coordinates, (b) plane geometry (infinite in z direction) in cylindrical coordinates.

In the case of the cylindrical geometry [Clarck, 1938] and [Everett, 1966], for a plane geometry, [Bolinger, 1988] suggested to approach the ideal sphere coil by placing N equally spaced turns (on the diameter projection) separated by a distance b, each turn being flown by the same current while the position of the n_{th} turn on the y axis is given by: $y(n_{th}) = n_{th}b + R/N$ (as illustrated by Fig. 38).

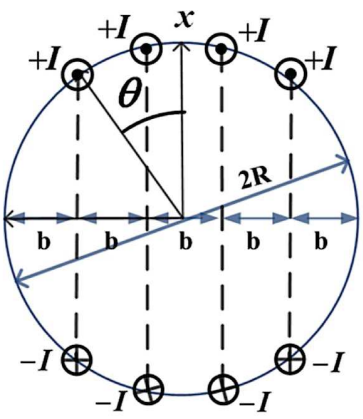

Figure 38 – Illustration of the sphere coil distribution according to [Bolinger, 1988] : the coils are placed along the circumference of the cylinder at angles θ and equally spaced by a distance $b = 2R/(2N + 1)$

Bolinger, drew a parallel with the cosine spatio-temporal distribution exploited in Birdcage coils [Hayes, 1985] and proposed to implement Clark's rule of spatial distribution of conductors in the context of RF MRI coils with a cylindrical geometry. Thus, the homogeneity on the obtained images proved insufficient to pretend to replace the Birdcage coils (very used in MRI). One of the possible reasons for this disillusionment was that the rule enunciated by Clark implied an infinite or, at least, high number of wire.

Thus, the problem of how to distribute the electrical conductors, flowed by the same current, along the circumference to obtain a homogeneous magnetic field inside the coil has been re examined through an analytic method based on a Space Harmonic Suppression (SHS) to determine the spatiale wire distribution [Coillot, 2016b].

The SHS method consists in approximating the cosine current density distribution by calculating discrete conductors angular positioning on a circle with a radius R (see Fig. 39), aiming to approach cosine distribution by means of a Fourier series formalism. It was assumed, in this work dedicated to MRI probe, that the same current was flowing in each conductor.

Thus, we will consider a current density distribution in coils (the authors use a Dirac representation): the current magnitude is the same (illustrated by Fig. 40). Then, the current density distribution will be expressed as :

$$J(\theta) = I(\delta(\theta) - \delta(\theta - \pi)) + \Sigma_{n=1}^{N} I(\delta(\theta - \theta_n) + \delta(\theta + \theta_n) - \delta(\theta - \theta_n - \pi) - \delta(\theta + \theta_n - \pi)) \quad (52)$$

The current density distribution is an even function, and the terms $\delta(\theta)$ and $\delta(\theta - \pi)$ are related to the central coil. For portable NMR, the magnet must be "accessible", so we consider only the configuration of the coils without central conductor ($x = 0$). Then, the Fourier series coefficient (a_{2k-1}) of $J(\theta)$ can be calculated.

$$a_{2k-1} = \frac{4I}{\pi}\Sigma_{n=1}^{N} cos((2k-1)\theta_n) \tag{53}$$

The current density function $J(\theta)$ is then written as a Fourier series :

$$J(\theta) = \Sigma_{k=1}^{\infty}\left(\Sigma_{n=1}^{N}\frac{4I}{\pi}cos((2k-1)\theta_n)\right)cos((2k-1)\theta) \tag{54}$$

Where the Fourier series decomposition has an infinite number of harmonics. Each harmonic (represented by means of a Dirac distribution, see Fig. 40) can be cancelled by means of a supplementary conductor.

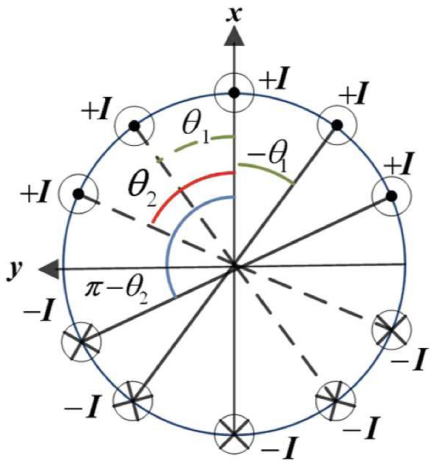

Figure 39 – Illustration of electrical conductors of unknown angular positions (θ), flown by the same current I, distributed along the circumference.

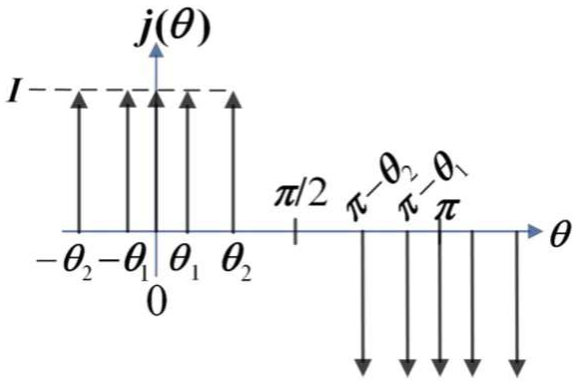

Figure 40 – Illustration of the space current density distribution : Dirac representation

14.2.2 Study of magnetic field homogeneity of SHS coils

In this part, we will apply the SHS method on different cases where we can have one, two, and three pairs of coils, $(N = 1), (N = 2)$ and $(N = 3)$ respectively, to analyze the homogeneity

performance provided by the SHS method using magnetostatic modeling by finite element. The different SHS solutions will be compared to Helmholtz coil and each other.

From Eq. (54) the angle solutions which have been obtained for the two, four and six pairs of coils are mentioned here:

- For the SHS 2 model, the condition to remove the current density space harmonics is :

$$cos(3\theta_1) = 0 \tag{55}$$

  The angle solution which have been obtained for SHS 2 is $\theta_1 = 30°$

- For the SHS 4 model, the conditions to remove the current density space harmonics are :

$$\begin{aligned} cos(3\theta_1) + cos(3\theta_2) &= 0 \\ cos(5\theta_1) + cos(5\theta_2) &= 0 \end{aligned} \tag{56}$$

  The angle solutions obtained for SHS 4 are : $\theta_1 = 12°$ and $\theta_2 = 48°$

- For the SHS 6 model, the conditions to remove the current density space harmonics are :

$$cos(3\theta_1) + cos(3\theta_2) + cos(3\theta_3) = 0$$

$$cos(5\theta_1) + cos(5\theta_2) + cos(5\theta_3) = 0$$

$$cos(7\theta_1) + cos(7\theta_2) + cos(7\theta_3) = 0$$

  The angle solutions obtained for SHS 6 are : $\theta_1 = 11.56°$, $\theta_2 = 26°$ and $\theta_3 = 56°$

The homogeneity efficiency criteria used to evaluate the different performances of the SHS coil are : the 0.1, 1 and 10 % homogeneities are defined as the fraction of the coil diameter $(\Delta(B_y)/(2R)$, where $\Delta(B_y)$ is the distance from center O along y (see Fig. 41) where the magnetic field intensity remains, respectively, within 0.1, 1 and 10 % of its maximum value where the variation of B with respect to its value at the center. The results are as presented in Table .4.

The Fig. 41 shows that an homogeneity distribution obtained by simulation using SHS method in a region of interest of R=10mm, sufficient to perform quantitative NMR experiments and relaxometry (hundred of ppm) in a wide volume fraction of the coil can be reached.

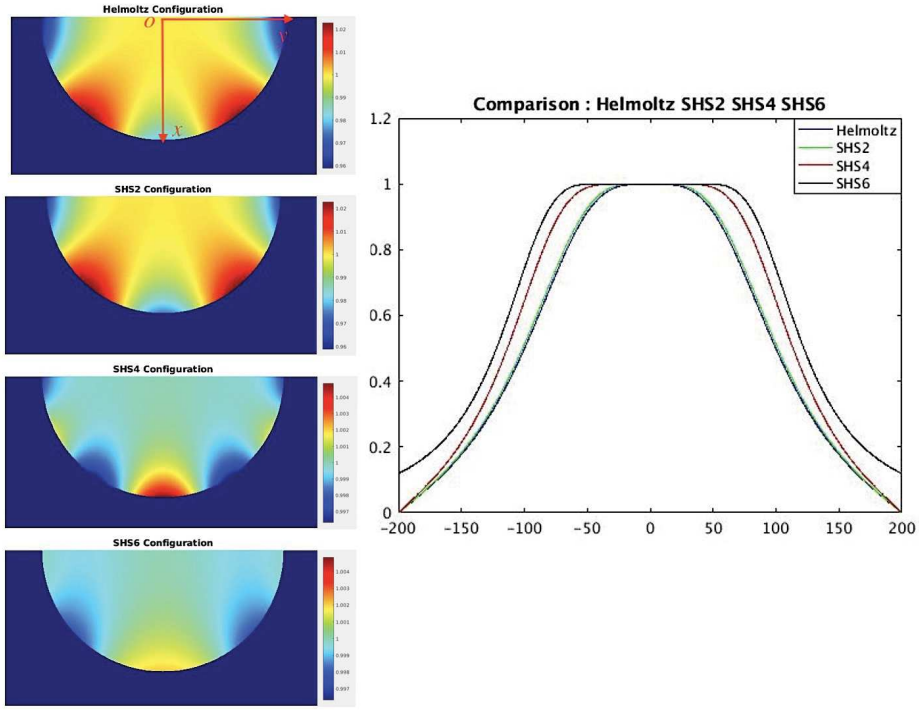

Figure 41 – Comparison of the homogeneity of the Helmholtz coil, SHS 2, SHS 4 and SHS 6 respectively. a) 2D Magnetic field homogeneity distribution b) Magnetic field homogeneity profile on the y axis.

	Helmoltz	SHS 2	SHS 4	SHS 6
0.1% homogeneity	0.141	0.199	0.355	0.523
1% homogeneity	0.267	0.301	0.493	0.629
10% homogeneity	0.523	0.543	0.729	0.837

Table 4 – Axisymmetric coil homogeneity study: comparison between several coils configurations: Helmholtz, SHS 2, SHS 4 and SHS 6

14.2.3 SHS 4 magnet design

The manufacturing of the SHS 4 based on parameters given in the previous section seems to offer a promising compromise between : the accessibility (gap between the inner coil is about $20mm$) and an overheating (about $21K$) around the sample under test. But, this overheating is still too stringent for agronomics studies, see Fig. 42. However, the homogeneity of the prototype is improved at $8mT$ compare to Helmholtz coil (less than 1%). Note that, all the coils of the prototype have the same number of turns equal to 320 turns.

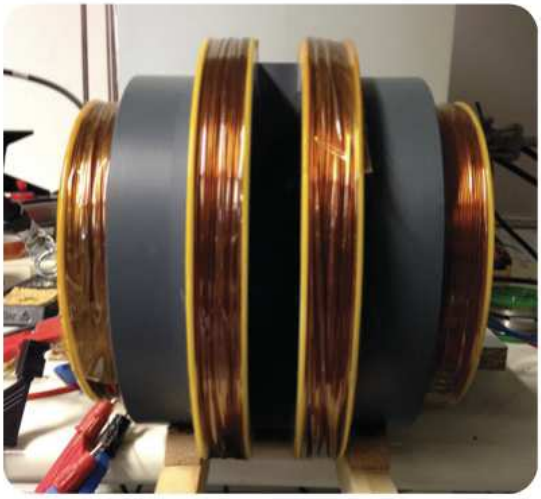

Figure 42 – Portable Magnet prototype based on the SHS 4 model at $8mT$ ($I = 1.4A$, $R = 100mm$, $N_{turns} = 320$, window of wire winding: $18mm \times 15layers$, $r_c = 0.4mm$, and the prototype total $weight = 6Kg$).

The validated design on the SHS 4 prototype results has encouraged us to go further in the prototype construction. The thermal behavior will be studied with a special focus on the inner coil, which is the closest to the plant stem where the self-heating must be limited.

14.3 Dissipation of overheating of SHS coil

14.3.1 Thermal dissipation issue

In the fondamental thermodynamics, the notion of thermal transfer is one of the modes of thermal energy exchange between two systems with different Temperature (T). There are three types of thermal dissipation : conduction, radiation and convection [Incorpera, 1990].

- The conduction (or diffusion) is a mode of thermal transport without macroscopic displacement of matter. This transfer takes place from the hot area to the cold area due to the thermal agitation. In the case of a flat wall with temperatures T_1 and T_2 imposed on the extremities of wall, a thickness e_t and a thermal conductivity $\lambda_S(W/m/K)$, the temperature distribution is linear. Then, the density of the flux at any point can be modeled by :

$$\varphi_t = \lambda_S \frac{T_1 - T_2}{e_t} \tag{57}$$

If $T_1 > T_2$, the flow Φ_t passing through a surface S is therefore :

$$\Phi_t = \lambda_S \frac{T_1 - T_2}{e_t} S \tag{58}$$

This phenomenon makes it possible to determine the thermal resistance of conduction R_{cond} (with : $T_1 - T_2 = R_{cond}\Phi_t$) of the materials to the passage of a thermal conduction flow for a flat infinite surface (S):

$$R_{cond} = \frac{e_t}{\lambda_S S} \tag{59}$$

- Radiation describes the transport of energy via electromagnetic wave propagation. As for conduction, it is the interaction between atoms and molecules which is at the origin of this radiation. Note that, this energy transfer is always present even in a vacuum. The power radiated by a surface can be calculated according to the Stefan-Boltzmann law:

$$PHI_{rad} = \sigma S \epsilon (T_s^4 - T_\infty^4) \tag{60}$$

Where T_s is average surface temperature, σ is the Stefan-Boltzmann constant ($5.6703e^{-8} W m^{-2} K^{-4}$), ϵ is the emissivity of the surface of material (coefficient between 0 and 1 which is the unit for a black body) and T_∞ is the ambient temperature.

- Convection is a mode of thermal transfer that involves a collective displacement of fluid. The hot fluid material, while moving, gives energy to the colder parts. There are two types of convection : the first one called "artificial convection" which requires a mechanical device (too restrictive for portable NMR) and the second on is called "natural convection" which stipulates to increase the exchange surface to dissipate naturally the heat. In convection, the power emitted by a surface can be calculated according to :

$$PHI_{conv} = h_s S (T_s - T_\infty) \tag{61}$$

Where h_s represents the exchange coefficient between the wall and fluid in ($W.m^{-2}.K^{-1}$)

14.3.2 Power to be dissipated by SHS coils

In our case, the conductive resistance will be neglected (the coil being constituted of highly thermal conductive material) and the power to be dissipated (P_n) by the n^{th} coil will be evacuated by means of natural convection and radiation through the exchange area of the coil (S_n):

Using Eq. (60) and Eq. (61), the total power of SHS coil can be calculated :

$$P_n = PHI_{conv} + PHI_{rad} = h_s S_n (T_s - T_\infty) + \sigma \epsilon S_n (T_s^4 - T_\infty^4) \tag{62}$$

On the other side, the power dissipated by Joule's effect for the coil with resistance Res_n can be expressed :

$$P_n = Res_n I_n^2 \tag{63}$$

For the n^{th} coil , see Fig. 43, the resistance is expressed :

$$Res_n = 2\rho \frac{N_{turns} \times R \times cos(\theta_n)}{r_c^2} \tag{64}$$

where ρ is the material resistivity, r_c is the wire radius and N_{turns} the number of turns of the considered n^{th} coil.

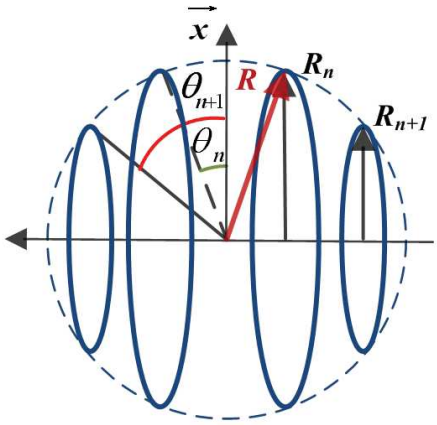

Figure 43 – SHS coil constituted of N pairs of coils.

14.3.3 Design of magnet based on SHS 4 with thermal dissipation

As depicted before the SHS 4 coil could suffer of too much overheating. For this we have established a thermal model where the natural convection coefficient h is preliminary determined by fitting the thermal prediction given by Eq. (62) with thermal measurement on a SHS 4 prototype (whose geometrical parameters are summarized on Table. (5), supplied with $I = 1.4A$ (in order to produce $8mT$). Then we determine the exchange surface needed to limit the overheating. Consequently the measured temperature of the coil overheating: $\triangle T < 25K$ and $T_\infty = 297K$, leads to estimate $h_s = 6Wm^{-2}K^{-1}$, that will allow us to calculate the exchange surface needed to solve the problem of overheating.

Thus, in order to solve this issue of the SHS 4 prototype, we increased the exchange area ($S = 0.24m^2$) and change the type of material support to reduce the temperature. Our goal is to evacuate heat by the natural convection mechanism, so we created a simple heat sink placed around the element to be cooled (coils). To make it, we choose a non-magnetic Aliminium

with a high thermal conductivity and we used black paint to get the emissivity coefficient as closest as possible to 1.

N_{turns}	$S_1(m^2)$	$r_c(mm)$	θ_1	$Res_1(\Omega)$
320	0.24	0.0489	0.2094	6.65

Table 5 – Geometric parameters of SHS 4 (supplied with $I = 1.4A$)

The improved setup (see Fig. 44) exhibits an overheating of about $\triangle T \simeq 12K$ which not satisfies completely the plant integrity. The linewidth of the NMR signal was used to estimate the homogeneity of the prototype about $300ppm$ in a volume of $1cm^3$ at $8mT$ demonstrating clearly the homogeneity performance.
Our prototype allowed us to measure with a One pulse NMR sequence (Acquisition time $< 3mn$ with a Repetition time about $1s$) the signal at stem of sorghum plant directly in the greenhouse.

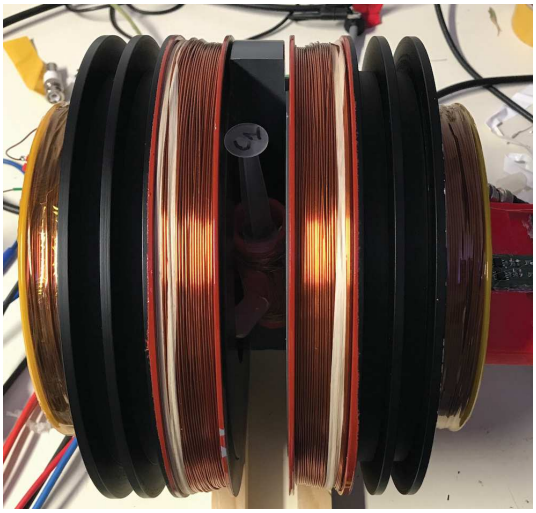

Figure 44 – Portable NMR prototype based on SHS 4 model at $336kHz$ for agronomics studies

The splitting of SHS coils into multiple coils has an important advantage compared to Helmholtz coil, with respect to the thermal behavior, since it allows us to split the total power on multiple coils (or, in other words, to increase the exchange area of coils). The study of the thermal behavior of the SHS coils with a special focus on the inner coil allowed us to predict the overheating of the SHS 4 and act accordingly.

The method presented took into account an equal current in each coil. This restriction is convenient for some NMR coils where the conductors are in series, but, not necessary for portable NMR. This prompted us to propose an Extended version where the current becomes a supplementary variable of the SHS problem.

14.4 Magnet based on Extended Space Harmonic Suppression method

14.4.1 Current density distribution

Thus, we will consider a more general current density distribution of the coil where the current magnitude in each coils are independant as depicted by Fig. 45. Then, by extending the method, the current density distribution (illustrated by Fig. 46) will be expressed:

$$J(\theta) = I_0(\delta(\theta) - \delta(\theta - \pi)) + \Sigma_{n=1}^{N} I_n(\delta(\theta - \theta_n) + \delta(\theta + \theta_n) - \delta(\theta - \theta_n - \pi) - \delta(\theta + \theta_n - \pi)) \quad (65)$$

where $\delta(\theta)$ is the one-dimensionnal Dirac distribution as a function of the angle θ and I_n is the product of current by the number of turns. Then, by applying a reasoning analog to the one developed in [Coillot, 2016a], the Fourier series coefficient (a_{2k-1}) of $j(\theta)$ can be calculated. The current density function $j(\theta)$ can then be re-written as a Fourier serie:

$$J(\theta) = \Sigma_{k=1}^{\infty} \left(\Sigma_{n=1}^{N} \frac{2}{\pi} (I_0 + 2I_n cos((2k-1)\theta_n)) \right) \times cos((2k-1)\theta) \quad (66)$$

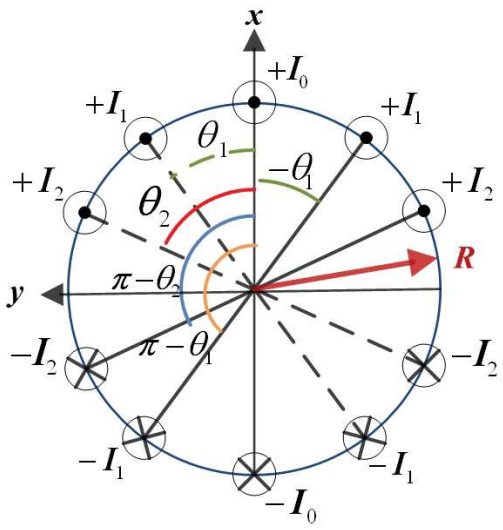

Figure 45 – Electrical conductors of unknown angular positions (θ_n), flown by currents I_n, distributed along the circumference.

14.4.2 Magnetic field generation

The magnetic field produced for the *in planta* portable NMR experiments requires to place the plant in the center of the coil. That leads us to focus only on the even SHS coils case (*i.e.* without central coils thus the term I_0 vanishes) composed of N pairs of coils. The magnetic field generated at the center of the SHS coil pair (B_n), based on the magnetic field at the center of a symmetric pair of coils, can be expressed either as a function of the coil radius

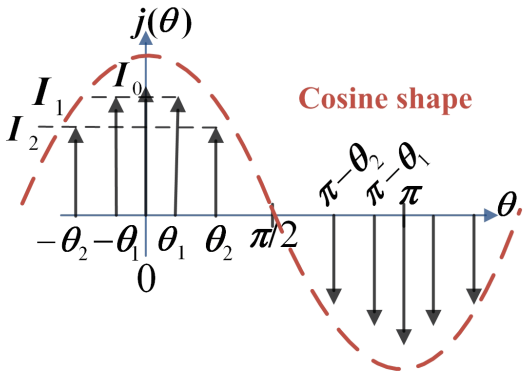

Figure 46 – Illustration of the space current density distribution for non identical currents flowing through the coils

(R_n), see Eq. (67), or as a function of the radius supporting circle (R such as $R_n = R\cos(\theta_n)$, defined on Fig. 49, see Eq. (68).

$$B_n = \frac{\mu_0}{R_n} N_n I_n cos^3(\theta_n) \tag{67}$$

$$B_n = \frac{\mu_0}{R} N_n I_n cos^2(\theta_n) \tag{68}$$

The total magnetic field (B_{SHS}) produced by the N pairs of coils results from the sum of the magnetic fields produced by each pair of coils:

$$B_{SHS} = \frac{\mu_0}{R} \Sigma_{n=1}^{N} N_n I_n cos^2(\theta_n) \tag{69}$$

14.4.3 Formulation of the homogeneous magnetic field coil design problem

In the context of a N turns coil pairs without the central coil, we will have to determine the N angles and currents allowing to produce the target magnetic field ($B_{SHS} = 8mT$ in our design case) and satisfying the harmonic suppression. That gives us $2N$ equations allowing to suppress $(2N-1)$ harmonics. The first equation of the equation set (Eq. (70)) allows the respect of the magnetic field goal (namely Eq. (69)) while the other equations are deduced from harmonics suppression (Eq. (66)):

$$\begin{gathered}
\frac{\mu_0}{R}\Sigma_{n=1}^{N} N_n I_n cos^2(\theta_n) = B_{SHS} \\
... \\
\Sigma_{n=1}^{N} I_n cos(3\theta_n) = 0 \ \& \ (k=2) \\
... \\
\Sigma_{n=1}^{N} I_n cos((2j-1)\theta_n) = 0 \ \& \ (k=j) \\
... \\
\Sigma_{n=1}^{N} I_n cos((2N-1)\theta_n) = 0 \ \& \ (k=2N)
\end{gathered} \tag{70}$$

The set of equations offers the possibility to design the coil generating the required magnetic field and allowing to enhance the homogeneity by means of the harmonics suppression.

14.4.4 Numerical resolution aspects

The angles solution of Eq. (70) are obtained using a numerical resolution tool. Nevertheless, for a large number of variables the algorithm may converge to aberrant solution with some angles higher than $\pi/2$ which satisfies the harmonic cancellation but does not maximize the magnetic field. Thus, it is recommended, in such case, to solve the design problem using optimization formalism. The objective function will be written as compromise between the maximization of the magnetic field production $g_{max}(u)$ (left member of first equation of Eq. (70) and the minimization of function $f_{min}(u)$ ensuring the cancellation of the harmonics (remaining equations of Eq. (70)):

$$g_{max}(u) = \left(\frac{\mu_0}{R}\Sigma_{n=1}^{N} N_n I_n cos^2(\theta_n)\right)^2 \tag{71}$$

$$f_{min}(u) = \left(\Sigma_{n=1}^{N} I_n cos(3\theta_n)\right)^2 + ...$$

$$+ \left(\Sigma_{n=1}^{N} I_n cos((2N-1)\theta_n)\right)^2$$

where u is the set of variables (θ_n and I_n).

Next, the optimization formalism will permit to limit the feasible space solution research using inequality constraints. Thus, an example of optimization formalism for the SHS coil design will be:

$$Min_{(u)}\ [\frac{\alpha_s}{g_{max}(u)} + \beta_s f_{min}(u)]$$

$$0 <\ \theta_n < \pi/2$$

$$I_n > 0$$

where α_s and β_s are the compromise parameters which should be determined intuitively by the designer. Lastly, the angles solution of the optimization problem are obtained using a numerical optimization tool.

To conclude this section, we report the angles solution (expressed in radian) and homogeneity efficiency (see Table. (9))obtained for SHS 8 and SHS 10 (with identical currents I_n) by means of the optimization formalism of Eq. (72):

- SHS 8 ($\theta_1 = 0$, $\theta_2 = 0.439$, $\theta_3 = 0.609$ and $\theta_4 = 1.061$).
- SHS 10 ($\theta_1 = 0.163$, $\theta_2 = 0.264$, $\theta_3 = 0.573$, $\theta_4 = 0.7901$ and $\theta_5 = 1.159$).

	SHS 6	SHS 8	SHS 10
0.1% homogeneity	0.523	0.5276	0.6078
1% homogeneity	0.629	0.6563	0.7144
10% homogeneity	0.837	0.884	0.893

Table 6 – Axisymmetric coil homogeneity study: comparison between several coils configurations: SHS 6, SHS 8 and SHS 10

The optimization formalism opens the way to a flexible solution where other kinds of constraints can be implemented (given range of values for instance).

14.4.5 Study of magnetic field homogeneity of Extended SHS coils

In this part, we consider the case of two pairs of turns ($i.e., N = 2$) and ($N = 3$) respectively. From Eq. (70) , the angle and current solutions which have been obtained for the four and six pairs of coils are mentioned here:

- For the Extended SHS 4 model (we have four variables: two angles and two currents), the condition to remove the current density space harmonics is :

$$\frac{N\mu_0}{R}\left(I_1 cos^2(\theta_1) I_2 cos^2(\theta_2)\right) = 8mT$$

$$\begin{aligned} I_1 cos^2(3\theta_1) I_2 cos^2(3\theta_2) &= 0 \\ I_1 cos^2(5\theta_1) I_2 cos^2(5\theta_2) &= 0 \\ I_1 cos^2(7\theta_1) I_2 cos^2(7\theta_2) &= 0 \end{aligned} \tag{72}$$

The solution of this set of equations is obtained by means of a numerical minimization and leads to $\theta_1 = 0.3142$, $\theta_2 = 0.9425$, $I_1 = 1.7794A$ and $I2 = 1.0997A$. Finally, we report in Table. 7 the study of homogeneity at the 0.1, 1 and 10 % using simulations achieved by finite element tool.

	SHS 4	Extended SHS 4
0.1% homogeneity	0.355	0.393
1% homogeneity	0.493	0.573
10% homogeneity	0.729	0.806

Table 7 – Axisymmetric coil homogeneity study: comparison between normal SHS 4 and Extended SHS 4

- For the Extended SHS 6 model (we have six variables: three angles and three currents), the condition to remove the current density space harmonics is :

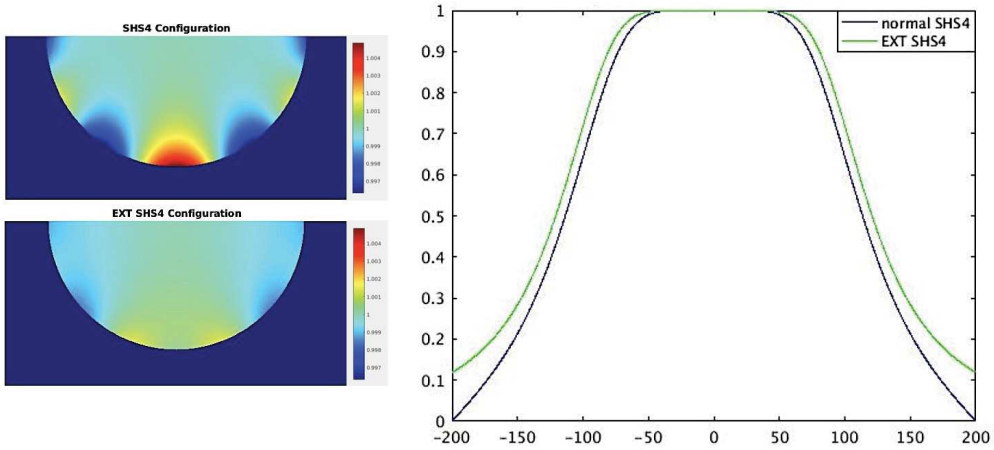

Figure 47 – Comparison of the homogeneity of the Helmholtz coil SHS 4 and Extended SHS 4 respectively. a) 2D Magnetic field homogeneity distribution b) Magnetic field homogeneity profile on the y axis.

$$\frac{N\mu_0}{R}\left(I_1 cos^2(\theta_1) I_2 cos^2(\theta_2)_2 I_3 cos^2(\theta_3)\right) = 8mT$$

$$\begin{aligned}
I_1 cos^2(3\theta_1) I_2 cos^2(3\theta_2) I_3 cos^2(3\theta_3) &= 0 \\
I_1 cos^2(5\theta_1) I_2 cos^2(5\theta_2) cos^2(5\theta_3) &= 0 \\
I_1 cos^2(7\theta_1) I_2 cos^2(7\theta_2) cos^2(7\theta_3) &= 0 \\
I_1 cos^2(9\theta_1) I_2 cos^2(9\theta_2) cos^2(9\theta_3) &= 0 \\
I_1 cos^2(11\theta_1) I_2 cos^2(11\theta_2) cos^2(11\theta_3) &= 0
\end{aligned} \tag{73}$$

The solution of this set of equations is obtained by means of a numerical minimization and leads to $\theta_1 = 0.2244$, $\theta_2 = 0.6732$, $\theta_3 = 1.122$ $I_1 = 1.305A$, $I_2 = 1.0465A$ and $I_3 = 0.5808A$.

The Fig. 47 suggests that the extended SHS method makes it possible to improve the homogeneity in the region where the NMR measurement was achieved.

14.4.6 Study of thermal behavior of Extended SHS 6

The Extended SHS 6 model allows , in addition to the improvement of the magnetic field homogeneity, to decrease the temperature compared to SHS 4. Dispatching in several coils , allows to distribute the power to dissipate while increasing the exchange surfaces. To evaluate the temperature of this model, we relied on the thermal model for the SHS method presented

before with a special focus on the inner coil.

N_{turns}	$S_1(m^2)$	$r_c(mm)$	θ_1	$Res_1(\Omega)$
320	0.24	0.0489	0.2244	6.65

Table 8 – Geometric parameters of Extended SHS 6 (supplied with $I = 1.3A$)

With the calculated parameters given in Table. 8, we predicted an overheating about $20K$. This result is still far from our goal that aims to keep the plant intact during NMR measurement. This time, the idea to increase the surface with the design of a heat sink is not the best due to the configuration / positioning of the coils. This thermal issue forced us to go further with this Extended SHS method. So we decided to fixe some parameters to reduce the overheating : this is accomplished by setting the current and position of the first coil pair.

14.5 Study of magnet based on Constrained Extended SHS 6 : fixed current and aperture angle θ_1.

In this part, we will constraint the formulation of the Extended SHS by fixing some parameters like the current intensity flowing into the inner coil ($1A$ should permit to limit the coil overheating: $\triangle T < 10K$.) and the angle of the central pair of coils (in order to have a sufficient gap to insert the plant stem, namely $\simeq 30mm$). Thus, we will fix $I_1 = 1A$ and $\theta_1 = 0.2244$, which reduces our number of variables to 4 and thus simplifies the set of Eq. (73). The solution obtained for the new set of equation is $\theta_1 = 0.2244$, $\theta_2 = 0.4509$, $\theta_3 = 0.9676$, $I_1 = 1A$, $I_2 = 0.8844A$ and $I_3 = 1.0017A$.

	SHS 6	Extended SHS 6	Constrained SHS 6
0.1% homogeneity	0.355	0.597	0.399
1% homogeneity	0.493	0.637	0.463
10% homogeneity	0.629	0.733	0.589

Table 9 – Homogeneity comparison between the SHS 6, the Extended SHS 6 and the constrained Extended SHS 6

The results in Table. 9 show that even by imposing constraints on this method, the homogeneity, remains favorable for NMR measurements. It is still possible to improve it with the increase in the number of pairs of SHS coils.

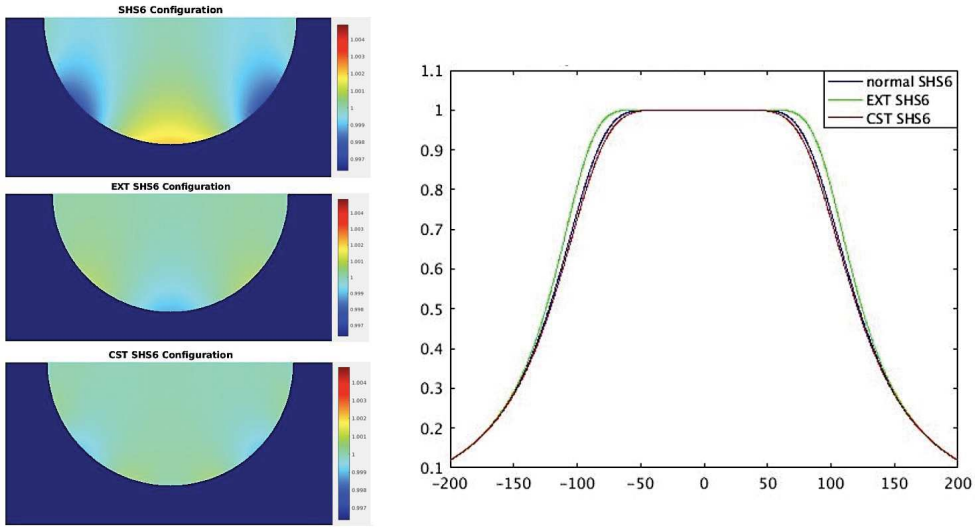

Figure 48 – Comparison of the homogeneity of the SHS 6, Extended SHS 6 and Constraint SHS 6 respectively. a) 2D Magnetic field homogeneity distribution b) Magnetic field homogeneity profile on the y axis.

15 Portable NMR device at 336kHz

The magnetic field produced for the *in planta* portable NMR experiments results in a compromise between the generation of homogenous magnetic field on one side and self-heating to avoid heating stress of the plant on the other side (it is assumed that local surrounding sorghum stem temperature increase should remain $< \Delta T(K) = 10K$). The use of SHS coils allows to seek for the best compromise thanks to the splitting of the dissipated power over several coils. Since, the application requires to access the center of the coil and it has lead us to consider a constrained design option. For these reasons we decided to manufacture the model of constraint SHS 6 (with the previous parameters) which allows to have a comfortable gap of 30mm and a reasonable overheating compliant with the plant physiology.

15.0.1 Manufacturing of Magnet based on Constrained SHS 6

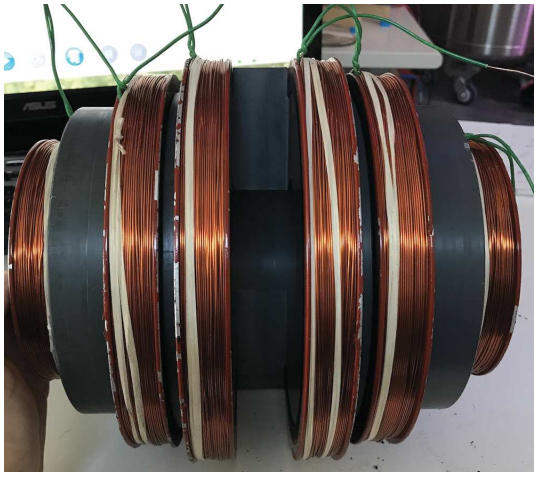

Figure 49 – Portable NMR prototype based on Constraint Extended SHS 6 model at $336kHz$ for agronomics studies

With this new prototype, the measured overheating around stem is now about $6K$ and totally compatible with our futur experiments.

15.0.2 Manufacturing of RF coil based on SHS 6

The promising results concerning the homogeneity of the SHS method also prompted us to use the SHS 6 model to manufacture the TxRx coil presented in Fig. 50.

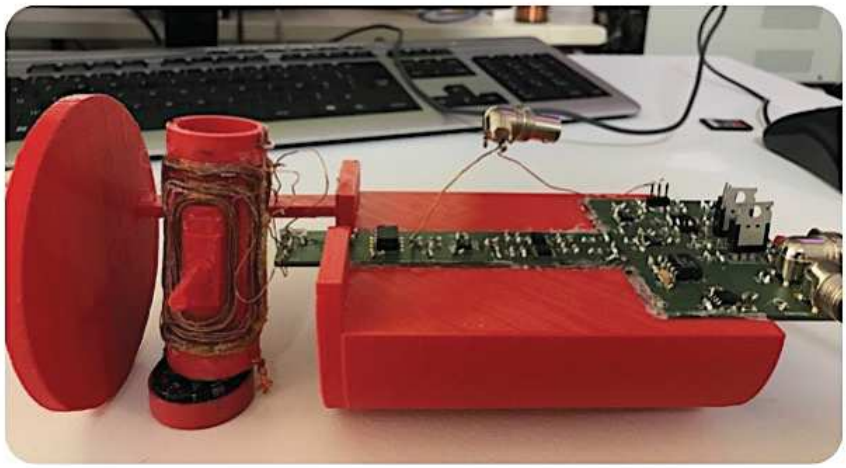

Figure 50 – Design and 3D printing of clipping antenna based on SHS 6 ($\theta_1 = 0.2035, \theta_2 = 0.4537, \theta_3 = 0.977$) configuration at $336kHz$ to keep the integrity of plant. Transmitter coil : $N_{turns} = 30$, Receiver coil is a Saddle coil : $N_{turns} = 90$ and $R = 20mm$

In fact, using the SHS method to build the new coil prototype while keeping the clipping configuration allowed us to improve the Q_{factor}, which doubled : $Q_{factor} = 80$.

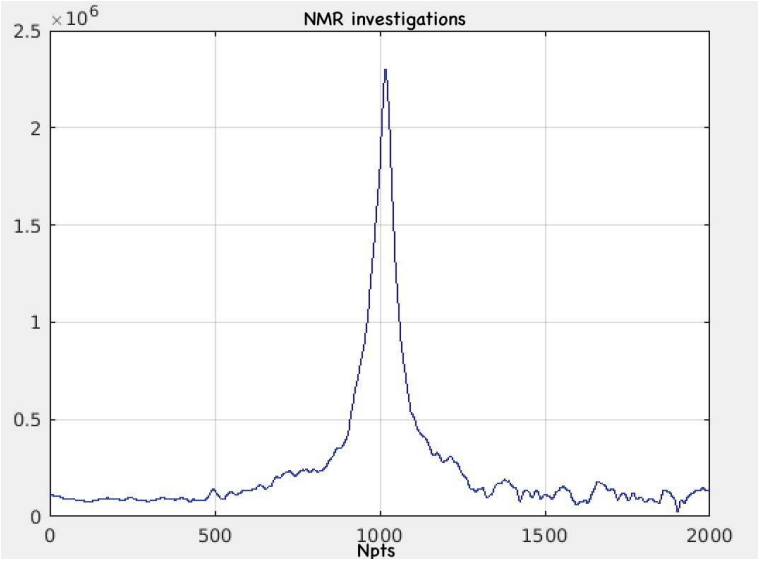

Figure 51 – ^1H NMR Signal of water reference obtained with our home made NMR system using One Pulse Sequence : $R_D = 1s, P_w = 375us$, acquisition time=$18mn$, 1point=6Hz at $336kHz$

The emergence of portable NMR system in recent years has opened a way for agronomic investigators to better understand the behavior of plants under global warming. Many efforts have been made to improve the techniques for early detection of plant under biotic and biotic stress and act accordingly. So far the Extended SHS method we used has given us the hope of having at our disposal the means to make a rapid, non-destructive and inexpensive detection of plant behavior directly in the fields.

.

Chapter 5. Multi scale investigations of sorghum plant

In agronomy, the use of multimodal data becomes "paramount", especially to highlight certain mechanisms such as the transport of water in plants. In particular, the coupling of morphological and functional images is of great interest. In fact, new multimodal imaging technologies increase our ability to jointly explore structural and functional properties of tissues and fruits. The Fig. 52 shows this huge potential by involving 3 technologies: MRI, Tomography and Histology to reconstruct a 3D image of internal structure of sorghum.

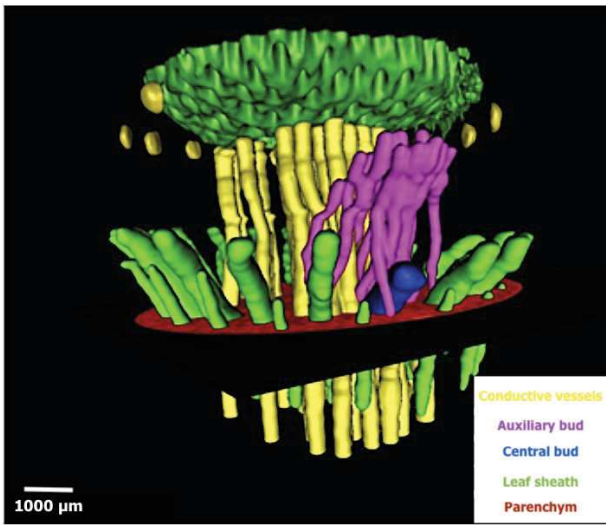

Figure 52 – 3D reconstrution of sorghum : highlighting the complexity of the sorghum internode by combining several technologies: MRI, Tomography and Histology - from BFF project images

In this chapter we will present two genotypes of sorghum duly chosen according to their differences investigated by: histology, MRI in the laboratory and low field NMR in the greenhouses and in the fields.

16 Histology investigations

This work achieved at CIRAD in the PHIV team (Plateforme d'Histologie et d'imagerie cellulaire végétale) under the BFF project (Biomass For the Future project funded by ANR)

aims to describe the anatomical and histochemical diversity of mature sorghum stems [Tirot, 2017]. This sorghum study shows how the tissue component varies within the stem. This will guide and support our interpretations from NMR / MRI.

The transverse histological sections of sorghum internodes using FASGA staining allows to distinguish two anatomical zones: an outer zone (OZ) and an inner zone (IZ), see Fig. 53 and Fig. 54. The outer zone is composed of an epidermis, a lignified support tissue composed of sclerenchyma fibers and numerous vascular bundles surrounded by sclerenchyma and composed of external phloem superimposed on the internal xylem. The inner zone is composed of parenchyma cells and vascular bundles arranged on several circles and have a lower density compared to the outer zone.

Thus, these results of anatomical phenotyping carried out at PHIV have demonstrated the presence of great anatomical diversity within the stem of sorghum plant for a panel for more than 300 genotypes, see Fig. 53. This anatomical diversity covers a large number of characters, such as the relative proportions of the outer zone and the inner zone, the percentage of sclerenchyma in the external zone or the density of the conductive fibers in the internal zone. Among the traits that vary greatly from one genotype to another with low variability between plants of the same genotype is the proportion of parenchyma in the inner zone that can be colored in blue or red by FASGA staining, see Fig. 53 and Fig. 54.

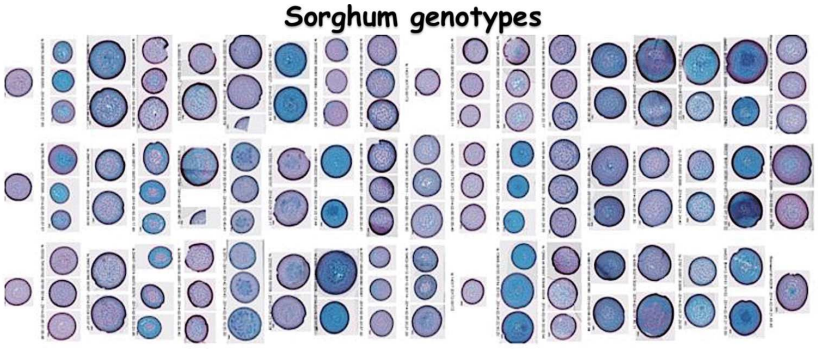

Figure 53 – Illustration of the "immense" diversity in the distribution of parenchymal Type B and R cells within the internodes of sorghum stems for 30 genotypes studied (FASGA staining)

In fact, FASGA staining distinguishes two types of parenchyma cells; cells called "Type R " which are stained red by FASGA and "Type B " cells whose wall is stained blue by this same staining. FASGA staining involves competition between two dyes the safranin and the alcian blue [Tolivia, 1987]. When the competition is in the profit of the safranin, the cells wall are colored in red and when it is the profit of the alcian blue, parenchyma cell wall takes a blue color.

It was shown that this anatomical trait influences very strongly the biomass quality and the potential industrial uses of sorghum (such a methanisation or the manufacture of sorghum fibers based on composite for car industry). Despite their importance, the so-called R and B cells are very seldom specified. The proportion and the localization of these parenchymental tissues in the inner zone varies from one genotype to another.

The Fig. 54 demonstrate an exemple of this "immense" diversity performed with FASGA staining which shows the presence and the distribution of R and B cells on four very contrasting genotypes.

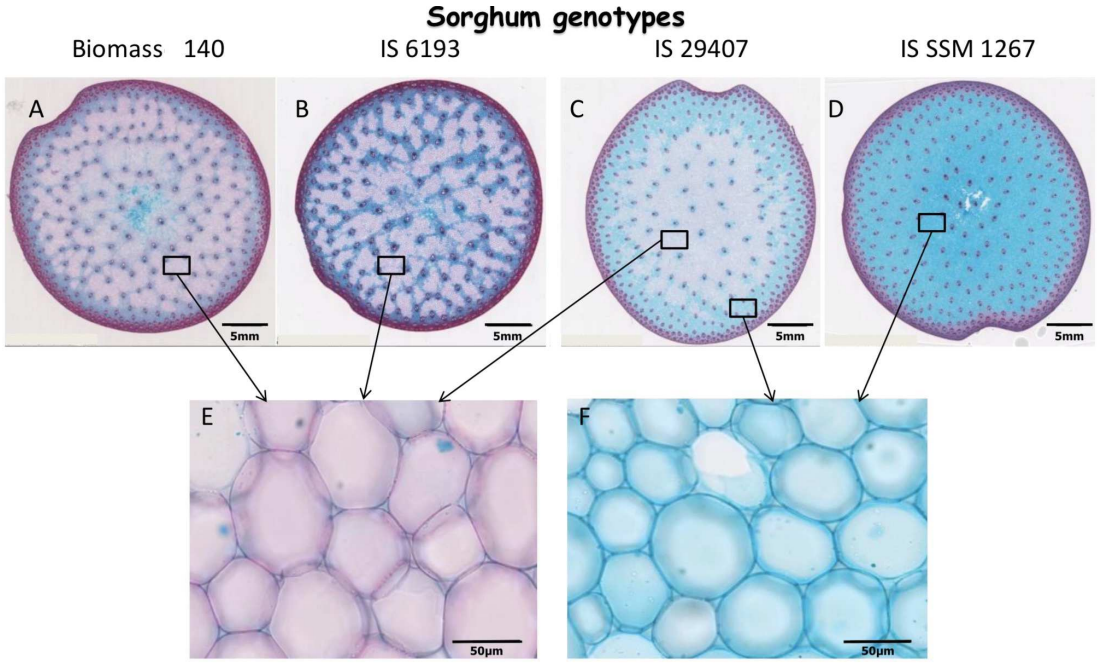

Figure 54 – Illustration of the "immense" diversity in the distribution of parenchymal cells Type B and R within the internodes of sorghum stems for 4 genotypes studied (FASGA staining) with optical microscope : Biomass 140 (A), IS 6193 (B), IS 29407 (C), IS SSM 1267 (D), cells of Type R (E) and Type B (F)

If FASGA allowed to distinguish two types of parenchyma cells in the inner zone of sorghum stem , in fact it is not a histochemically specific staining. In order to better understand the respective histochemical nature of the B and R Type walls, an accurate characterization of the two cell types has been performed [Tirot, 2017]. This additional comparative work has shown that :

Firstly, through the study showed in Fig. 55, when stem sections are treated with a mixture of cellulase and hemicellulase (enzymes specifically degrading cellulose and hemicellulose) during 72h, the wall of Type B cells is totally degraded (Fig. 55 G and H) , unlike the Type R cells that are protected from the action of these enzymes (Fig. 55 E and F). This study highlights that the walls of Type B cells are made of cellulose and hemicellulose.

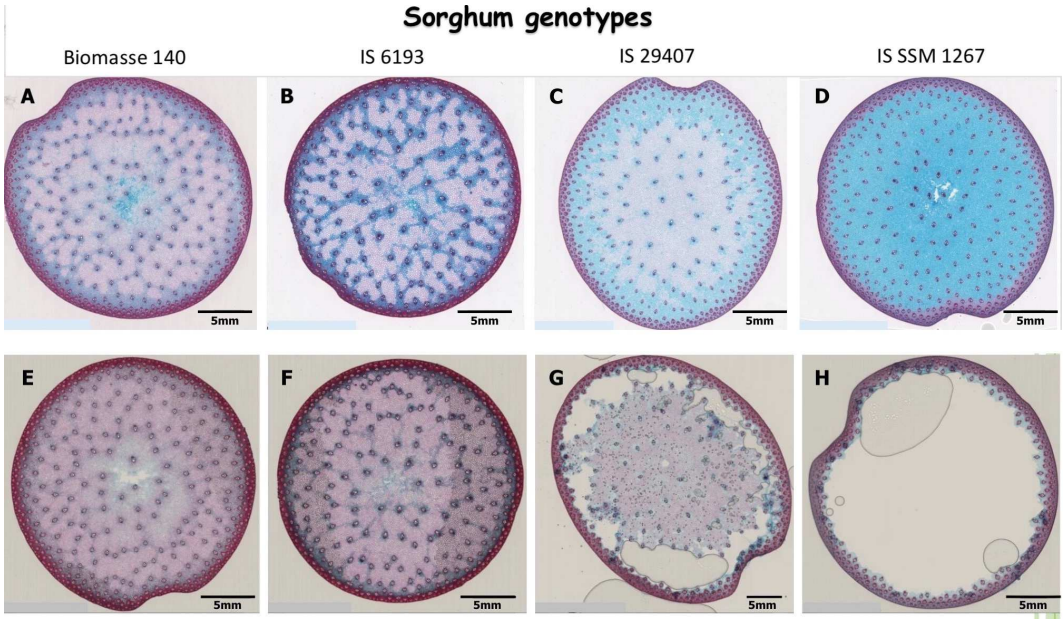

Figure 55 – Enzymatic hydrolysis of walls of Type B by hemicellulase treatment for 72h on cross sections of sorghum stem from all genotypes : Biomass 140 (A), IS 6193 (B), IS 29407 (C) and IS SSM 1267 (D) are the reference samples and Biomass 140 (E), IS 6193 (F), IS 29407 (G) and IS SSM 1267 (H) are the treated samples

The comparative study continued with the search for the presence of lignin or Suberin in R and B Type tissues, see Fig. 56. The lignin-specific staining (Phloroglucinol and Maule) are systematically negative for any type cells and for any parenchyma cell type (R and B) of studied genotypes (Fig. 56 A and C, B and D respectively). The walls of the Type B cells are not stained by the three stains used for the detection of Suberin (Berberine, Yellow Fluorol and Sudan Red (Fig. 56 F, H and J respectively). By contrast, the parenchyma cell walls of the Type R cells react positively to all three staining, regardless of the genotype (Berberine, Yellow Fluorol and Sudan Red (Fig. 56 E, G and I respectively). This study highlights the presence of the Suberin in the walls of the parenchym of some sorghum genotypes.

Finally, the results using the electron microscopy observations revealed significant differences in the thickness and the architecture of cells (Type R and B type)
[Tirot, 2017], see Fig. 57.

In conclusion, our histochemical and histoenzymatic data revealed that Type B parenchymal cells have a cell walls composed of cellulose and hemicellulose while Type R parenchyma cell walls contain Suberin. Suberin is an hydrophobic macromolecule that makes the walls impermeable to water, unlike cellulose and hemicelluloses, which are very hydrophilic macromolecules. This raises the question of the putative role of these two types of parenchyma cells in the water status of sorghum plants. To address this relevant question, we have subsequently chosen to study two genotypes contrasting genotypes: the Biomass 140 genotype which will

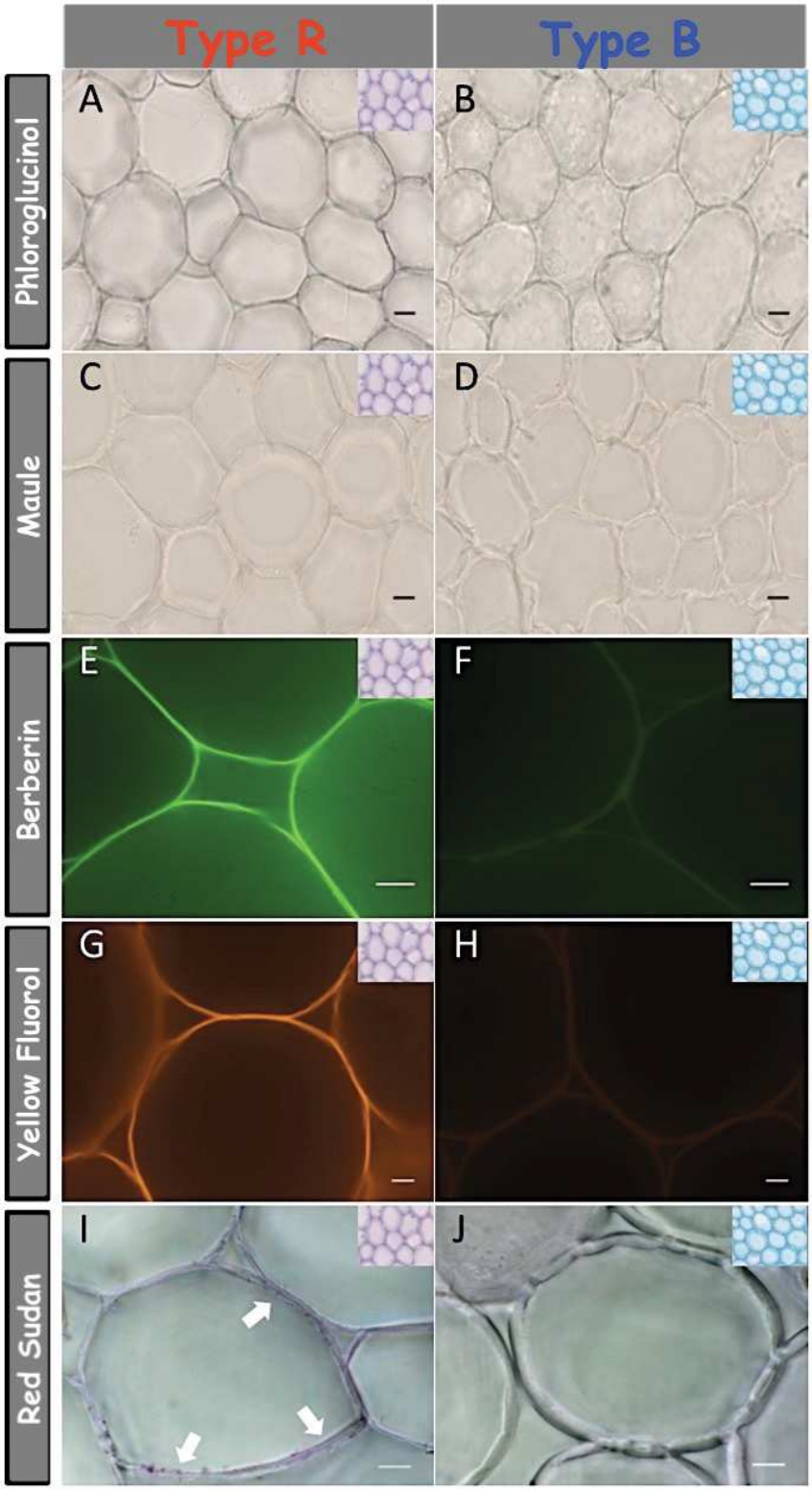

Figure 56 – Histochemical characterization of both parenchymal cell types: comparative detection of lignin and Suberin. Optical microscope observation of R-type (left column) and B-type (right column) cells after Phloroglucinol (A and B) staining, Maule (C and D) and Sudan red (I and J). Fluorescence microscope observation of R and B cells, after Berberin staining (E and F) and yellow Fluorol (G and H). The white arrows in Figure I underline the parietal markings of Sudan red. Resolution : black bars = $25\mu m$, white bars = $10\mu m$.

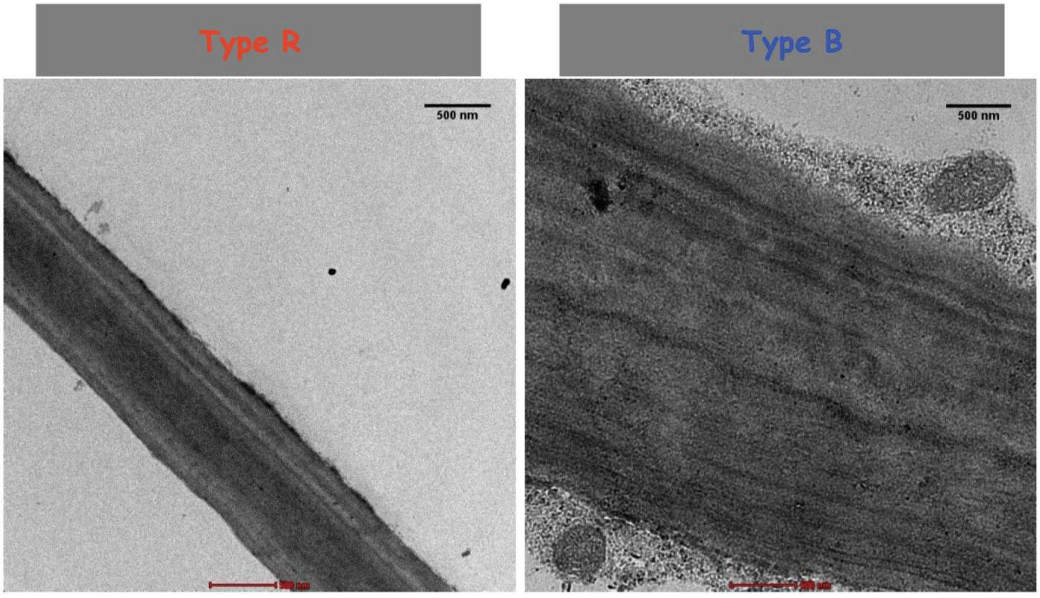

Figure 57 – Comparison of the thickness of the two types of parenchymal cells R and B with Transmission Electron Microscopy (TEM) observation. Type R (Biomass 140, A) and Type B (IS SSM 1267, B)

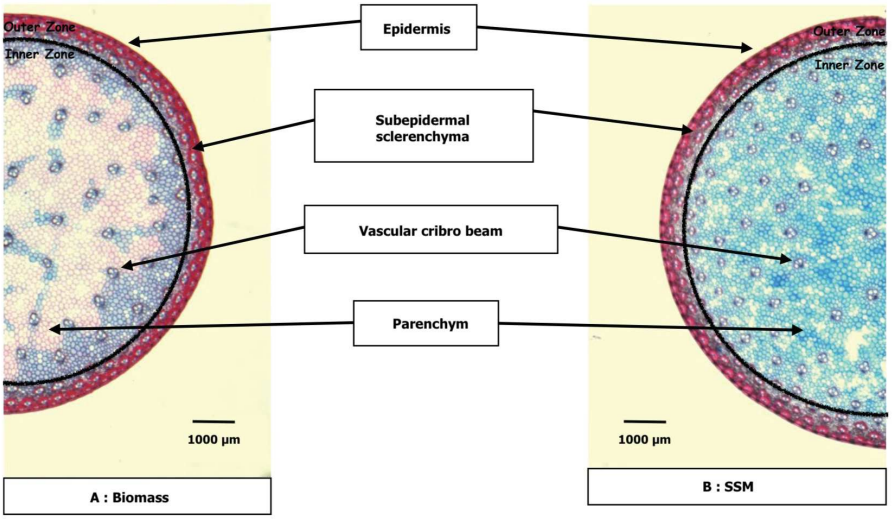

Figure 58 – Anatomy of sorghum stems (A : Biomass and B : SSM) - Transversal slices - FASGA staining

then be called "Biomass" for which the parenchymal cells of the inner zone of the stem are predominantly of Type R (66%) with some blue "bridges" between bundles and the IS SSM 1267 genotype which will then be called "SSM" for which these parenchymal cells are of Type B (87%), see Fig. 58.

16.1 NMR investigations in Climatic chamber at laboratory (80mT)

Plants are very sensitive to the environment in which they evolve. To ensure the reliability of NMR measurements at laboratory and to develop a low field NMR methodology, that reveals markers related to plant life under watered conditions and under stress, we have set up an electromagnet at $80mT$ corresponding to $3.5MHz$ for ^1H NMR in a climatic chamber. This chamber (heigh $3m \times 1m \times 1.05m$) was constructed in order to control the environment in which the plant grows, see Fig. 59. The enclosure, whose walls are made of polycarbonate, is mounted around an electromagnet (Drusch $gap = 36mm, 860kg, 6mT - 2T$) which has been raised by 1.50 m above ground level (to allow plant installation).

Various sensors have been installed inside the climatic chamber in order to characterize the surrounding environment of the plant as well as plant growth. There are arranged in the chamber sensors of brightness (2 ramps of LED's Alphaeus), temperature (Air heater) and humidity of the air (add of salty solution) in which the plant develops. Thus, the plant was subjected to a photoperiod of 12 hours per day and 12 hours per night. A measured PAR (Photosynthetically active radiation) at the leaf level of maximum of 600 $\mu molm^{-2}s^{-1}$ is found (when the sensor is placed just below the LED's. The temperature was adjusted at $28\pm1^{\circ}C$ during the day and $25\pm1^{\circ}C$ at night and the relative humidity is 70%. A comparative study of the growth of plants (Biomass genotype) reveals that they do not differ under the two types of conditions: greenhouses at CIRAD and NMR climatic chamber at laboratory.

Finally and following the preliminary study of design of RF coil (chapter 4), a clipping coil with its Tuning Matching circuit characterized by a resonant frequency at $3.5MHz(80mT)$ was constructed (the diameter of the coil is adapted to the diameter of sorghum).

In this climatic chamber we have first characterized the basic relaxation times T_1 and T_2 in sorghum (with respectively a Saturation sequence and CPMG sequence under NTNMR pulse sequencer). The investigations of these parameters reveal that there are two main components : a short and a long in M_0, $T_1(T_{1a} : 562ms, T_{1b} : 100ms)$ and $T_2(T_{2a} : 186ms, T_{2b} : 37ms)$.

The possibility of monitoring the M_0, T_1 and T_2 parameters in sorghum for several days is particularly interesting. In order to reproduce the experience at very low field with the portable NMR and to have several measurements per day, we have opted for a measure of the amount of magnetization M (with Saturation sequence under NTNMR pulse se-

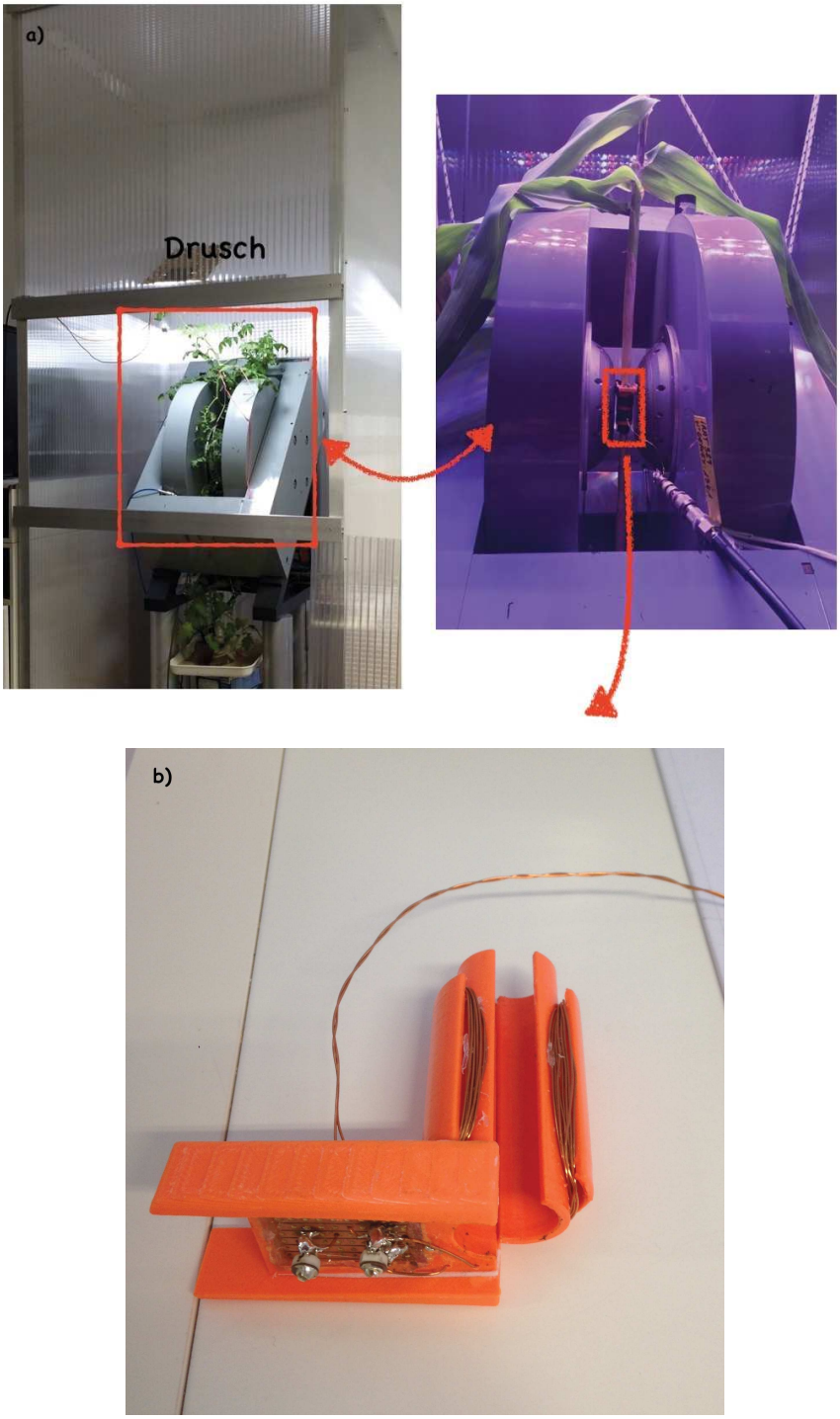

Figure 59 – a) Climatic chamber Setup at 3.5 MHz dedicated to study plants in suitable conditions at laboratory : Photoperiod 12h/12h, PAR= 600 $\mu molm^{-2}s^{-1}$, Temperature= $28^{\circ}C/25^{\circ}C$ and Humidity=70% b) Clipping RF coil with its Tunig Matching Circuit (N_{turns} = 30)

quencer) in sorghum stem with a daily watering for 15 days and with several Recovery Delay $(0.1s, 0.5s, 1s, 2s)$. This settings allows our measurement to be sensitive to either the short component or the long component.

The Fig. 60 shows an interesting result concerning the behavior of magnetization M. Indeed, for a very fast Recovery Delay, we don't observe fluctuations during day/night and for a Recovery Delay higher than $0.5s$ we observe day / night fluctuations in the plant.

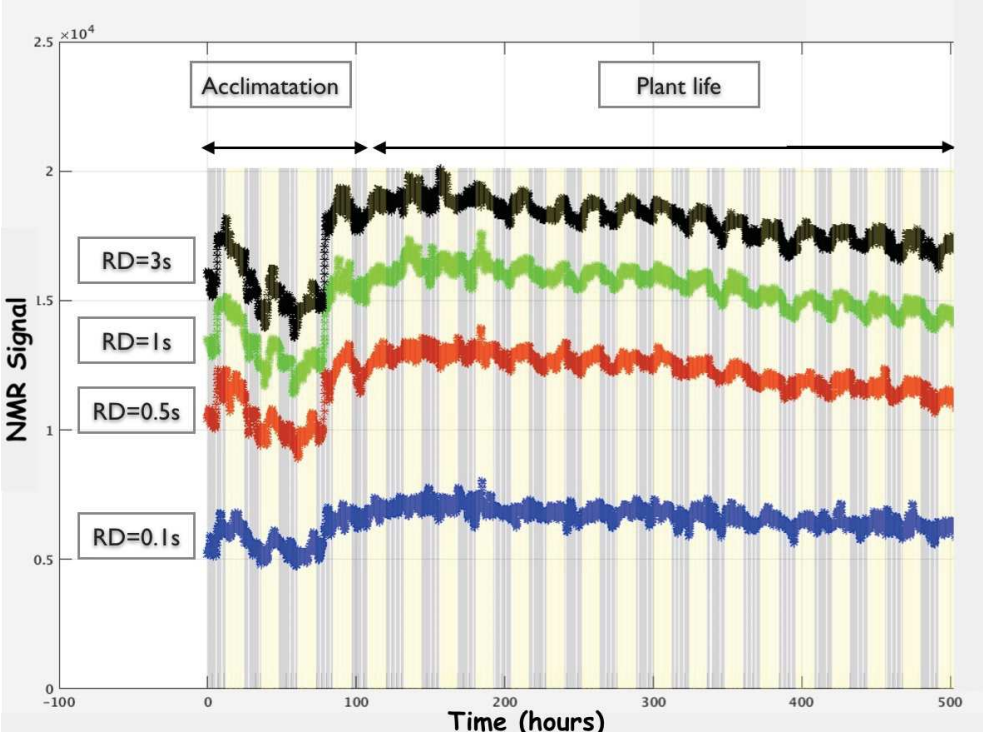

Figure 60 – Evolution in irrigated sorghum (BM genotype at stage of anthesis) of the NMR Signal (magnetization) at several Recovery Delay : $0.1s, 0.5s, 1s, 2s$: measures were conduced on the third internode below the panicle at the anthesis stage (Photoperiod 12h/12h, PAR= 600 $\mu molm^{-2}s^{-1}$, Temperature= $28^{\circ}C/25^{\circ}C$ and Humidity=70%)

In conclusion, this setup allowed us to develop a measurement methodology that revealed a presence of two NMR components with an interesting behavior in sorghum during day/night (Photoperiod 12h/12h, PAR= 600 $\mu molm^{-2}s^{-1}$, Temperature= $28^{\circ}C/25^{\circ}C$ and Humidity=70%), see Fig. 60. It is known that the short component is related to the tissue composition of plants while the long components are related to water content and water fluxes [Musse, 2009b]. This long component will be studied closely in the greenhouses to validate this behavior day/night with our protocol of measure and to study the behavior of the two contrasted genotypes (BM and SSM) under water stress.

17 MRI investigations at laboratory : comparative study of two contrasted genotypes

To decipher the relation between the two genotypes of parenchyma and their respective water contents status and better understand the role of these tissues during watered conditions and under stress, we conducted MRI investigations at BioNanoNMRI platform. For all our MRI measurements, a home made RF Saddle-coil (16mm) was installed at the level of the inter node 3 (from panicle) of sorghum at anthesis stage. The environmental conditions in the magnet were $20 \pm 1^{\circ}C$ at daytime and night-time. During the day, the light is provided by a panel of Leds.

17.1 T_2 distribution in BM and SSM

The Fig. 61.a shows T_2 The Fig. 61.a shows T_2 map within the transversal slice stem of the sorghum genotypes BM and SSM. We observe that the T2 maps of the 2 genotypes are different. The main difference concerns the inner zone constituted of the tissues of the parenchyma (BM : Type R and SSM : Type B). In BM genotype, theses investigations revealed that the zones composed of Type R cells give no signal in MRI, see Fig. 61.a. We observe also in the BM, bridges that could act as a functional cells, connecting the bundles between them and allowing cell / cell communication even within a parenchyma.

The Fig. 61.b shows that the analysis of T_2 distribution within the Sorghum stem reveals that the zones composed of Type B cells are hydrated and full of water.

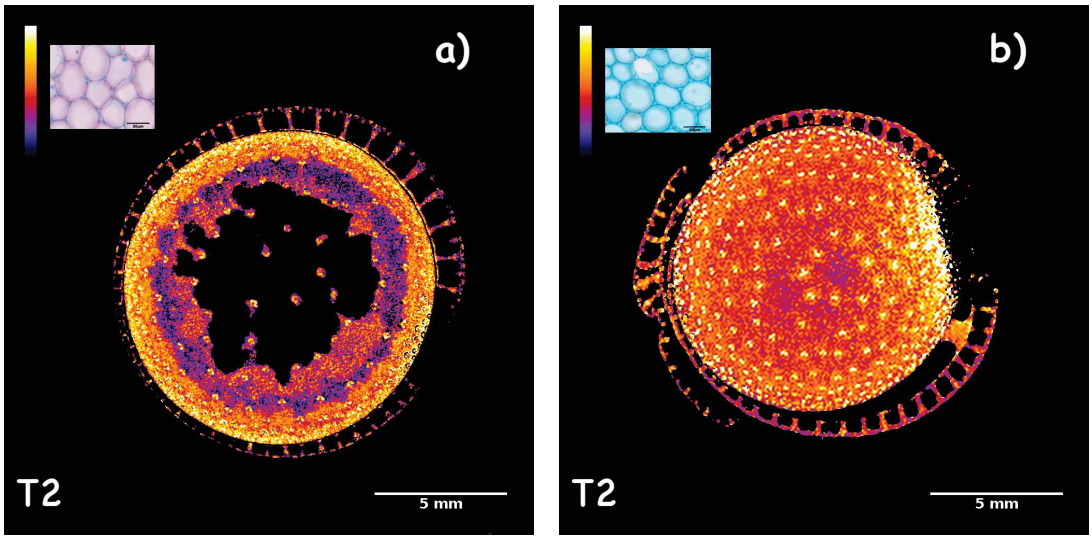

Figure 61 – Comparaison of BM and SSM genotypes by High Resolution MRI ^1H at $9.4T$ at internode 3 at the anthesis stage : T_2 maps of a) BM and b) SSM. MRI parameters used is : MEMS sequence with $TR = 5000ms, TE = 10.84min, Slices = 4, Thickness = 0.5mm, FOV = 20mm \times 20mm$.

17.2 M_0, T_2 and R_2 distributions in BM in watered and no watered conditions

The Fig. 62 shows that in the BM genotype, the so-called Type B cells which constitute a part of the parenchyma in the inner zone disappear during a water stress. This tissue shrinkage leads to a loss of 48% in water content, see Fig. 62.a & .b.

The so-called "bridges " (Type B cells) localized in the parenchyma in the inner zone disappear also in no watered conditions.

The subepidermal sclerenchyma of the outer zone is also affected by stress, the Fig. 62.c & .d shows a decrease of T_2 from $56ms$ to $39ms$ in this zone.

Finally, we also observe that after stress most vascular bundles in the inner zone give no signal in MRI.

17.3 M_0, T_2 and R_2 distributions in SSM in watered and no watered conditions

The Fig. 63 shows that in the SSM genotype, the so-called Type B cells which constitute mainly the parenchyma decreases very slightly in the inner zone.

As for the BM, the subepidermal sclerenchyma of the outer zone is also affected by stress, the Fig. 63.c & .d shows a decrease of T_2 from $51ms$ to $30ms$ in this zone.

The vascular bundles of the SSM do not seem very affected by the stress unlike the BM (the T_2 is about the same at $25ms$).

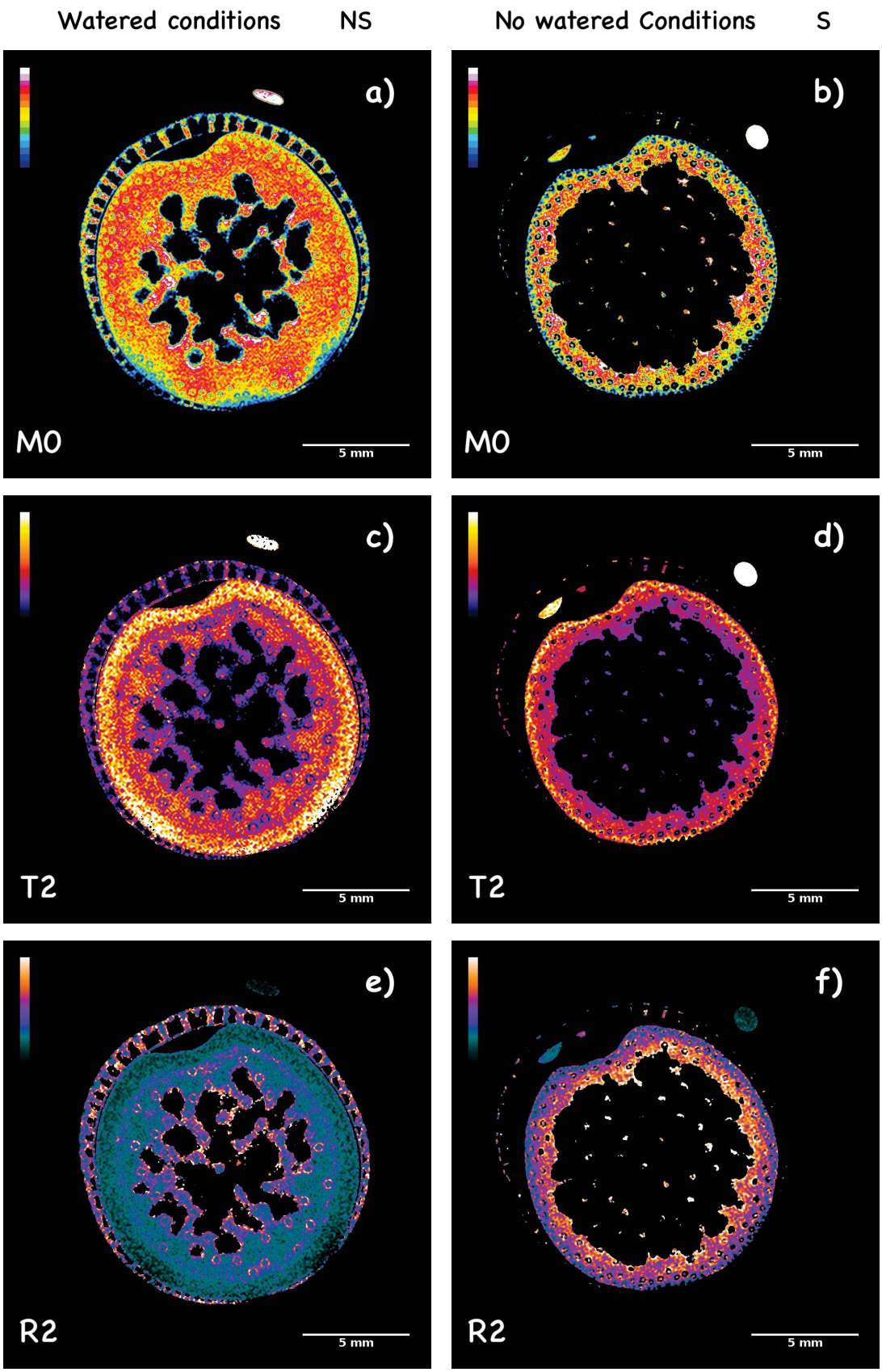

Figure 62 – Comparaison of BM sorghum in watered conditions (no stress : NS) and no watered conditions (during stress : S) by High Resolution MRI ^1H at $9.4T$ at internode 3 at the anthesis stage : M_0 maps a) NS and b) S, T_2 maps c) NS and d) S and R_2 maps e) NS and f) S with water reference. MRI parameters used is : MEMS sequence with $TR = 5000ms, TE = 10.84ms, Slices = 4, Thickness = 0.5mm, FOV = 20mm \times 20mm$.

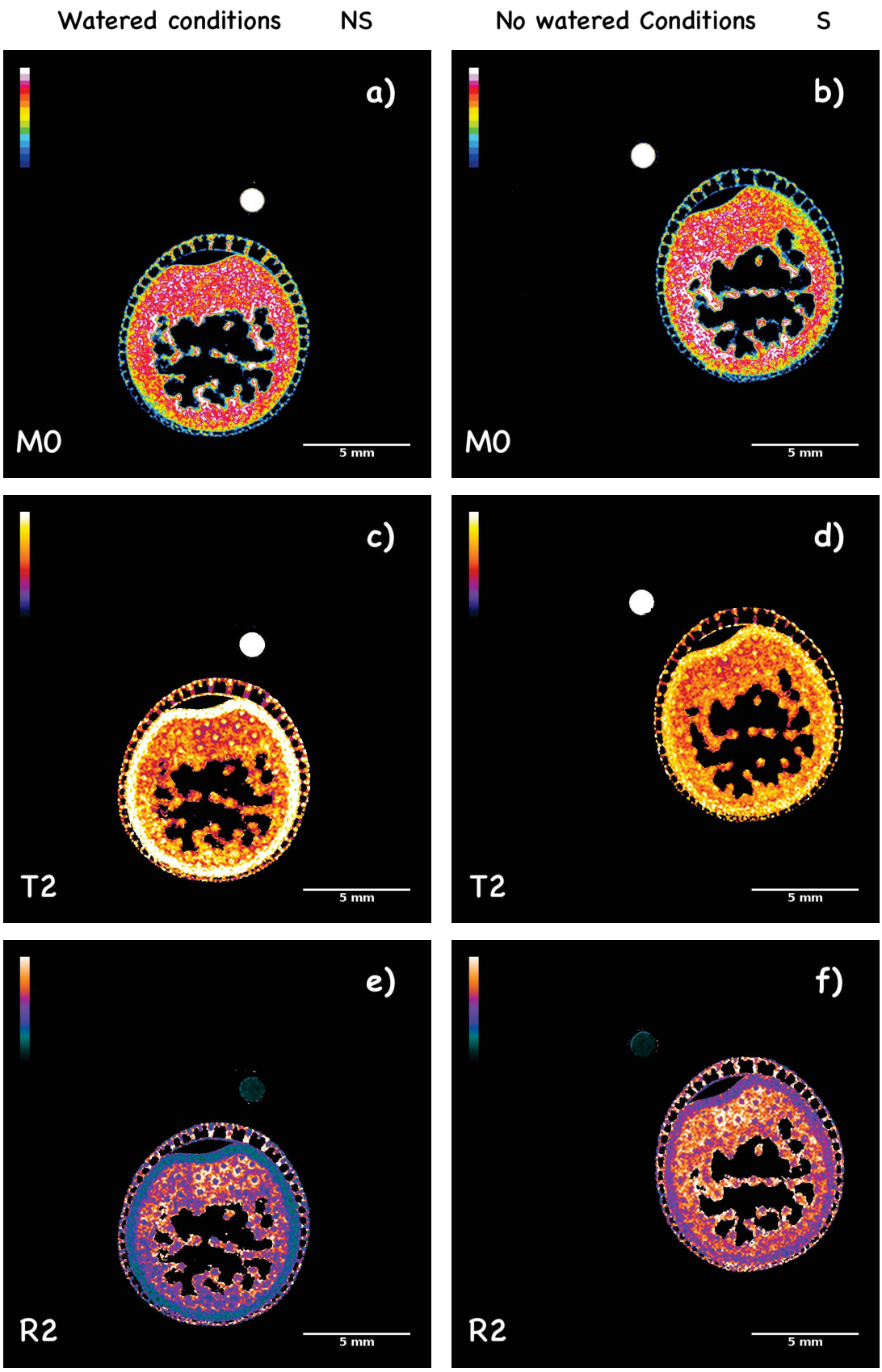

Figure 63 – Comparaison of SSM sorghum in watered conditions (no stress : NS) and no watered conditions (during stress : S) by High Resolution MRI ^1H at $9.4T$ at internode 3 at the anthesis stage : M_0 maps a) NS and b) S, T_2 maps c) NS and d) S and R_2 maps e) NS and f) S with water reference. MRI parameters used is : MEMS sequence with $TR = 5000ms, TE = 10.84ms, Slices = 4, Thickness = 0.5mm, FOV = 20mm \times 20mm$.

17.4 Water fluxes investigations

The investigations of plants health within the agro-ecosystem is becoming essential. A key for these studies would be to monitor the "flow dynamic" of saps in living plants. In this context, the flip-flop flow-MRI method was used to monitor the flow in plants in a non-invasive way. In our case, we investigate sorghum genotypes in watered conditions (BM and SSM) at 9.4T [Buy, 2018]. According to this method, a double Spin Echo Multi Slice (SEMS) sequence available on Agilent MRI is used with a common slice and opposite directions of the slice selection order (in our case, we set up 4 slices). The Fig. 64 is a simplified illustration to explain the principle of Flip Flop method.

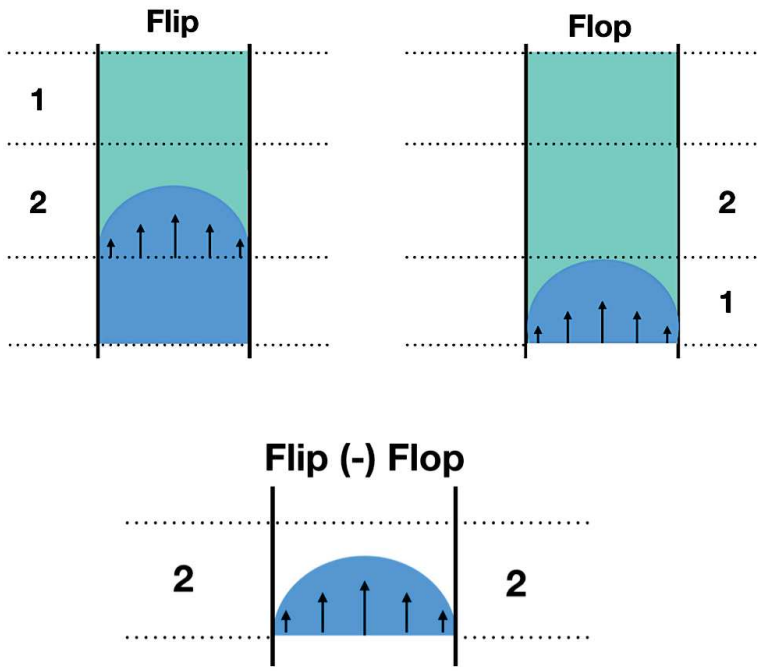

Figure 64 – Illustration of Flip Flop method : In presence of a bidirectionnal flow, the second slice of flip will be sensitive to the positive direction inflow while the second slice of flop will be sensitive to outflow.

The first MRI sequence will be called "flip" and will be sensitive to the influx of saturated spins which induces an increase of the signal, see Fig. 64. During the flip acquisition, the resulting signal in the common slice according to [Buy, 2018] is:

$$S_{flip} = A_{fov} k_c (M_0^m e^{-\frac{T_E}{T_2^m}} (T_{hk}(1 - e^{-\frac{T_R}{T_1^m}}) + vT_R e^{-\frac{T_R}{T_1^m}}) + M_0^s e^{-\frac{T_E}{T_2^m}} T_{hk}(1 - e^{-\frac{T_R}{T_1^m}})) \quad (74)$$

Where v is the velocity, A_{fov} is the voxel surface, k_c is the coil sensitivity coefficient, T_{hk} thickness of slice , $M_0^m$and T_1^m are the magnetization and the T_1 relaxation time assuming

the velocity and M_0^s and T_1^s are the magnetization and the T_1 relaxation time of the partial magnetization of static spins.

The second MRI sequence will be called "flop", there is still a fraction of flow exhibiting negligible magnetization which enters into the slide, due to the T2-weighted flow effect, during $N_s \times$ TE, where N_s is the number of slice. During the flop acquisition, the resulting signal in the common slices and in the case of distributed T_R according to [Buy, 2018] is :

$$S_{flop} = A_{fov} k_c (M_0^m e^{-\frac{T_E}{T_2^m}} (T_{hk}(1 - e^{-\frac{T_R}{T_1^m}}) + v\frac{T_R}{N_s}(e^{-\frac{T_R}{T_1^m}} - e^{-\frac{T_R/4}{T_1^m}} + M_0^s e^{-\frac{T_E}{T_2^m}} T_{hk}(1 - e^{-\frac{T_R}{T_1^m}})) \tag{75}$$

A difference between the two acquisitions flip and flop thereby permits to cancel the static spin contribution (from Eq. (74) and (75)) while contribution of the moving spins only remains according to :

$$S_{flip-flop} = \pm A_{fov} k_c M_0^m e^{-\frac{T_E}{T_2^m}} v T_R((1 - \frac{1}{N_s})e^{-\frac{T_R}{T_1^m}} + \frac{1}{N_s} e^{-\frac{T_R/N_s}{T_1^m}}) \tag{76}$$

The Fig. 65.a & .c represent anatomic images of both BM and SSM genotypes respectively under watered conditions and during the day. The Fig. 65.b & .d represent the anatomical images superimposed with the flow images obtained with the flip flop method.

These results show that only xylemian conductive bundles are active in the two genotypes BM and SSM. This method allows also to calculate the conducting surface in the BM $0.929mm^2$ and in the SSM $0.65mm^2$.

The flip flop method allows us to identify the conductive bundles but also to quantify the speed of the sap in these bundles. Experiments were run at different TR values (from 400ms up to 1600ms). The evolution of the average signal on a conductive bundles at different T_R is investigated by the fitting method using :

$$v_{moy} = H(\frac{T_{hk}}{v_{max}} - T_R)(\frac{v_{max}}{2}) + H(T_R - \frac{T_{hk}}{v_{max}})(\frac{T_{hk}}{T_R}(1 - \frac{1}{2v_{max}}\frac{T_{hk}}{T_R})) \tag{77}$$

where $H(u)$ is the Heaviside step-function such as $H(u) = 0$ for $u < 0$ and $H(u) = 1$ for $u > 1$.

The velocity study using this method is presented in Fig. 66. According to our fits, we find an estimation of the speed in the BM and the SSM of $0.5mm/s$, see Fig. 66. We conducted also a flow investigations in both genotypes under no watered conditions but they are not very exploitable because both genotypes were in an advanced state of stress.

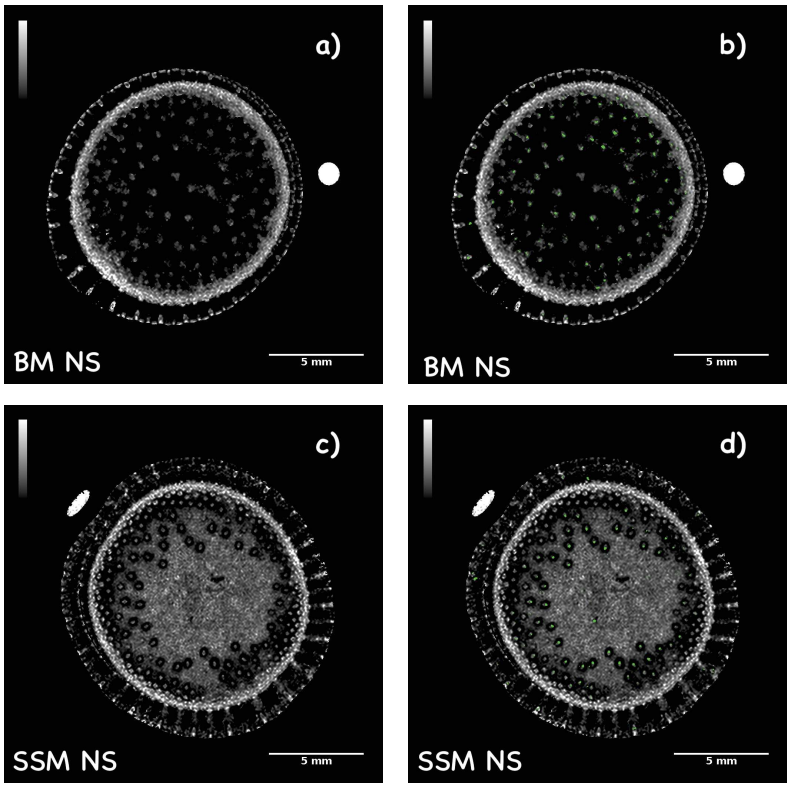

Figure 65 – Illustration of the vascular bundles on BM and SSM stem. a) and c) Anatomical image acquisition of BM and SSM respectively ($T_R = 1.2s$, $TE = 10.84ms$, Slices=4, $FOV = 20mm \times 20mm$ and T_R is distributed) b) and d) Superimposition of the anatomical acquisition (background) with the flow acquisition in green by $T_1 - weighted$ Flip-Flop sequence (only the active xylemian tissues appear)

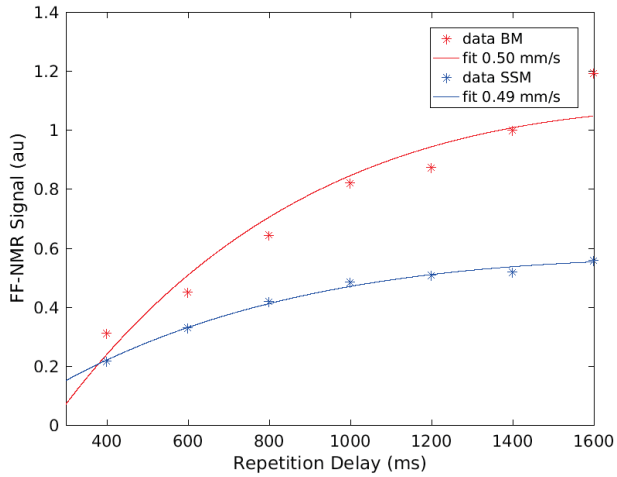

Figure 66 – Quantification of the flow velocity of BM and SSM sorghum thanks to a segmentation applied on the regions concerned by the flux as a function of the repetition time T_R (400ms-1600ms)

18 NMR Low Field investigations in greenhouses (8mT)

Finally, we conducted a comparative investigations of water status of these two anatomically contrasted genotypes at CIRAD using the facilities of the ecophysiology platform. We had at disposal a series of two contrasted genotypes Biomass and SSM at maturity with the distribution of the cells Type B and Type R within the parenchyma quite differente.

18.1 Experimental design

The experiment was carried out on greenhouse-grown sorghum plants in plastic sheaths (diameter 28 cm, height 50 cm) containing potting soil (a mixture of 1/3 pozzolan, 1/3 Neuhaus soil S, 1/3 soil Neuhaus $N°2$). The amount of potting compost was adjusted to $2.6Kg$ per plastic sheaths for all the plants of each genotype. The plants were regularly watered from seedling to the panicle emission stage at which the measures were carried out. At this stage 3 homogeneous plants were selected for each genotype.

At the beginning of the experiment, these plants were watered until substrate saturation and after freely draining the excess water, the soil was hermetically sealed in a plastic bag to prevent soil water evaporation and privilege the water losses by the aerial parts by the mechanism of transpiration (to allow the measurement of the water fraction transpired by the plant (FTSW), by weighing). To be able to compare the two genotypes we install two NMR systems in the greenhouse that allow to monitor simultaneously the evolution of the NMR parameters according to the water stress under the same environmental conditions, see Fig. 67.

For each NMR system, a NMR clipping coil is placed around the inter node 3 from the panicle whose the diameter varies between 12 and $20mm$ depending on the genotypes and all is brought to the center of the NMR setup.

In the greenhouse at CIRAD, various sensors (temperature, air relative humidity, light intensity) have been installed in order to characterize the growing environment of the plant. Thus, there are arranged in the greenhouses sensors of light, temperature and the air humidity

.

A connected weight scale has also been added under each plant for the monitoring of the weight losses, see Fig. 67. Indeed, the monitoring of the weight allows us to calculate the Fraction of Transpirable Soil Water (FTSW). The FTSW investigations allows us to study the hydric behavior of plants and reflects an estimation of the fraction of soil water usable by the plant, which fluctuates with rainfall inputs, soil evaporation and transpiration losses from the vegetation [Masinde, 2005].

$$FTSW = \frac{W_D - W_F}{W_I - W_F} \tag{78}$$

Where:

W_D : weight of the day

W_F : final weight (when the weight becomes stable)

W_I : initial weight (water saturated soil)

The experiment was reproduced three times independently (between April and June) and the obtained results were similar.

Transpiration and photosynthesis rate measurement : Leaf transpiration rate (E, in $mmolm^{-2}s^{-1}$), stomatal conductance ($GH2O$, in $mmolm^{-2}s^{-1}$), the CO2 assimilation rate (A_s, in $\mu molm^{-2}s^{-1}$) and the intercellular $CO2$ mole fraction (ci, in ppm) were measured from 10 am with a Portable Gas Exchange Fluorescence System (GFS-3000). It was measured on the well exposed leaf of the phytomer corresponding to the internode 3 below the panicle.

18.2 Measurement method of the NMR signal

A one pulse T_1- weighted sequence on a pulse sequencer (Chameleon, RS2D Compagny) was modified and adapted in order to drive a dual Transmitter/Receiver system operating at the resonant frequency of protons at $336kHz(8mT)$ with a recovery delay (R_D) of $1s$. The NMR signals corresponding to each NMR device are presented in red for the first apparatus and blue for the second one.

The Fig. 68 shows the NMR spectrum of the water tubes (control) measured with the two devices. The homogeneity performance of our two systems measured from the line width is about $600ppm(150Hz)$ on a total water volume of $4cm^3$.

The difference between the two red and blue signals in terms of SNR (see Fig. 68) is due to the sensitivity of the TxRx devices showing different characteristics. The first system it is a SHS 6 coil of $20mm$ in diameter and the second one is a Saddle of $15mm$ in diameter (you can find design details in chapter 4). The diameter of the control water tubes is identical and measures 1cm in diameter.

We also note that the two signals have an offset with respect to the observation frequency at $336kHz$ ($Nbpts = 1024$ and spectral width $S_W = 12kHz$)which is due to several factors including current supply stability (in our case we use laboratory power supply which is not

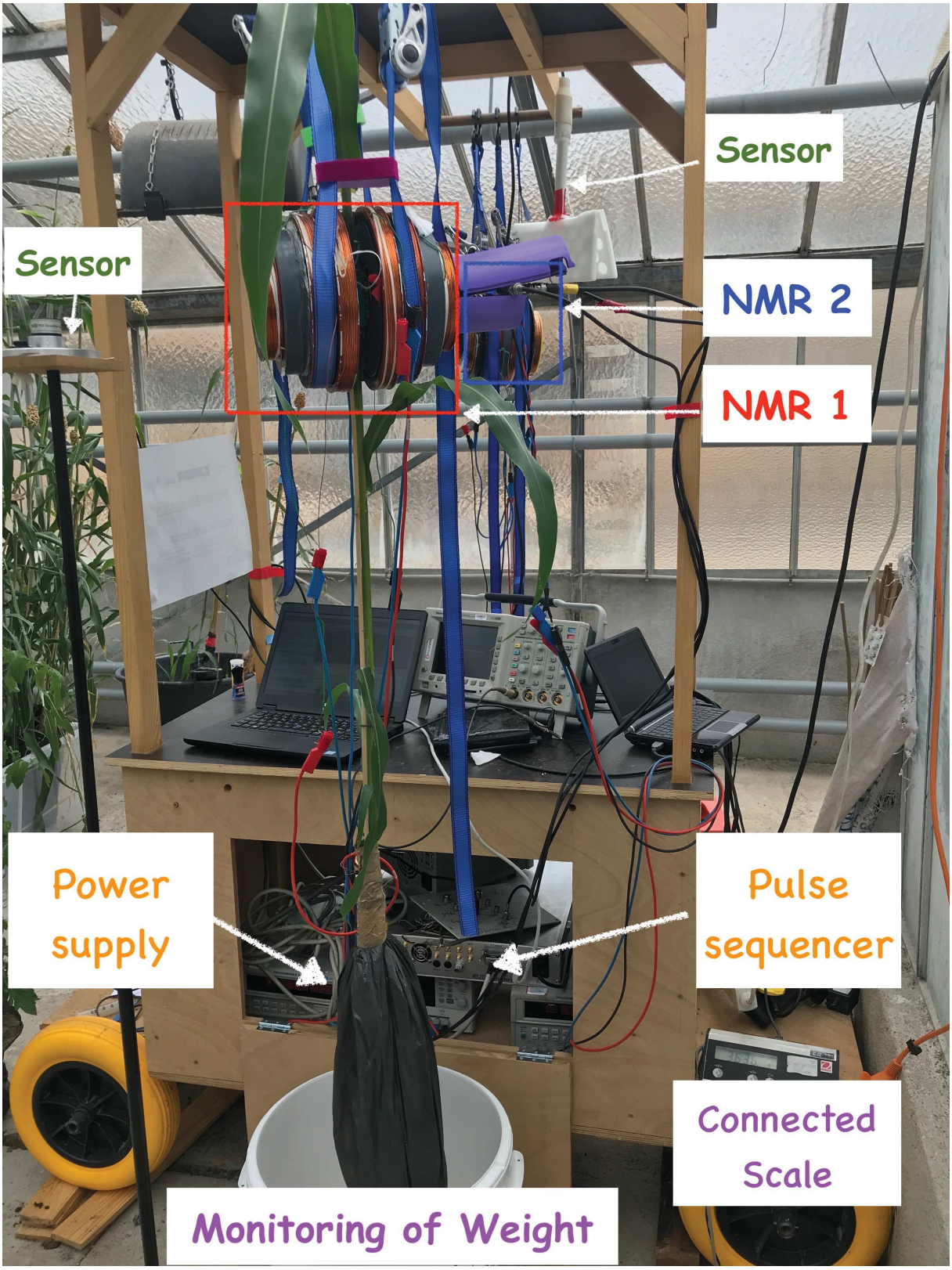

Figure 67 – Double NMR setup at 336kHz installed in the greenhouse with a weather station (measurement of temperature, light intensity and air humidity)

intended to feed NMR relaxometers).

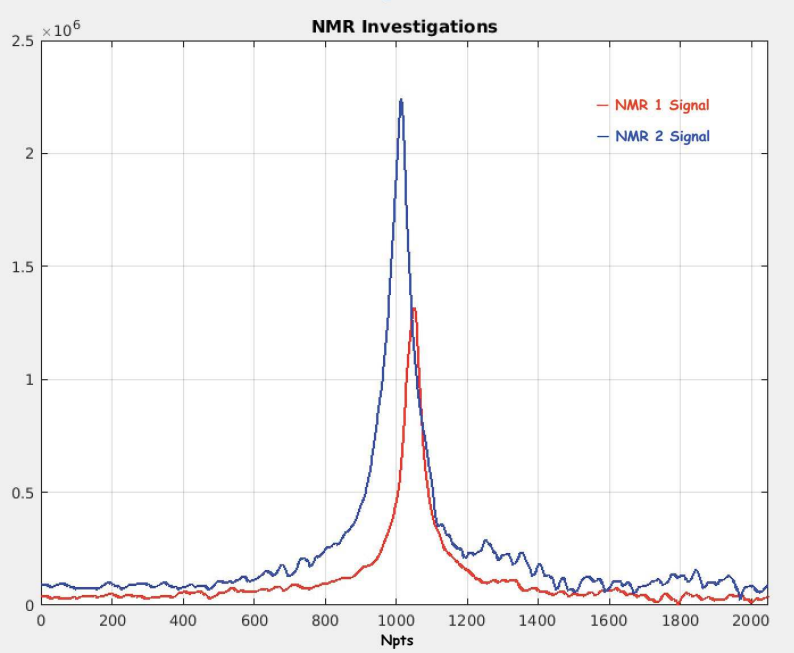

Figure 68 – ^1H NMR Signal of water reference obtained with our double NMR system using the same One Pulse Sequence : $R_D = 1s$, pulse width $(\pi/2)$: $P_w = 375us$, acquisition time=$18mn$, 1point=6Hz at $336kHz$

Another factor that can affect the stability of the experiment in outside the laboratory or in fields is the environmental temperature variations. In greenhouses, to tackle this important we have repeated the experiment shown in Fig. 68 during 3 consecutive days in order to monitor the evolution of the water signal over time and investigate the dependence of the signal as function of the temperature in greenhouse at CIRAD.

During these 3 days we therefore have a number of experience equal to $3 \times 24 \times 60mn$ / acquisition time = $18mn$. To process them we have implemented under MATLAB software a process created specifically.

First, this protocol allows to proceed to a series of basic steps of preprocessing of the NMR signal. This has for main objective the improvement of the quality of the signal by the application of a line broadening (L_B) or the Left shift L_s which makes it possible to remove the few first points affected by " Ringing ".

Then, this process allows to :

- Load and organize data and integrate the NMR signals from two devices according to the number of desired points (on the spectrum),
- Calculate the Noise (on the FID),
- Calculate the shift of the NMR signal from the observation frequency.

We obtain these information for each acquisition time elapsed.

The Fig. 69 shows the dependence of the ^1H NMR signal of water : Intensity, Noise, Shift as a function of measured temperature during 3 consecutive days in the greenhouse.

The Fig. 69.a presents the dependence of the signal as a function of the temperature that varies during day / night. The red NMR signal (NMR 1) fluctuates of 25% while the blue NMR signal (NMR 2) fluctuates less than 10%.

The Fig. 69.b presents the dependence of the Noise as a function of the temperature that varies during day / night. The red Noise signal (NMR 1) fluctuates of less than 5% while the blue Noise signal (NMR 2) fluctuates of 15%.

Finally, the Fig. 69.c presents the dependence of the shift of NMR signals according to the temperature that varies during day / night has been invested shows that the red and blue curve fluctuates of less than $10Npts$ which corresponds to 60Hz.

In conclusion, these investigations show that we must consider the temperature that affects particularly the stability of both the NMR signal and Noise. The effect of temperature on the shift is negligible. The calculation of the SNR does not make it possible to remedy this dependence.

To compensate this problem and from the signals presented in Fig. 69, we have studied a polynomial curves fitting lines (second order) in order to find correlations between the different studied parameters and the temperature.

In order to be able to apply our corrections to a real sample for which the signal varies a lot like in living plants we have opted for a temperature correction found from the Noise signal. The Fig. 70.a and 70.b shows the improvement on the Noise signals and the NMR signals. Indeed, the dependance on temperature are now negligible (less than 5 %) in both NMR systems which allows us to consider studies in living plant.

Finally, the Fig. 70 represents the typical behavior of the corrected NMR signal evolution over time. This correction will be used to compare the behavior of plants over time from the two anatomically contrasted genotypes (BM and SSM) under watered and no watered conditions.

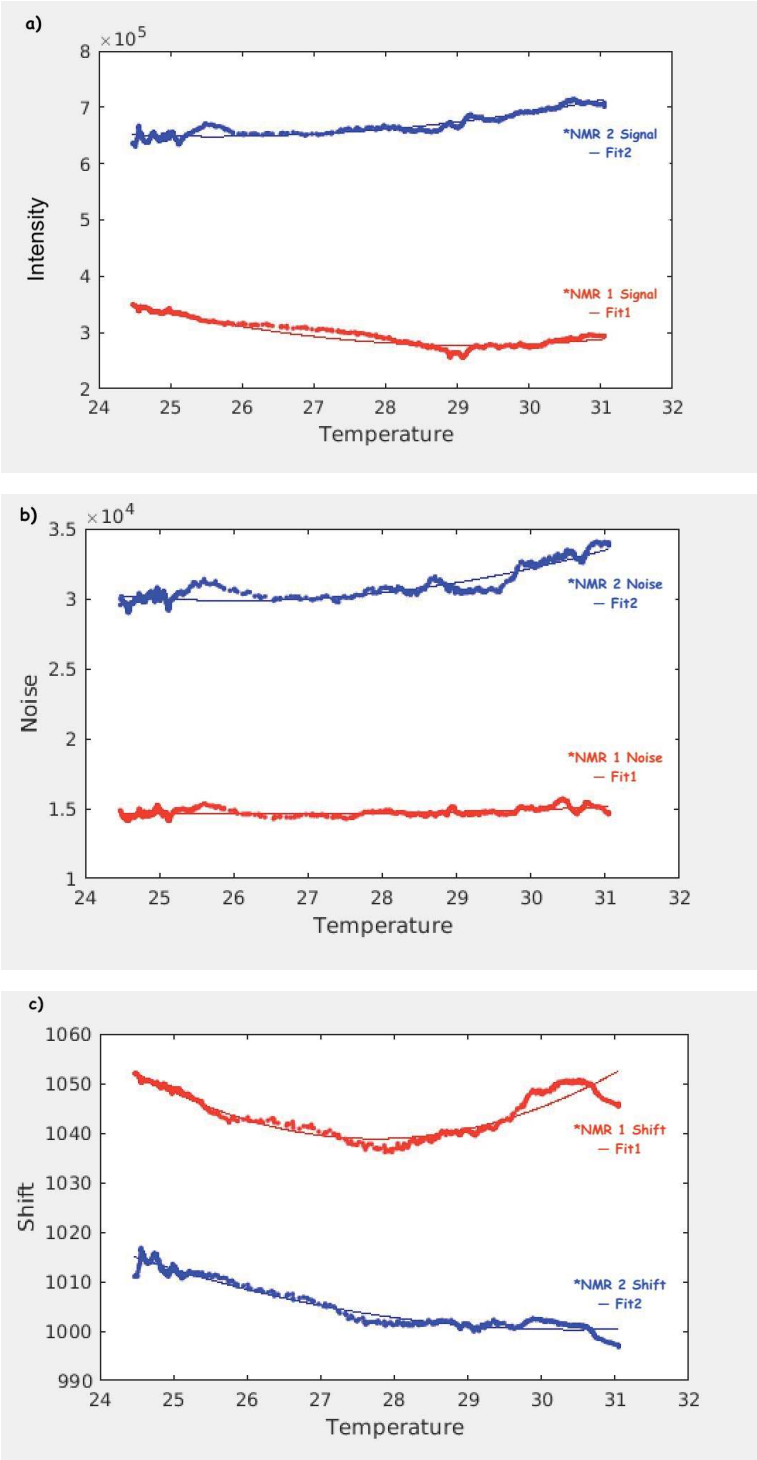

Figure 69 – Evolution of (a) NMR Signals and (b) Noise over time (c) shift of NMR Signals of water reference according to the temperature with their polynomial fitting curves

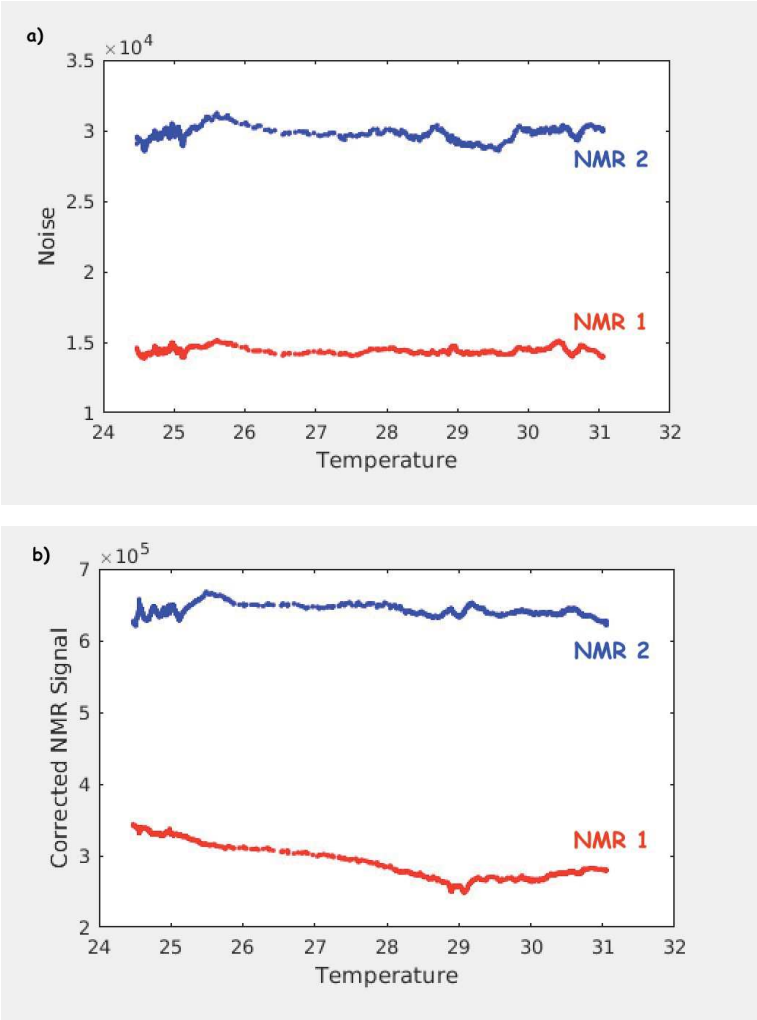

Figure 70 – Corrected NMR Signal of water reference by the dependance of temperature obtained on Noise

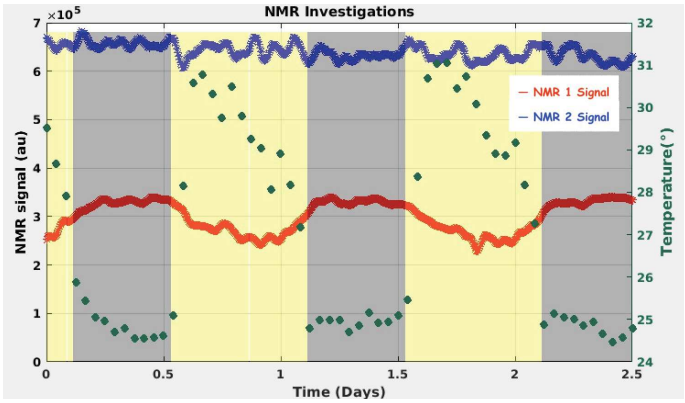

Figure 71 – Corrected NMR Signal of water reference by the dependance of temperature obtained on Noise

18.3 Investigations of the behavior of NMR signal to an incoming flow

After finding a method to compensate the variations in the water signal as a function of the outdoor temperature, a final step in the development of a NMR method suitable for monitoring plant water status in the greenhouse was to test the sensitivity of our system to an incoming flow for velocities measurement in plants (xylemian and phloemian fluxes : velocity range in xylem= 0-5mm/s and phloem = 0.4mm/s, [Vans As, 1984 and 1985]).

For this, we have set up a pump that allows to flow water in one direction in a silicone tube of $1cm$ diameter, see Fig. 72. a. The effect of water inflow accelerates the signal towards the full relaxation due to the introduction of fresh spins, see Fig. 72 .b. The full magnetization depends on the R_D delay and the thickness of the slice. In our case, the thickness is the whole area where the Rx coil is homogeneous (6mm).

The Fig. 73.a shows the recorded NMR signal as a function of the R_D in the case where we have a flow (red curve) and in the case where we have no flow (blue curve). This reveals that there is a significant difference between the signal with and without flow. The fitting using flip flop method (signal vs several R_D) allows us to quantify also the water speed of a fixed water speed of $3.7mm/s$ [Buy, 2018]. We also notice that the greatest difference is observed at $R_D = 2.3s$ which corresponds to T_1 of water at 336kHz.

The Fig. 73.b shows the behavior of the NMR signal at different velocities (0-8mm/s) with a constant R_D (1s). This shows an increase in the NMR signal as a function of the water speed. When the speed is greater than the thickness of the slice / R_D, our system is no longer differentiates the speeds this explains the flat curve reached at $6mm/s$ for $R_D = 1s$.

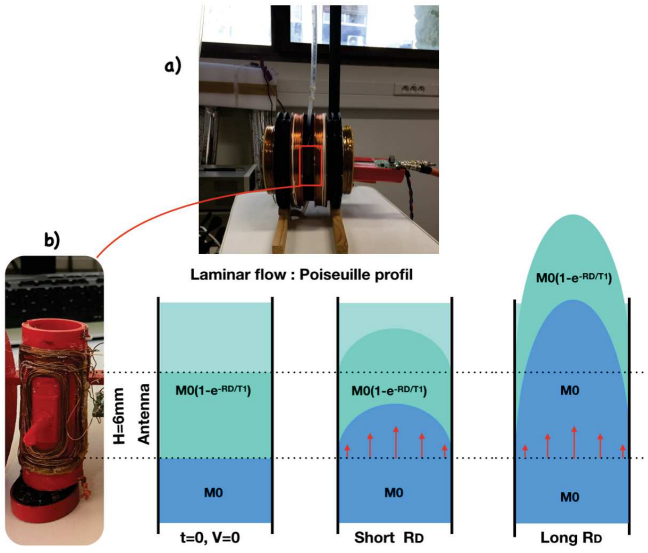

Figure 72 – a) NMR flow setup b) Laminar flow profile inside antenna : Effect of water inflow as function of R_D delay on magnetization

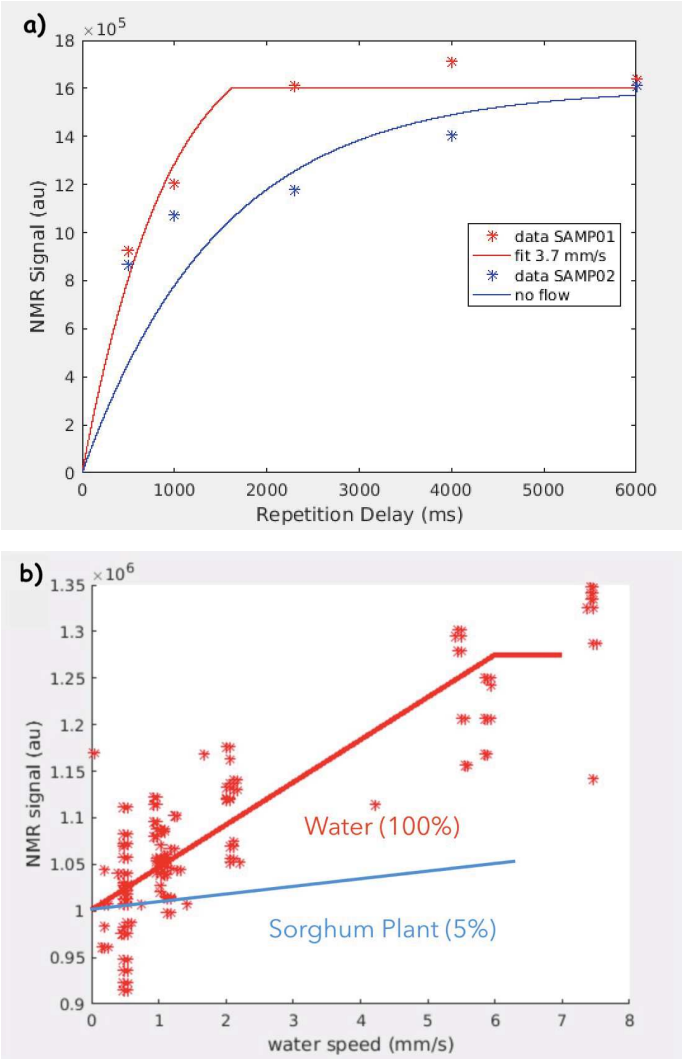

Figure 73 – Investigation of water fluxes in the portable NMR using One pulse sequence (Chameleon pulse sequencer) (a) Evolution of NMR signal as a function of Recovery delay $R_D = 0.5s, 1s, 2.3s, 4s$ and $6s$: red with flow of 3.7 mm/s and blue without flow (b) Red curve : evolution of NMR signal as a function of water speed at fixed $R_D(1s)$ in water pipe ($D = 1cm$) which corresponds to 100% of conductive surface and blue curve : interpolation of the evolution of NMR signal in sorghum plant which corresponds to 5% of conductive surface

Thus, the evolution over time of the NMR signal obtained by our portable NMR is also sensitive to the water speed in water tube for velocities less than 6mm/s. In the perspective to make this experiment in sorghum plant where the conductive surface is 20 times (5%) less than water tube, we calculate the sensitivity of our system by interpolation, see Fig. 73. b. We conclude that your system is not able to discern velocities within a plant with this configuration. The solution is the reduction of the slice thickness. In conclusion, it is necessary to add a gradient system to our portable NMR to access flow measurements in plants [Vans As, 1984 and 1985].

18.4 Water status investigations in sorghum plants

To conduct a comparative study of the impact of stress, we investigated two groups of BM x3 and SSM x3 for which the soil is hermetically sealed to avoid the soil evaporation. The aim is to study the water stress behavior through the parameters: FTSW, photosynthesis activity, NMR and MRI.

During these experiments, we monitor the weight of these 6 plants using connected weight scales that has been interfaced in order to have measurements at each time interval chosen by the user. Thus we can follow the hydric behavior of the plants until the weight stabilizes (FTSW=0).

In parallel, we have also studied the modification of photosynthesis activity of these 6 plants and for that we carried out a punctual measurements at different values of FTSW with a dedicated device (GS3000). Finally, we measure the NMR signal of two different genotypes. These 2 genotypes will be transported two times to the laboratory to make high resolution investigations with MRI : the first time it is at the beginning of the experiment, then a second time after one week (Fig. 75). See the MRI results presented in the section before (0.17).

Water irrigation of plants for the two genotypes was stopped at the beginning of the experimentation (stage anthesis). From this moment on , the FTSW (chosen to reflect the soil water constraint) decreased differently according to the genotype (Fig. 75). Indeed, there are strong differences in the pace at which plants of the two anatomically contrasted genotypes deplete their available water.

The FTSW measurement on these groups shown in Fig. 75 .a & .b confirms that the BM and SSM have a different feeling of water stress. Indeed, for the BM plant group, we can divide its FTSW decay curves in three stages: 1) a sharp decrease in the FTSW during the the first two days (it loses 50% of its transpirable soil water fraction after 2 days) 2) a slower FTSW decrease between day 2 and day 6 (decrease from 0.2 to 0.05) 3) a stabilization beyond 6 days after stopping the irrigation at values close to 0.

Regarding the FTSW decay curves of the SSM genotype plants, we can distinguish 4 phases: 1) a rapid decrease during the first two days (30% losses of FTSW in two during this phase) 2) a much slower decrease (decrease of 0.7 to 0.5 between day 2 and day 5) then 3) a faster decrease between day 6 and day 11 and finally 4) a stabilization at values close to 0 between day 12 and day 15 after stopping the irrigation.

The Fig. 75 .a & .b represents also the NMR measurements for BM and SSM genotypes, respectively. We observed in both cases, some decays of the NMR signal intensities after a water stress.

Concerning the NMR measurement on BM genotype, the decay goes through 3 different

phases also (1) a sharp decay in the NMR signal during the the first two days (40%) (2) a slower decay between day 2 and day 10 (40% to 10%) (3) a stabilization beyond 10 days after stopping the irrigation at values about 0.

For the SSM genotype, the decay goes through 4 different phases also (1) sharp decay in the NMR signal during the first two days (50%) (2) a stabilization of the NMR signal between day 2 and day 8 (40%) (3) a slower decay between day 2 and day 10 (40% to 10%) (4) finally after 15 days stopping the irrigation at values close to 0.

The Table. 10 represents the evolution of the parameters : E, GH2O, A_s, ci and water use efficiency WUE according the FTSW. The photosynthetic activity decreases in both genotypes as a function of water stress. Now, if we compare for the same value of FTSW the values of ci (concentration of intercellular CO2) it is noted that the latter is much higher for the genotype BM plant than for the plant of genotype SSM (respectively 114.1 against for FTSW=108.78 for example). All indications are that the uptake of CO2 by PEPc for this level of stress (FTSW=0.2) is less in BM genotype than in the SSM genotype.

We calculated also the intrinsic Water Use Efficiency (WUE) (ratio between the net assimilation A_s and the stomatal conductance GH2O). The values obtained are respectively 0.18 for the BM genotype and 0.17 for the SSM genotype. Thus, although we have observed differences in transpiration behavior between the two genotypes, they did not seem to be accompanied by differences in water efficiency, as has been observed in other plants such as grapevine [Lovisolo, 2010].

Figure 74 – GFS300 device that allowed the measurement of gas exchange in sorghum leaves

18.5 Daily evolution of NMR signal at different FTSW

Now we will focus on the behavior within 24 hours at different FTSW stages and investigate how the NMR signal varies during day/night.

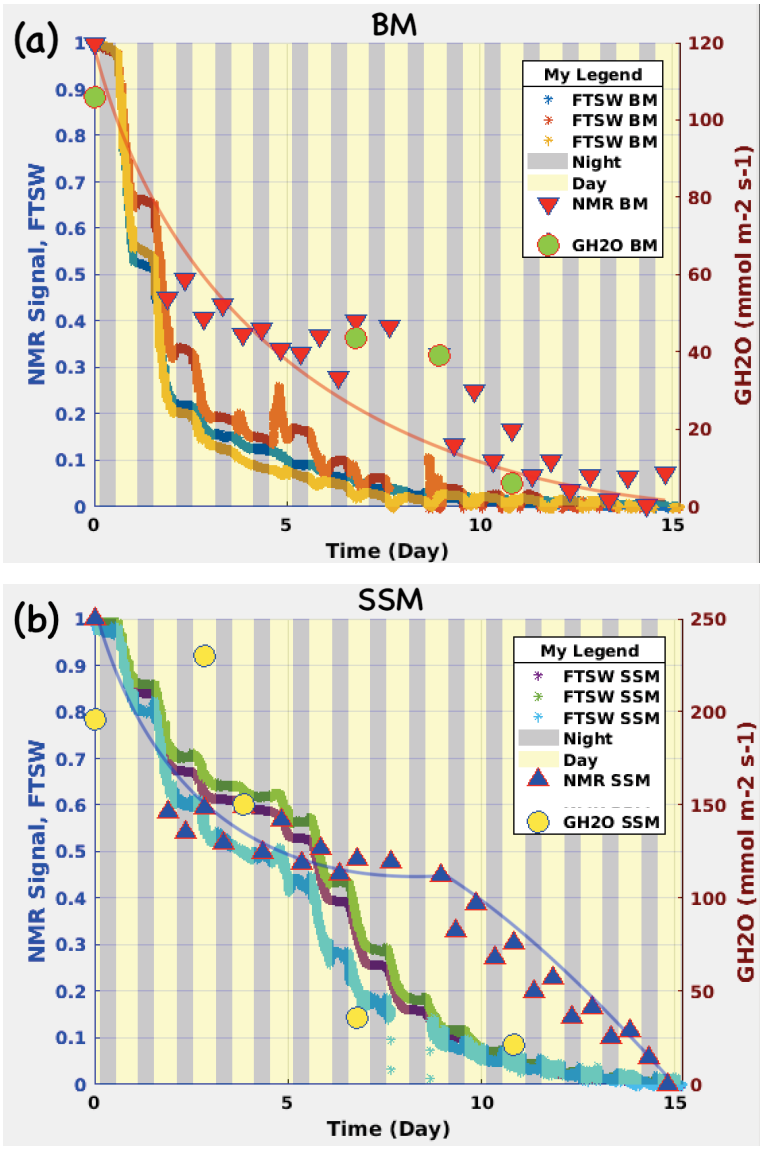

Figure 75 – Monitoring of the NMR signal and comparative evolution of Fraction of Transpirable Soil Water (FTSW) during water stress in two groups of anatomically contrasted genotypes of sorghum : (a) BM and (b) SSM. Each line reflects the evolution of the FTSW value of one plant, the triangles correspond to the measurement of the NMR signal of a plant (Red for the BM genotype (a) Blue for the SSM genotype (b)). The circles correspond to the punctual measurements of the photosynthetic activity with GFS-3000 device

The Fig. 76 show the evolution of NMR signal in BM genotype :

- For a value of FTSW=0.6 : during this stage, the NMR signal varies by more than 50% during the day but the night remains stable.
- For a value of FTSW=0.2 : during this stage, the NMR signal varies by more than 30% during the day but the night remains stable.
- For a value of FTSW=0: during this stage, the NMR remains stable during the day and night.

Genotype	FTSW	$E(mmolm^{-2}s^{-1})$	$GH2O(mmolm^{-2}s^{-1})$	$A_s(\mu molm^{-2}s^{-1})$	$WUE(mmol)$	$ci(ppm)$
BM	1	2.65 ± 0.28	105.84 ± 17.63	19.24 ± 2.37	0.18	86.35 ± 10.44
	0.2	0.74	43.53	8.05	0.18	114.18
SSM	1	4.10 ± 0.65	196.36 ± 47.93	31.25 ± 7.81	0.15	111.83 ± 34.31
	0.2	0.62	21.59	3.82	0.17	108.78

Table 10 – Measurement of photosynthetic activity of Biomass genotype and SSM genotype using GFS 3000 at leaf level. The photosynthetic activity decreases in both genotypes as a function of water stress

The Fig. 77 show the evolution of NMR signal in SSM genotype :

- For a value of FTSW=0.8 : during this stage, the NMR signal varies by more than 35% during the day but the night remains stable.
- For a value of FTSW=0.5 : during this stage, the NMR remains stable during the day and night.
- For a value of FTSW=0.3 : during this stage, the NMR signal varies by more than 30% during the day but the night it remains stable.
- For a value of FTSW=0 : during this stage, the NMR signal remains stable during the day and night.

These results obtained in two genotypes investigations show that :

- The NMR signal varies during the day but remains stable throughout the night.
- These variations during the day are manifested when the plant uses water for its vegetative needs.
- These observed variations are perfectly correlated with the variations observed in the FTSW.

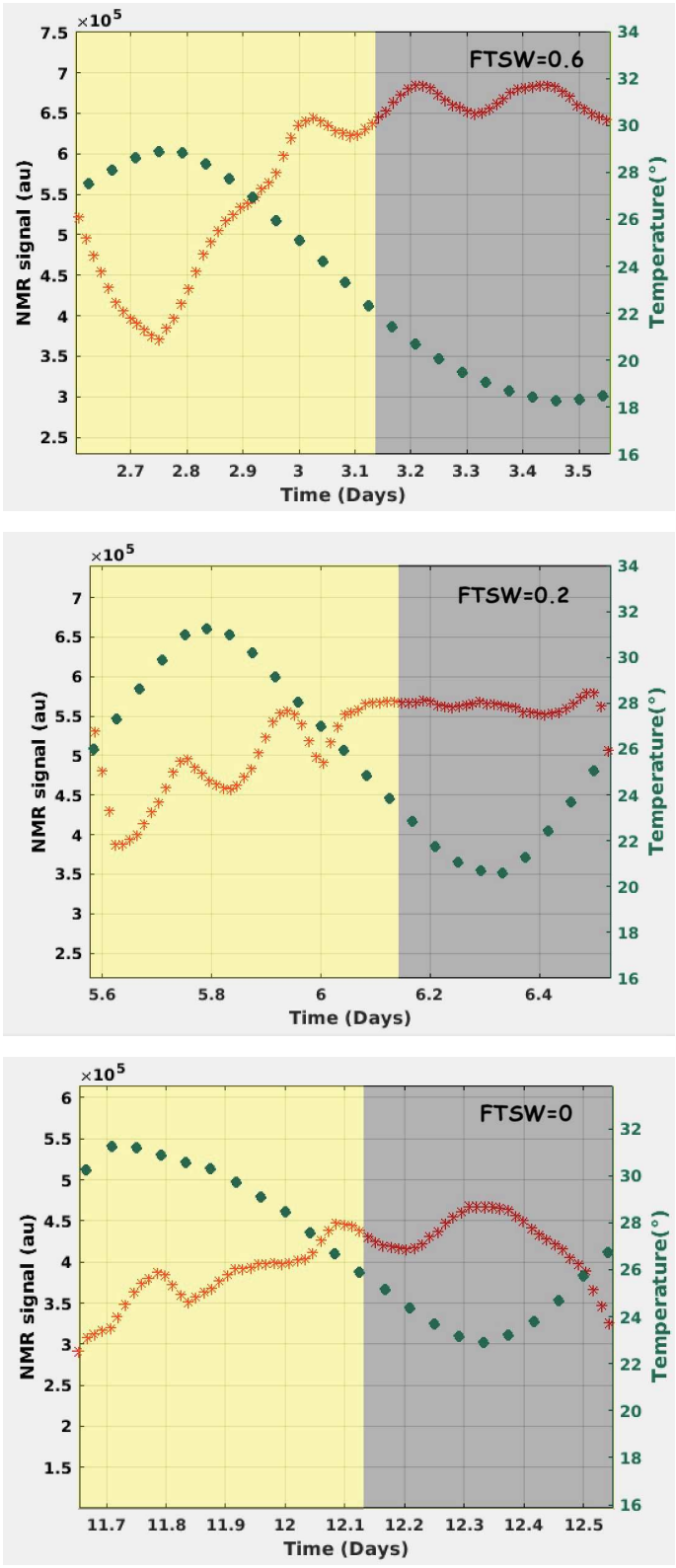

Figure 76 – Behavior of NMR Signal of BM during 24 hours on 3 FTSW stages : 0.6, 0.2 and 0 ($R_D = 1s, P_w = 375us$, acquisition time=$18mn$ at $336kHz$)

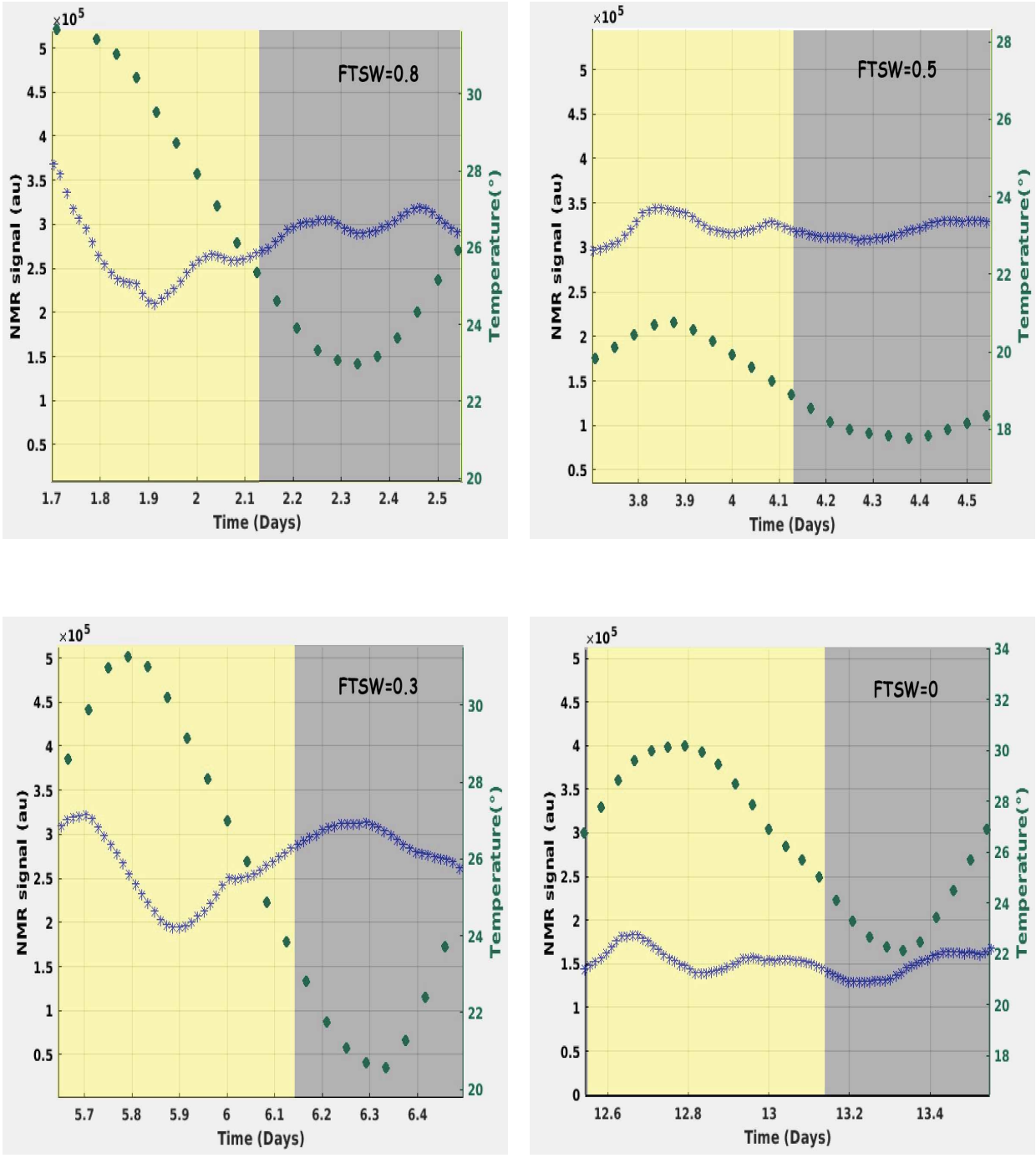

Figure 77 – Behavior of NMR Signal of BM during 24 hours on 4 FTSW stages : 0.8, 0.5, 0.3 and 0 ($R_D = 1s, P_w = 375us$, acquisition time=$18mn$ at $336kHz$)

19 Discussion

19.1 Evolution of NMR/ MRI properties in different tissues under watered conditions

The NMR / MRI results revealed the presence of two NMR components in sorghum plant: a long one related to the conductive bundles and the parenchymal tissues of the Type B filled with water and a short one related to the subepidermal sclerenchyma and epidermis.

The difference between the two genotypes studied is that : in BM genotype, the long component is partially bound to parenchymal tissues and bridges that contain Type B cells. In SSM genotype, the long component is linked a lot to parenchymal tissues because there is a strong presence of Type B tissues.

Regarding the Type R cells, they give no signal because they are surely filled with matter very poor in water content according to the MRI.

19.2 Water status biomarkers from the evolution of NMR/ MRI properties in different tissues under water stress

Under water stress it is the long component that is likely more affected :

Indeed in the BM genotype, with a "heterogeneous distribution of Type B cells", loses more than half of the water content contained in these cells and the bridges have completely disappeared. This suggests that these cells were a sources of water supply and that these bridges served as a radial supply between the vascular bundles.

The BM loses the half of its weight after two days and arrives at its wilting weight after 7 days. From the MRI it is clear that after 7 days the vascular bundles give no signal and therefore no more transport. This behavior correlates perfectly with the measurement achieved with the portable NMR and suggests that no evidence of resistance or tolerance under stress for this genotype and after one week the vascular vessels show some signs of embolism.

In the SSM genotype, with a "homogenous distribution of Type B cells", it also loses about half of its initial water content but its Type B cells do not disappear and the vascular vessels are functional. This suggests that the water in these cells is used in a moderate way and that the proportion of these cells may need to be re-examined after several weeks (in our case, we perform MRI experiments after 1 week only).

The SSM loses 40% of its weight after 3 days then stagnates for a few days and then loses again after one week and finally reaches its wilt weight after 15 days. This behavior also corresponds perfectly to the measurement carried out with the portable NMR and suggests that, unlike to the BM genotype, the SSM shows signs of perception of stress then a resistance

during few days before yielding when the stress becomes too important.

These results obtained by monitoring the water status with NMR revealed stress biomarkers and the possibility to clearly identify the behavior of two different genotypes under water stress.

19.3 Water fluxes biomarkers

To better distinguish the two genotypes BM and SSM and thanks to the method of flip flop in terms of transport, we were able to determine a mobility effect ensured by MRI by Xylem bundles.

MRI experiment shown that during the day there is a strong mobility in the xylemian bundles due to sap transport. We revealed also that the BM and the SSM transport at the same speed this xylemian sap but in the SSM there is less conductive bundles used. This result shows once again that the SSM needs less resources to survive and that it regulates its water supply according to the conditions that surround it. These results in SSM also coincide with the behavior of weight loss and changes in the NMR signal during the water stress in the greenhouse.

In fact, the large changes obtained in both cases with the NMR signal during the day correspond to the great mobility of the xylemian sap. Indeed, we know that the mechanism of absorption of water by plants is transpiration, which is regulated by stomata that open during the day and close at night. When the vascular bundles are no longer functional, there are no more changes. This change in NMR signal may be interpreted in term of T_1 effect combined with a inflow effect in the coil due to the moving spins.

Our results obtained show that the BM uses all of its means of transport until exhaustion of available water resources without any resistance. The SSM transport system is more strategic and reduces its consumption by reducing the number of conductive bundles during a water stress.

Conclusion and perspectives

Non invasive multi-scale investigations of plants in *naturae* under the effects of global warming and climate change can be studied thanks to the recent improvements of the Nuclear Magnetic Resonance instrumentation and methodology.

My thesis is a contribution to the constant interest of the plant community for this field of research developing the great potential of the NMR and MRI to highlight the physiological and morphological properties associated with the water content and transport in the plants during normal conditions and under water stress.

The choice to study sorghum was justified by its economical impact, its biodiversity and the fact that it represents a plant model in the study of water stress thanks to its resistance to drought.

In a first step, our approach consisted in developing the low field methodology based on a resistive NMR system implemented in a climatic chamber at the laboratory. This allowed us to develop the protocols (sequences and processing of the NMR information) during the dynamic diurnal cycle in normal and abiotic stress conditions as well as to guide our choice of the instrumental development for the low magnetic field device.

In a second step, we developed the key elements (magnet and transmitter/receiver amplifiers) of a complete NMR portable system dedicated to the plants.

Based on space harmonics suppression (SHS) method and thermal modelisation, we proposed an extended version for manufacturing a resistive magnet showing sufficient magnetic field homogeneity and overheating which keeps plant integrity. High signal to noise ratio was achieved by developing some innovative electronic device.

With the help of these apparatus, we investigated two genotypes of sorghum duly chosen according to their differences : Biomass 140 and SSM 1267 using histology, MRI in the laboratory and low field NMR in the greenhouses and in the fields concerning.

The histology experiments illustrated a significant differences in the thickness, the architecture and the distribution of cells (Type R and B) that constituted the parenchyma of these two genotypes.

The MRI experiments and especially the flip flop method allowed us to identify the con-

ductive bundles but also to quantify for the first time the speed with which these bundles transport the sap in sorghum plant, in agreement with the behavior expected in these two genotypes.

In conclusion, we demonstrated that our homemade portable NMR is sensitive to water content and its variation during diurnal cycles and stress and opens a way to study the plant in fields condition.

Perspectives Today, our portable NMR permits quantitative and qualitative measurements of water statut in plants.

In the future, additional magnetic field gradients could permit a more precise determination of water fluxes, which can provide more information on water management in a non invasive way and in the fields (see Fig. 78).

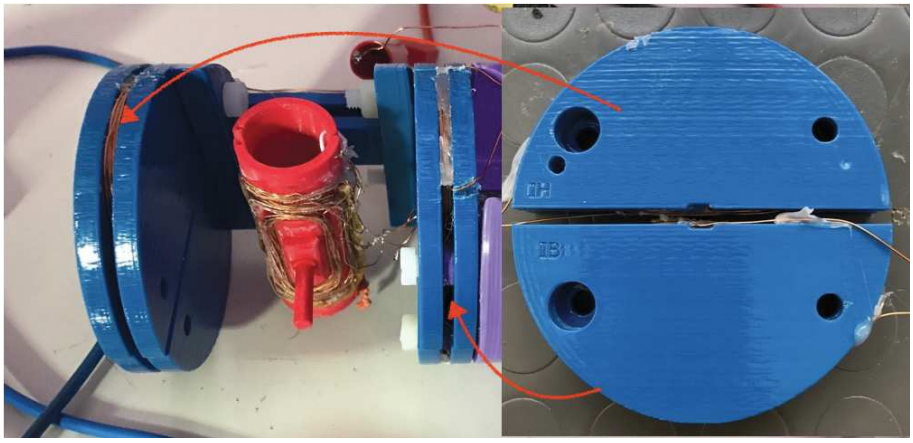

Figure 78 – Magnetic field gradients design based on Golay coil : $G_s = 29uT/mm, N_n = 30$ x $4, R = 42mm$ and $r_c = 0.25mm$.

The high resolution MRI experiments were conducted in a horizontal 9.4T MRI system. It would be interesting to consider the same approach on these two very contrasted genotypes in a vertical MRI system with a suited climatic chamber, in order to study the contributions of xylem bundles and the flow velocity under water stress for these two genotypes.

Finally concerning the portable NMR system dedicated to measurements where plants are not available, some efforts have to be made on the energy autonomy by looking at alternative sources of energy like solar or hydraulic.

Acknowledgements This work has been carried out thanks to the support of the LabEx NUMEV project (no. ANR-10-LABX-20) funded by the "Investissements d'Avenir" French Government program, managed by the French National Research Agency (ANR), CIRAD, AGROPOLIS and INRA.

Annex 1 : Bloch equations

In 1946 Felix Bloch formulated a set of equations that describe the behavior of the magnetization of nuclear spin in a magnetic field B_0 after the application of RF magnetic field B_1. Bloch assumed that the spins relax along the z-axis and in the x-y plane at different rates R but following first order kinetics according [Robert, 1970]:

$$\frac{dM}{dt} = \gamma M(t) \wedge B - R(M(t) - M_0) \tag{79}$$

These rates (R) are designated as 1/T1 and 1/T2 for the z-axis and x-y plane, respectively. According to the Eq.(79) we can express deduce :

$$\frac{dM_z}{dt} = \gamma(M_x B_y - M_y B_x) + \frac{dM_z - M_0}{T_1} \tag{80}$$

$$\frac{dM_x}{dt} = \gamma(M_y B_z - M_z B_y) - \frac{dM_x}{T_2} \tag{81}$$

$$\frac{dM_y}{dt} = \gamma(M_z B_x - M_x B_z) - \frac{dM_y}{T_2} \tag{82}$$

In fact, Eq.(80), (81) and (82) describes the motion of magnetization of stationnary system in the laboratory referential while we know that this magnetization is rotate at a speed ω_0 in xy plan. Now, by reporting these equations in rotate referential ($B_z = B_0$, $B_x = B_1 cos(\phi)$ and $B_y = B_1 sin(\phi)$ are the RF magnetic field) we find:

$$\frac{dM_z}{dt} = \gamma(M_x B_y - M_y B_x) + \frac{dM_z - M_0}{T_1} \tag{83}$$

$$\frac{dM_x}{dt} = -\omega_0 M_y - \gamma M_z B_y - \frac{dM_x}{T_2} \tag{84}$$

$$\frac{dM_y}{dt} = \gamma(M_z B_x) + \omega_0 M_x - \frac{dM_y}{T_2} \tag{85}$$

If we will apply the RF pulse along the x-axis, we neglige the terms that contain T_1, T_2, B_y, ω_0 :

$$\frac{dM_z}{dt} = -\gamma M_y B_x \tag{86}$$

$$\frac{dM_x}{dt} = 0 \tag{87}$$

$$\frac{dM_y}{dt} = \gamma M_z B_x \tag{88}$$

During the NMR experiment, we can choose which direction we can apply our magnetic field during the pulse. If we introduce a frequency of rotation about the x-axis $\omega_1 = \gamma B_x$, the solution of Eq.(86), (87) and (88) :

$$M_z = M_0 cos(\omega_1 t) \tag{89}$$

$$M_x = 0 \tag{90}$$

$$M_y = M_0 sin(\omega_1 t) \tag{91}$$

In the absence of any magnetization applied in the x-y plane, the change in the magnetization is due to relaxation effects "free precession" of T1 and T2 processes, B_x and B_y are both equal to zero and the solution of Eq.(83), (84) and (85) become:

$$\frac{dM_z}{dt} = -\frac{dM_z - M_0}{T_1} \tag{92}$$

$$\frac{dM_x}{dt} = -\omega_0 M_y \frac{dM_x}{T_2} \tag{93}$$

$$\frac{dM_y}{dt} = \gamma(M_z B_x) + \frac{dM_y}{T_2} \tag{94}$$

The general solution of these last set of equations :

$$M_z = M_0(1 - e^{(-t/T_1)}) \tag{95}$$

$$M_x = M_0 cos(\omega_0 t)(1 - e^{(-t/T_2)}) \tag{96}$$

$$M_y = M_0 sin(\omega_0 t)(1 - e^{(-t/T_2)}) \tag{97}$$

Annex 2 : Gradients used in NMR imagery

The MR images are generated by means of the sequential application of three gradients : G_s, G_r and G_p to spatially encode the contributions of volume elements (voxels).

- **Gradient of slice selection G_s :** in NMR imaging, the first gradient applied is the gradient of selection by frequency along the z axis for example. This gradient is applied at the same time as the RF selective pulse with a spectral width δf around the central position ($z = 0$), see Fig. 79 :

$$\delta f = 2\pi\gamma G_s \Delta z \tag{98}$$

  where Δz is the slice thickness where the spins are selected.

  The Eq. (98) shows that one can act on the thickness of the slice either by increasing the intensity of the gradient G_s. The slice position can be modified by acting on the frequency of selection.

- **Gradient of frequency encoding G_r:**

  After the application of G_s, we apply another gradient G_r, this time in the x-y plane, to code first the x or read axis by "frequency ω". As we said before, the gradient makes it possible to correlate the frequency and spatial position, which is commonly called in MRI technique space k or Fourrier space. In fact, the first dimension k_r of this space is the positions of spins along the x-axis point by point n at regular intervals t_x(sampling) : $k_r = \gamma n G_r \Delta t_x$.

  This gradient is applied in same time than the acquisition of the entire signal from slice by the MR system (see Fig. 79).

- **Gradient of phase encoding G_p :**

  The phase gradient makes it possible to fill the second dimension of Fourrier space k_p. At the end of this gradient, the magnetization of each voxel returns to its equilibrium

according B_0 but keeps the information "phase ϕ" and allows to fill k-space line by line. Note that, this gradient is applied just before the acquisition of the signal and its amplitude is incremented n times: $k_p = \gamma n G_p \Delta t_y$ (see Fig. 79).

We conclude that, by using these coding gradients by the frequency G_r and by the phase G_p, we have located each magnetization in the selected slice with a double components (ω and ϕ). This pair is also written as a function that depends on the x and y positions in the space.

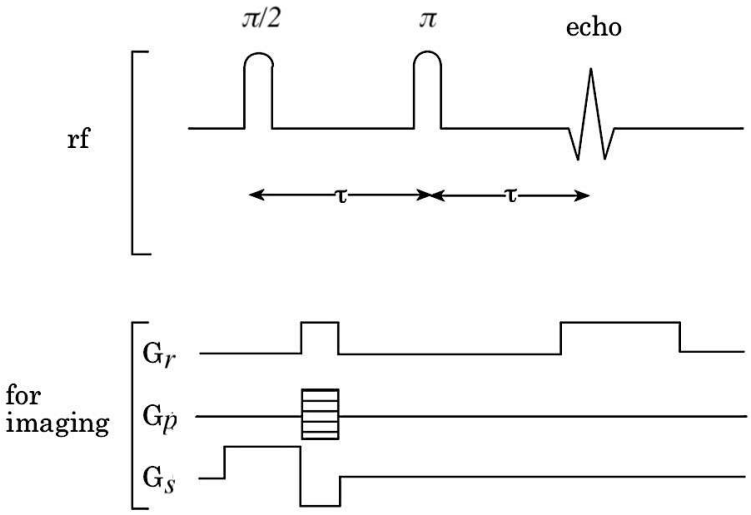

Figure 79 – Illustration of pulse sequence of a spin echo imaging technique (TF 2D): Radio frequency (RF) pulse sequence for spin-echo measurement. τ is the interval between $\pi/2$ (excitation) and π (refocus) RF pulses. Magnetic field gradient sequence for imaging is shown then : G_r, G_p and G_s indicate magnetic field gradients for imaging in x,y and z, respectively. Modified from [Ishida, 1989]

The total signal in k-space after the application of the three gradients can be written as :

$$S(k_r, k_p) = \int \int \rho_s(x, y) e(-j(k_r x + k_p y)) dx dy \tag{99}$$

Where ρ_s is the image in real space:

$$\rho_s(x, y) = \int \int S(k_r, k_p) e(-j(k_r x + k_p y)) dk_r dk_p \tag{100}$$

Finally, the distribution of the proton density is obtained by the application of two-dimensional Fourier Transform (TF 2D)

The spatial resolution in x-y plan can be written:

$$\Delta r = \frac{2\pi}{\gamma G_r t_{acq}} \tag{101}$$

$$\Delta p = \frac{2\pi}{\gamma G_{pmax}} \tag{102}$$

Where t_{acq} is the acquisition time of one line of n sample and G_{pmax} is the max value of the intensity of phase encoding gradient. The setting of these two parameters is essential to define the spatiale resolution and the total acquisition time.

Annex 3: TxRx amplifier circuit

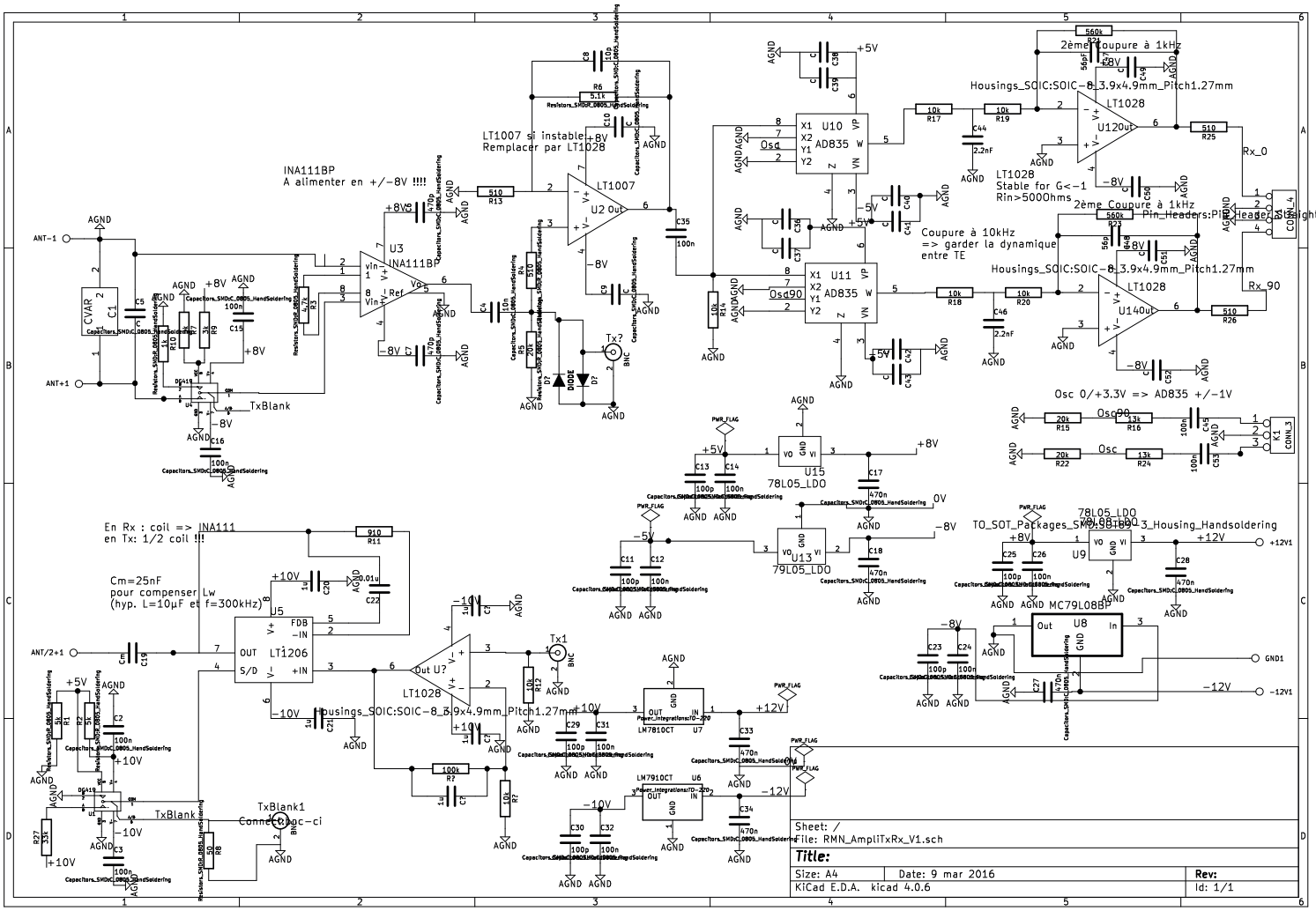

Bibliography

[Asfour, 2011] Asfour A., Low-Field NMR/MRI Systems Using LabVIEW and Advanced Data-Acquisition Techniques, InTech, ISBN: 978- 953-307-650-8, (2011).

[Barrs, 1965] Barrs H.D., Psychrometric measurement of leaf water potential: lack of error attributable to leaf permeability, Science 149, 63-65. http://dx.doi.org/10.1126/science.149.3679.63 PMid:17737791, (1965).

[Begue, 1992] Bégué A., Hanan N.P., Prince S.D., Modélisation de la conductance stomatique de couverts végétaux sahéliens, jourrnées hydrologiques - Orstom, (1995).

[Belevitch, 1971] Belevitch V., The lateral skin effect in a flat conductor, Philips tech Rev., 32, 221-231, (1971).

[Ben Rejeb, 2014] Ben Rejeb I., Pastor V. and Mauch-Man B., Plant Responses to Simultaneous Biotic and Abiotic Stress: Molecular Mechanisms, Plants 3(4), 458-475. http://doi.org/10.3390/plants3040458, (2014).

[Bernstein, 2005] Bernstein M.A., King K.F. and Zhou X.J., Handbook of MRI pulse sequences, Elsevier Academic Press, (2005).

[Bloch, 1946] Bloch F., Hansen W.W. and Packard M., The Nuclear Induction Experiment, Phys. Rev., 70, 474, (1946).

[Blumich, 2011] Blumich B., Casanova F., Dabrowski M., Danieli E., Evertz L., Haber A., Van Landeghem M., Haber-Pohlmeier S., Olaru A., Perlo J., Sucre O., Small-scale instrumentation for nuclear magnetic resonance of porous media, New J Phys., (2011).

[Braun, 1996] Braun S.,Kalinowski, Berger S., 100 and more Basic NMR experiments., VCH, ISBN: 3-527-29091-5, (1996).

[Breitenstein, 2011] Breitenstein B., Scheller M., Shakfa M.K., Kinder T., Muller-Wirts T., Koch M. and Selmar D., Introducing terahertz technology into plant biology: A novel method to monitor changes in leaf water status, Journal of Applied Botany and Food Quality 84, 158 - 161, (2011).

[Bolinger, 1988] Bolinger, L., Prammer, M. G., and Leigh, J. S., A Multiple- Frequency Coil with a Highly Uniform B1 Field, J. Magn. Reson., 81, 162-166, 1988.

[Bottomley, 1984] Bottomley P.A., Foster T.H., Argersinger R.E., Pfeifer L.M., A review of normal tissue hydrogen relaxation times and relaxation mechanisms from 1-100 MHz : dependence on tissue type, NMR frequency, temperature, species, excision, and age, Med Phys 11:425-448, (1984).

[Boyer, 1967] Boyer J. S., Leaf Water Potentials Measured with a Pressure Chamber. Plant Physiology, 42(1), 133-137, (1967).

[Bunce, 2001] Bunce J. A., Direct and acclimatory responses of stomatal conductance to elevated carbon dioxide in four herbaceous crop species in the field, Global Change Biology 7, 323-331, (2001).

[Buy, 2018] Buy S., Le Floch S., TANG N., Sidiboulenouar R., Zanca M., Canadas P., Nativel E., Cardoso M., Alibert E., Dupont G., Ambard D., Maurel C., Verdeil J.-L., Bertin N., Goze-Bac C., Coillot C., Flip-flop method: A new T1-weighted flow-MRI for plants studies. Plos One, 13 (3). , DOI : 10.1371/journal.pone.0194845, (2018).

[Bydder, 2007] Bydder M., Rahal A., Fullerton G.D., Bydder G.M., The Magic Angle Effect: A Source of Artifact, Determinant of Image Contrast, and Technique for Imaging, Journal of Mag. Res. Imag., 25:290-300, (2007).

[Callaghan, 1991] Callaghan P.T., Principles of Nuclear Magnetic Resonance Microscopy, Clarendon Press, Oxford (1991).

[Chantereau, 2013] Chantereau J., Cruz J-F., Ratnadass A., Trouche G., Le sorgho., Quae, ISBN: 978-275-922-061-8, (2013).

[Chaves, 2003] Chaves Manuela M. , Maroco J.P., Pereira J.S., Understanding plant responses to drought - from genes to the whole plant. Functional Plant Biology, https://doi.org/10.1071/FP02076, (2003).

[Clarck, 1938] Clark, J. W.: A new method for obtaining a uniform magnetic field, Rev. Sci. Instrum., 9, 320?322, (1938).

[Coillot, 2016a] Coillot C., Sidiboulenouar R., Nativel E., Zanca M., Alibert E., Cardoso M., Saintmartin G., Noristani H., Lonjon N., Lecorre M., Perrin F. and Goze-Bac C., Signal modeling of an MRI ribbon solenoid coil dedicated to spinal cord injury investigations, J. Sens. Sens. Syst., 5, pp. 137–145, (2016).

[Coillot, 2016b] Coillot, C., Nativel, E., Zanca, M., and Goze-Bac, C.: The magnetic field homogeneity of coils by means of the space harmonics suppression of the current density distribution, J. Sens. Sens. Syst., 5, 401?408, https://doi.org/10.5194/jsss-5-401-2016, (2016).

[Coillot, 2018] Coillot, C., Sondes pour l'IRM, (2018).

[Cole, 2015] Cole J., Pagay V., Usefulness of early morning stem water potential as a sensitive indicator of water status of deficit-irrigated grapevines, Scientia Horticulturae ,191 10?14 , http://dx.doi.org/10.1016/j.scienta.2015.04.034, (2015).

[Coupe, 2016] Coupe M., Touraine B., Physiologie vegetale., Ellipses, ISBN: 978-234-001-409-1, (2016).

[Cramer, 2011] Cramer GR., Urano K., Delrot S., Pezzotti M. et Shinozaki K., Effects of abiotic stress on plants: a systems biology perspective. BMC Plant Biology., 11:163. doi:10.1186/1471-2229-11-163, (2011).

[Damadian, 1971] Damadian R., Tumor detection by nuclear magnetic resonance, Science, 171: 1151, (1971).

[Daudet, 2005] Daudet F.A., Ameglio T., Cochard H., Archilla O. et Lacointe A. Experimental analysis of the role of water and carbon in tree stem diameter variations. J. Exp. Bot, 56:135?144, (2005).

[De Graaf, 2006] De Graaf R.A., Brown P.B., McIntyre S., Nixon T.W., Behar K.L., et Rothman D.L., High magnetic field water and metabolite proton T1 and T2 relaxation in rat brain in vivo. Magn Reson Med., 56:386-394, (2006).

[Dixon, 1894] Dixon H.H and Joly J., On the Ascent of Sap., Proceedings of the Royal Society of London. 57:3-5,(1894).

[Duval, 2004] Duval F.P., Cambert M. and Mariette F., NMR study of tomato pericarp tissus by spin- spin relaxation and water self-diffusion. Applied Magnetic Resonance. 28-29, (2004).

[Ernst, 1966] Ernst R.R., Anderson W.A., Application of Fourier transform spectroscopy to magnetic resonance. Rev Sci Instrum , 37:93-102, (1966).

[Emmerik, 2017] Emmerik T.V., Steele-Dunne S.C., Judge J. and Giesen N.V., Dielectric Response of Corn Leaves to Water Stress, IEEE Geoscience and Remote Sensing Letters, VOL. 14, NO. 1, (2017).

[Everett, 1966] Everett, J. E. and Osemeikhian, J. E.: Spherical coils for uniform magnetic fields, J. Sci. Instrum., 43, 470?474, (1966).

[Fay, 1995] Fay P. A., and Knapp A. K., Stomatal and photosynthetic responses to shade in sorghum, soybean and eastern gamagrass, Physiol, Plant, 94: 613-62, (1995).

[Floch, 1990] Fuchs M., Infrared measurement of canopy temperature and detection of plant water stress, Theoretical and Applied Climatology, doi :10.1007/BF00865986, (1990).

[Gente, 2016] Gente R., Born N., Balzer B.C. and Koch M., Assessment of plants' reaction to drought stress using THz time domain spectroscopy, 41st International Conference on Infrared, Millimeter and Terahertz waves (IRMMW-THz), doi: 10.1109/IRMMW-THz.2016.7758370, (2016).

[GIEC, 2014] Groupe d'experts Intergouvernemental sur l'Evolution du Climat (GIEC)., Changements climatiques 2014 rapport de synthese., P. 4-6, (2014).

[Ginefri, 2001 and 2005] Ginefri J-C., Poirier-Quinot M., Robert P., , Darrasse L. Contrast-enhanced dynamic MRI protocol with improved spatial and time resolution for in vivo microimaging of the mouse with a 1.5 T body scanner and a superconducting surface coil. Magnetic Resonance Imaging, vol. 23 : 239-243, (2005).

[Ginefri, 2001 and 2005] Ginefri J-C., Darrasse L., Crozat P., A High-Temperature Superconducting surface coil for In Vivo micro imaging of the human skin, Magnetic resonance in medicine, vol. 45 : 376-382, (2001).

[Hadjiloucas, 1999] Hadjiloucas S., Karatzas L.S. and Bowen J.W., Measurements of Leaf Water Content Using Terahertz Radiation, IEEE Transactions on Microwave Theory and Techniques, Vol. 47, No. 2, (1999).

[Hamburger, 1937] Hamburger E., Contribution à l'étude des pertes par courants de Foucault dans les bobines cylindriques à une ou plusieurs couches, PhD thesis, Ecole d'ingénieurs de l'université de LAUSANNE, (1937).

[Haignere, 1976] Haignere E.B., Potter W.M., Optimizing the shape and size of a uniform-current-density magnet to maximize the field at constant power, J. Appl. Phys., 47 1657?1661, (1976).

[Halbach, 1980] Halbach K., Design of permanent multipole magnets with oriented rare earth cobalt material, Nucl. Instrum. Methods, vol. 169, no. 1, pp. 1-10, (1980).

[Herlach, 2002] Herlach F., Laboratory electromagnets?from oersted to megagauss, Physica B 319, 321?329, (2002).

[Harpen, 1991] Harpen M.D., The Spherical Birdcage Resonator, Journal of Magnetic Resonance., Vol. 94, pp. 550–556, (1991).

[Hayes, 1985] Hayes C. E., Edeutein W. A., Schenck J.F., Mueller O. M. and Eash M., An Efficient Highly Homogeneous Radiofrequency Coil for Whole-Body NMR Imaging at 1.5T., Journal of Magnetic Resonance, Vol. 63, pp. 622-628, (1985).

[Hu, 1995] Hu B.B. and Nuss M.C., Imaging with terahertz waves, Opt. Lett. 20, 1716-1718 (1995).

[Hudson, 2011] Hudson P., Pushing the Boundaries in Gradient and Shim Design for MRI, thesis, University of western Ontorio, (2011).

[Hugon, 2010] Hugon C., Aimants permanents pour la RMN et l'IRM, These doctorat, Universite de Versailles Saint-Quentin-en-Yvelines, (2010).

[Hoult, 1976] Hoult D.I., Richards R.E., The signal-to-noise ratio of the nuclear magnetic resonance experiment., J Magn Reson, Vol. 24,pp. 71–85, (1976).

[Hoult, 1990] Hoult D.I., Deslauriers, A High-Sensitivity and High B_1 Homogeneity Probe for Quantitation of Metabolites., Magnetic Resonance in Medicine, Vol. 16,pp. 411–417, (1990).

[Incorpera, 1990] Incropera F.P. and De Witt D.P., Introduction to Heat Transfer, Second Edition, John Wiley & Sons, New York, NY, (1990).

[Ishida, 1989] Ishida N., Kobayashi T., Koizumi M. and Kano H., NMR Imaging of Tomato Fruits, Agric. Biol. Chem., 53, 9, 2363-2367, (1989).

[Jones, 1998] Jones H.G., Tardieu F., Modelling water relations of horticultural crops: a review, Scientia Horticulturae,74 21-46, (1998).

[Jones, 2004] Jones H.G., Application of thermal imaging and infrared sensing in plant physiology and ecophysiology. Adv. Bot. Res., 41, 107-163, (2004).

[Jones, 2012] Jones M., Aptaker P.S., Cox J., Gardiner B.A., McDonald P.J., A transportable magnetic resonance imaging system for in situ measurements of living trees: the tree hugger, J. Magn. Reson., 218:133-40, (2012).

[Kehr, 2007] Kehr J. and Buhtz A., Long distance transport and movement of RNA throught the phloem. Journal of Experimental Botany. 59(1):85-92., (2007).

[Kennouche, 2014] Kennouche S., Etudes experimentales et modelisation de la dynamique de distribution des agents de contraste en imagerie RMN: applications a l'agronomie, These doctorat, Universite des sciences de Montpellier, (2014).

[Kimura, 2011] Kimura T., Geya Y., Terada Y., Kose K., Haishi T., Gemma H., Sekozawa Y., Development of a mobile magnetic resonance imaging system for outdoor tree measurements, Rev. Sci. Instrum., 82:053704, (2011).

[Kotchi, 2004] Kotchi S. O., Détection du stress hydrique par thermographie infrarouge: Application à la culture de la pomme de terre. Maitrise en sciences, Université Québec, Canada, (2004).

[Kregel, 2002] Kregel K., Heat shock proteins: modifying factors in physiological stress responses and acquired thermotolerance, J. Appl. Physiol., 92: 2177-218-6, (2002).

[Köckenberger, 1997] Köckenberger W., Pope J.M., Xia Y., Jeffrey K.R., Komor E. and Callaghan P.T., A non- invasive measurement of phloemand xylem water flow in castor bean seedlings by nuclear mag- netic resonance microimaging. Planta. 201(1):53-63, (1997).

[Lauterbur, 1973] Lauterbur P.C. Image formation by induced local interactions: examples employing nuclear magnetic resonance. Nature, 242:190-1, (1973).

[Levitt, 2008] Levitt M.H., Spin Dynamics - Basics of Nuclear Magnetic Resonance, Second edition. John Wiley and Sons, Ltd., ISBN: 978-0-470-51117-6, (2008).

[Li, 2010] Li L., Nielsen D.C., Yu Q., Ma L., Ahuja L.R., Evaluating the Crop Water Stress Index and its correlation with latent heat and CO2 fluxes over winter wheat and maize in the North China plain, Agricultural Water Management 97 1146-1155, (2010).

[Lovisolo, 2010] Lovisolo C., Perrone I., Carra A., Ferrandino A., Flexas J., Medrano H., Schubert A., Drought-induced changes in development and function of grapevine (Vitis spp.) organs and in their hydraulic and non-hydraulic interactions at the whole-plant level: a physiological and molecular update, Funct Plant Biol 37:98?116, 2010.

[Mansfield, 1977] Mansfield P., Maudsley A.A., Medical imaging by NMR (First image of human finger), Br J Radiol, 50:188-194., (1977).

[Martinez, 2011] Martinez E.M., Cancela J.J., Cuesta T. S. and Neira X. X., Review. Use of psychrometers in field measurements of plant material: accuracy and handling difficulties, Spanish Journal of Agricultural Research, 9(1), 313-328, (2011).

[Masinde, 2005] Masinde P.W., St utzel H., Agong, S.G., Fricke A., Plant growth, water relations, and transpiration of Spiderplant [Gynandropsis gynandra L. Briq.] under water limited conditions. J. Am. Soc. Hort. Sci. 130, 469-477, (2005).

[Matsushima, 2009] Matsushima U., Herppich W.B., Kardjilov N. , Graf N. , Hilger A., Manke I., Estimation of water flow velocity in small plants using cold neutron imaging with D2O tracer. Nuclear Instruments and Methods in Physics Research Section A: Accelerators, Spectrometers, Detectors and Associated Equipment 605, 146-149, (2009).

[Matsushima, 2009] Matsushima U., Wolfgang Graf W, Kardjilov N., Shono H. and Herppich W.B., Calculation of flow vector in plants by non destructive imaging using neutron radiography, https://www.researchgate.net/publication/40831179, (2009).

[Mispelter, 2006] Mispelter J., Lupu M. and Briguet A., NMR probehads for biophysical and biomedical experiments: theoretical principles and practical guidelines., Imperial College Press, (2006).

[Moradi, 2011] Moradi A.B., Carminati A., Vetterlein D., Vontobel P., Lehmann E., Weller U., Hopmans J.W., Vogel H.J., Oswald S.E., Three-dimensional visualization and quantification of water content in the rhizosphere. New Phytologist 192, 653-663, (2011).

[Monteith and Szeicz, 1962] Monteith J. L. and Szeicz G., Radiative temperature in the heat balance of natural surfaces. Quart. J. R. Meteorol. Soc., 88, 496-507, (1962).

[Musse, 2009a] Musse M., Quellec S., Devaux M.F., Cambert M., Lahaye M. and Mariette F, An investigation of the structural aspects of the tomato fruit by means of quantitative nuclear magnetic resonance imaging, Magnetic Resonance Imaging. 27:709-719, (2009).

[Musse, 2009b] Musse M., Quellec S., Devaux M.F., Cambert M., Lahaye M. and Mariette F. Monitoring the postharvest ripening of tomato fruit using quantitative MRI and NMR relaxometry. Postharvest Biology and Technology. 53:22-35, (2009).

[Musse, 2017] Musse, M., Leport L., Cambert M., Debrandt W., Sorin S., Bouchereau A. and Mariette F., A mobile NMR lab for leaf phenotyping in the field, Plant Methods 13(1): 53, (2017).

[Nabors, 2008] Nabors M., Biologie vegetale. Structures, fonctionnement, ecologie et biotechnologies. Pearson Education. Universite du Mississippi, Oxford, 650 p.,(2008).

[Nagy, 1995] Nagy Z., Tuba Z, Zsoldos F., Erdei L., CO2-Exchange and Water Relation Responses of Sorghum and Maize during Water and Salt Stress, Journal of Plant Physiology, Volume 145, Issue 4, 539-544, (1995).

[Nave, 2006] Nave, C.R., Magnets and electromagnets. HyperPhysics, Department of Physics and Astronomy, Georgia State University. Retrieved May 30, 2012, from http://hyperphysics.phy-astr.gsu.edu/hbase/magnetic/elemag.html, (2006).

[Noristani, 2018] Noristani H.N., Saint-Martin G.P., Cardoso M., Sidiboulenouar R., Catteau M., Coillot C., Goze-Bac C., Perrin F.E., Neurotrauma J., Longitudinal MRI analysis and histological characterization after spinal cord injury in two mouse strains with different functional recovery: gliosis as a key factor, doi: 10.1089/neu.2017.5613, (2018).

[Okada, 2006] Okada F., Handa S., Tomiha S., Ohya K., Kose K., Haishi T., Utsuzawa S., Togashi K., Development of a portable MRI for outdoor measurements of plants., In 6th Colloquium on mobile magnetic resonance, Aachen, Germany, (2006).

[Ortuno, 2010] Ortuno M.F., Conejero W., Moreno F., Moriana A., Intrigliolo D.S., Biel C., Mellisho C.D., Perez-Pastor A., Domingo R., Ruiz-Sanchez M.C., Casadesus J., Bonany J., Torrecillas A., Could trunk diameter sensors be used in woody crops for irrigation scheduling? A review of current knowledge and future perspectives. Agricultural Water Management 97: 1-11, (2010).

[Oosterhuis, 1983] Oosterhuis D.M., Savage M.J., Walter S., Field use of in situ leaf psychrometers for monitoring water potential of a soybean crop. Field Crop Res 7, 237-248, (1983).

[Raich, 2004] Raich H., Blumler P., Design and construction of a dipolar Halbach array with a homogeneous field from identical bar magnets: NMR Mandhalas, Concepts Magn. Reson.,16-25, (2004).

[Robert, 1970] Robert T.S., Introduction to Magnetic resonance, Principles and applications, modern physics monograph series, MassachusettsInstitute of Technology, (1970).

[Robert, 2014] Robert W.B., Norman Cheng Y.C., Haacke E.M., Thompson R.M. and Venkatesan R., Imaging: Physical Principles and Sequence Design, 2nd Edition, ISBN: 978-0-471-72085-0, Wiley-Blackwell, (2014).

[Rokitta, 2000] Rokitta M., Rommel E., Zimmermann U., Haase A., Portable nuclear magnetic resonance imaging system., Rev. Sci. Instrum.,71:4257-62, (2000).

[Romeo and Hoult, 1984] Romeo F., Hoult D.I., Magnet field profiling: analysis and correcting coil design. Magn. Reson. Med., 1(1):44-65, (1984).

[Sakellariou, 2014] Sakellariou D., Hugon C., Guiga A., Aubert G., Cazaux S., and Hardy P., Permanent magnet assembly producing a strong tilted homogeneous magnetic field: towards magic angle field spinning NMR and MRI, Magn. Reson. Chem., vol. 48, no. 12, pp. 903-908, (2010).

[Savage, 2018] Savage A.J., Beecher S.D., Clerx L., Gersony J.T., Knoblauch J., Losada J.M., Jensen K.H., Knoblauch M., and Holbrook N.M., Maintenance of carbohydrate transport in tall trees, nature plants, https://doi.org/10.1038/s41477-017-0064, (2018).

[Scholander, 1965] Scholander P.F., Bradstreet E.D., Hemmingsen E.A., Hammel H.T., Sap Pressure in Vascular Plants, science Vol. 148, Issue 3668, pp. 339-346, (1965).

[Shakhovoy, 2015] Shakhovoy R., Propri ét és structurales et dynamiques des sulfates d'alcalins, th èse doctorat, Universit é d?Orl éans, (2015).

[Suzuki, 2014] Suzuki N., Rivero R.M., Shulaev V., Blumwald E. and Mittler R., Abiotic and biotic stress combinations, New Phytologist 203: 32-43 doi: 10.1111/nph.12797, (2014).

[Taiz, 2002] Taiz L., Zeiger E., Plant Physiology .,Sinauer Associates, 3 edition, ISBN: 0878938230, (2002).

[Taiz, 2014] Taiz L., Zeiger E., Plant Physiology and Development, Ian Max Moller and Angus Murphy, ISBN: 978-1-60535-255-8, (2014).

[Tanner, 1963] Tanner C.B., Plant temperatures. Agronomy J., 55, 210- 211, (1963).

[Tirot, 2017] Tirot L., Caractérisation de deux types de cellule parenchymateuse chez le Sorgho Sorghum Bicolor, Rapport de Master Biologie des Plantes et des Micro-organismes, CIRAD, (2017).

[Tixier, 2013] Tixier A. Physique et biologie moleculaire de la vulnerabilite du xyleme a la cavitation. These Sciences agricole. Universite Blaise Pascal, Clermont-Ferrand. 53–56pp, (2013).

[Tolivia, 1987] Tolivia D, Tolivia J, Fasga: A new polychromatic method for simultaneous and differential staining of plant tissues. Journal of Microscopy 148: 113-117, (1987).

[Tötzke, 2013] Tötzke C., Miranda T., Konrad W., Gout J., Kardjilov N., Dawson M., Roth-Nebelsick A., Visualization of embolism formation in the xylem of liana stems using neu-

tron radiography. Annals of Botany, 111(4), 723?730. http://doi.org/10.1093/aob/mct0140, (2013).

[Turner, 1988] Turner N.C., Measurement of plant water status by the pressure chamber technique.,Irrigation Science, vol. 9, no. 4, 289–308 pp, (1988).

[Vans As, 1984 and 1985] Van As H. and Schaafsma T., Non invasive measurement of plant water flow by nuclear magnetic resonance., Biophysical Journal, vol. 45, pp 46–472, (1984).

[Van As, 1985] Van As H., Schaafsma T. and Blaakmeer J., Applications of NMR to water flow-Balance in plants., Acta Horticulturae, (1985).

[Van As, 1994] Van As H, Reinders J.E.A., De Jager P.A., Van de Sanden P.A.C.M., Schaafsma T.J., In situ plant water balance studies using a portable NMR spectrometer, J Exp Bot.;45:61-7, (1994).

[Van As, 2007] Van As H. Intact plant MRI for the study of cell water relations, membrane permeability, cell-to-cell and long distance water transport, J. Exp. Bot. 58, 743-756, (2007).

[Van As, 2009] Van As H., Scheenen T. and Vergeldt F.J., MRI of intact plants, Photosynth. Res. 102, 213-222, (2009).

[Van Bel, 2003] Van Bel A.J.E., The phloem, a miracle of ingenuity. Plant, Cell and Environment. 26:125-149, (2003).

[Van Der Maaten, 2016] Van der Maaten E., Van der Maaten-Theunissen M., Smiljanic M., Rossi S., Simard S., Wilmking M., Deslauriers A., Fonti P., Von Arx G., Bouriaud O., DendrometeR: Analyzing the pulse of trees in R, Dendrochronologia 40 12-16, (2016).

[Vesna, 2017] Vesna D., Thermodynamics of Abiotic Stress and Stress Tolerance of Cultivated Plants, http://dx.doi.org/10.5772/60990, (2017).

[Vilagrosa, 2012] Vilagrosa A., Chirino E.,Peguero-Pina J.J., Barigah T.S., Cochard H. and Gil-Pelegrin E., Xylem Cavitation and Embolism in Plants Living in Water-Limited Ecosystems, DOI : 10.1007/978-3-642-32653-0 3,(2012).

[Vo-Dinh, 2002] Vo-Dinh T., Biomedical photonics handbook., ISBN 0-8493-111, pp. 17–20, (2002).

[Wheeler, 1928] Wheeler H. A., Simple Inductance Formulas for Radio Coils, P.IRE, 16, 1398?1400, (1928).

[Windt, 2006] Windt C., Vergeldt F., De Jager P. and Van As H., MRI of long-distance water transport : a comparison of the phloem and xylem flow characteristics and dynamics in poplar, castor bean, tomato and tobacco. Plant, Cell and Environment. 29:1715-1729, (2006).

[Windt, 2011 & 2015] Windt C., Soltner H., Dusschoten D.V., Blumler P., A portable Halbach magnet that can be opened and closed without force: the NMR-CUFF, J.Magn. Reson. 208:27-33, (2011).

[Windt, 2015] Windt C., Blumler P., A portable NMR sensor to measure dynamic changes in the amount of water in living stems or fruit and its potential to measure sap flow, Tree Physiol.,35:366-75, (2015).

[Yamori, 2014] Yamori W., Hikosaka K. and Way D.A., Temperature response of photosynthesis in C3, C4, and CAM plants : temperature acclimation and temperature adaptation, Photosynth. Res., 119: 101, https://doi.org/10.1007/s11120-013-9874-6, (2014).

[Yoshisa, 2011] Yoshida M. and Kramer S., High-field Phase Diagram and Spin Structure of Volborthite Cu3V2O7(OH)2/2H2O., J. Phys. Soc. Jpn. 81, (2012).

[Zarebanadkouki, 2011] Zarebanadkouki M., Quantification and Modeling of Local Root Water Uptake Using Neutron Radiography and Deuterated Water, Vadose Zone Journal 11, (2011).

[Zhu, 2016] Zhu, J.-K., Abiotic stress signaling and responses in plants. Cell, 167(2), 313?324. http://doi.org/10.1016/j.cell.2016.08.029, (2016).